UNIVERSITÀ DEGLI STUDI
DI GENOVA

Università degli studi di Genova

PhD Thesis

Cosmic ray studies with the KM3NeT neutrino telescope

Andrey Romanov

Supervisors:
Dr. Vladimir Kulikovskiy
Dr. Matteo Sanguineti
Prof. Mauro Gino Taiuti

Jury members:
Dr. Rémi Adam
Dr. Ronald Bruijn
Prof. Silvano Tosi

Contents

Introduction

The origin, propagation, and interaction of high-energy Cosmic Rays (CRs) with the atmosphere are not yet fully understood. In particular, we lack precise measurements of the CR hadronic interactions in the very forward region. This work focuses on the investigation of the CR secondary particle properties via the study of high-energy atmospheric muons. Muon detection is performed underwater with the KM3NeT neutrino telescopes.

The KM3NeT research infrastructure comprises two neutrino telescopes at the bottom of the Mediterranean Sea. The KM3NeT/ARCA telescope is in construction off-shore the coast of Sicily, Italy, at a depth of ∼3.5 km. Its primary scientific aim is to study high-energy cosmic neutrinos in the TeV-PeV range. The KM3NeT/ORCA detector has a smaller and denser configuration with respect to KM3NeT/ARCA since its primary goal is to investigate atmospheric neutrino oscillations and neutrino mass hierarchy which requires a lower energy threshold (GeV) for neutrino detection. The telescope is located around 40 km away from Toulon, off the coast of France, at ∼2.5 km depth.

Only muons with TeV energies and above at sea level are able to reach the depths of the KM3NeT detectors. This energy range is about 3 orders of magnitude higher than for the muons detected in Extensive Air Shower (EAS) experiments. Thus, the KM3NeT measurement is complementary to the investigations of the so-called muon puzzle, i.e. deficit of GeV muons detected at the ground with respect to the calculations with known CR flux and hadronic interactions. In particular, the most of low energy muons are produced in the meson decays in the lower atmosphere, while the most energetic muons originate from the very first interactions of CRs with the atmosphere nuclei.

This work comprises five chapters excluding the introduction and conclusion sections. The first chapter is devoted to the overview of the CR measurements and the EAS description. The energy spectrum of CRs, their origin and acceleration mechanism are discussed first. Then, the results from direct and indirect CR experiments are presented. The chapter ends with the EAS description and the introduction to the muon puzzle.

In the second chapter, the KM3NeT neutrino telescopes are discussed. In particular, the detection principle used in KM3NeT and the telescope design are described. Other large-volume neutrino telescopes are also mentioned briefly.

The atmospheric muon simulation for the KM3NeT experiment is presented in the third chapter. During my PhD, I was one of the developers of atmospheric muon simulation software for KM3NeT. The chapter starts with the CORSIKA software description that was used for the EAS simulations. Then, the muon propagation in water, the simulation of the Cherenkov radiation and detector response, and the event reconstruction algorithms used in KM3NeT are described. The reconstruction capabilities of the KM3NeT detectors are also discussed. Finally, the CR energy spectrum as seen by the KM3NeT telescopes is presented.

In the fourth chapter, the framework that I developed for the MUPAGE parametrization tuning on CORSIKA is presented. CORSIKA provides atmospheric muons at sea level, which can be propagated till the detector, performing the full MC simulation of EAS development through the atmosphere. The main drawback of this approach is high CPU time. To reduce CPU time requirement, the simulation of atmospheric muons in KM3NeT is based on the fast

MC generator MUPAGE. It generates the muon bundle kinematics features at a certain sea depth and zenith angle based on parametric formulas. Values of the parameters were originally obtained starting from a full MC simulation performed with the HEMAS package and fitting the results to MACRO measurements. I have developed a framework to adjust the MUPAGE parameters using the CORSIKA simulations with the most recent physics models available, both for the hadronic interaction description (Sibyll 2.3d) and for the CR mass composition (GSF).

The last chapter is devoted to the comparison of the KM3NeT data with the MC simulation which includes the aforementioned models. First, the TeV muon flux at sea level resulting from the CORSIKA simulations is compared to the data from ground-based CR experiments. Then, the KM3NeT capabilities to reconstruct the muon energy and direction are discussed. After that, the KM3NeT data is compared to the MC simulations. Several systematic uncertainties are considered in the comparison: the uncertainty on CR flux and its composition, on the high-energy hadronic interaction model, on light absorption length in seawater, and on the quantum efficiency of the KM3NeT photomultiplier tubes. A mismatch between the data and MC predictions is observed which goes beyond the uncertainties considered. The discrepancy is then discussed in details together with the known results from EAS experiments and from the IceCube neutrino telescope.

1 Cosmic Rays and Extensive Air Showers

Cosmic Rays (CRs) are ionized nuclei, mainly protons, that hit the Earth's atmosphere at a rate of about 1000 particles per square meter per second [1]. They have been extensively studied for more than 100 years and a number of milestone discoveries in physics, such as the discovery of positrons [2] and muons [3], have been made possible thanks to CRs. Their history starts back in 1912 with the discovery of Victor Hess [4]. Three years before Hess' publication, Theodor Wulf measured the rate of ionization near the top of the Eiffel Tower using a portable electroscope [5]. The expectation was that the radiation originates from the Earth and, hence, the ionization rate was expected to decrease with height. Indeed, the rate decreased at the top of the Eiffel Tower but much less than anticipated. In order to further test the hypothesis about the radiation origin, Victor Hess made a series of balloon flights, the highest flight was at an altitude of 5 km. He found that the ionization rate first decreased with height and then began to rise rapidly. The Hess results were later confirmed by Werner Kolhörster in a number of flights up to 9200 m in altitude [6]. Fig. 1.1 illustrates the results of the ionization measurements done by Hess and Kolhörster.

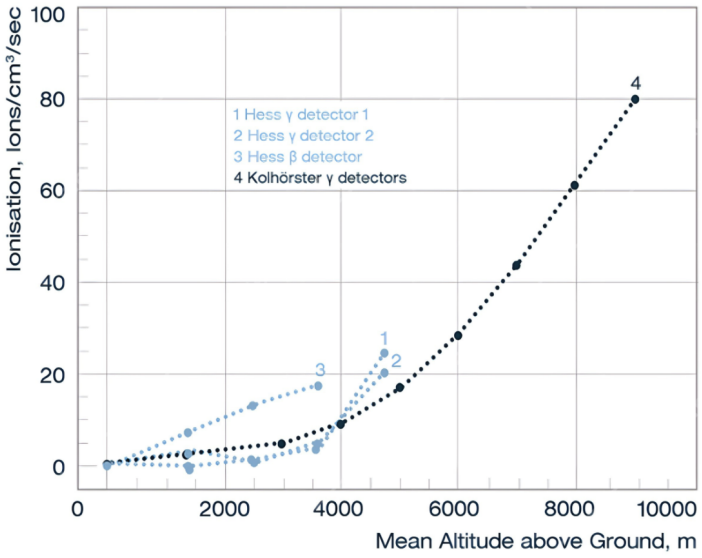

Figure 1.1: Dependence of the ionization on the altitude above the ground as measured during the Hess (light blue points) and Kolhörster (dark blue points) flights. The figure is taken from [7].

1.1 Energy spectrum

The energy of CRs, E, covers a wide range of more than 12 orders of magnitude, from less than a GeV up to more than 10^{11} GeV. The all-particle spectrum together with the individual

fluxes of nuclei up to 100 TeV is presented in Fig. 1.2. The flux was multiplied by $E^{2.7}$ to compensate for its fast drop with energy.

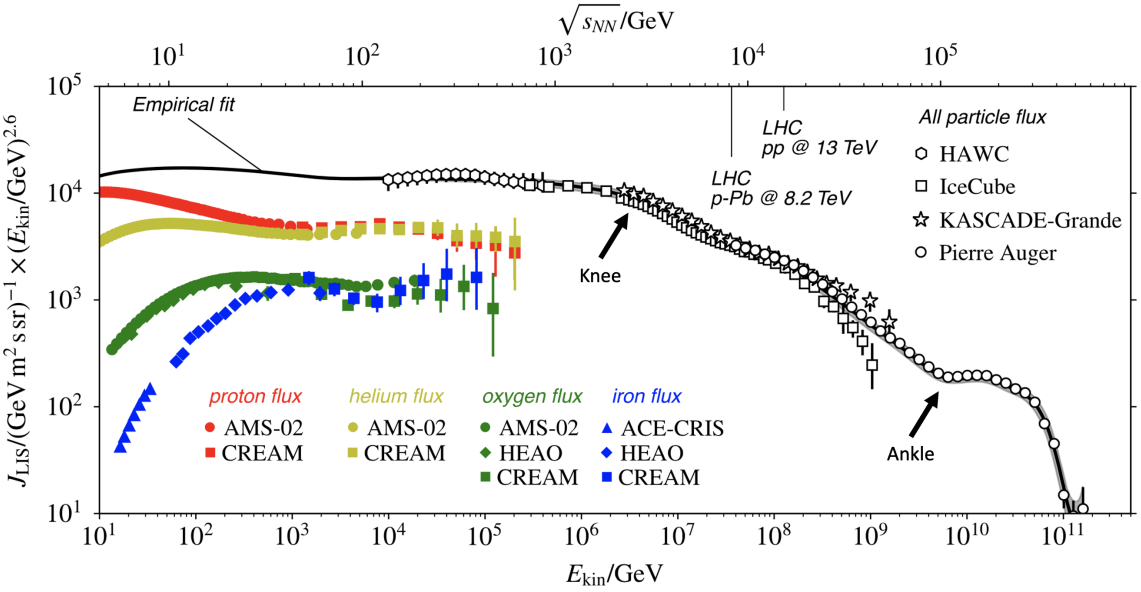

Figure 1.2: All-particle flux of CRs (open symbols) as measured by the HAWC [8], IceCube [9], KASCADE-Grange [10, 11], and Piere Auger [12, 13] experiments. The coloured solid symbols illustrate the fluxes of individual elements, protons (red), helium (yellow), oxygen (green), and iron (blue), that were measured by the direct CR experiments, AMS [14, 15], CREAM [16, 17], and HEAO [18]. The black solid line is the empirical fit of the data [19]. The figure is taken from [20].

In general, the spectrum follows a power law shape with a differential spectral index between 2.7 and 3.3 [21] and with two known transition regions. There is a softening of the spectrum at the energies around 3 PeV, known as the knee. The second transition, the so-called ankle, is at the energies around 3 EeV where the spectrum becomes harder again. Some books report also the third region with the spectrum steepening around 100 PeV, the so-called "second knee", which is believed to be accompanied by a transition to heavy primaries [22].

The reason for the first transition region remains unclear. The possible causes for the knee region are the transition from the supernovae to other galactic CR accelerators [23], propagation effects [22], or the end of the spectrum of galactic CR sources [1].

The reason for the ankle region is also not clearly identified. It may indicate the transition to CR particles that originate from extra-galactic sources [24].

Also, there is a cut-off at the end of the energy spectrum, around 50 EeV. One of the explanations for the cut-off is the Greisen-Zatsepin-Kuzmin (GZK) effect [25, 26]. The GZK effect implies that ultra-high energy protons start to interact with the microwave background at the energies of about 70 EeV [1] producing pions via a Δ-resonance. Hence, the particles lose their energy in each interaction until the energy is lower than the Δ-resonance production threshold which leads to the suppression of the flux. The energy at which the integral flux drops by a factor of two with respect to the no-cut-off scenario is $E_{1/2} = 53$ EeV assuming the GZK effect. The Pierre Auger Observatory measured the $E_{1/2}$ value and the result is $E_{1/2} = 22 \pm 1$ (stat.) ± 3 (syst.) EeV [27], lower than the GZK prediction. Therefore, it is

still not clear whether the cut-off is caused by the GZK effect alone or by its combination with other processes, such as the limited acceleration energy or a mixed CR mass-composition at the sources [28].

The main questions that arise about CRs are their origin, acceleration mechanism, and mass composition. The first two questions are discussed in Sec. 1.2 and Sec 1.3, correspondingly. The composition of CRs is considered within the results from the direct, Sec. 1.4, and indirect experiments that explore Extensive Air Showers (EAS) to study CRs, Sec. 1.5.

1.2 Origin of Cosmic Rays

Since CRs are charged particles they are deflected in the magnetic fields during their propagation from the sources to the Earth. The CR flux observed on the Earth is very isotropic up to ultra-high energies. At the energies above $\sim 10^{18}$-10^{19} eV, there are observations of the CR anisotropies reported by the Telescope Array [29] and Pierre Auger Observatory [30]. The possibility to track back the particle paths and identify the sources even for ultra-high energy CRs is still an open question since the extragalactic magnetic fields are poorly known [22]. Therefore, the exact origin of CRs is still under debate and there are only possible candidates that may accelerate particles up to the measured CR energies.

The maximum acceleration energy of the potential CR sources can be estimated using the so-called Hillas criterion [31]. The criterion states that a charged particle is able to escape a CR accelerator if its gyroradius, r_g, is larger than the size of the accelerator. The gyroradius, also known as the Larmor radius, is the radius of a particle's circular motion in the homogeneous magnetic field with strength B: $r_g = p/qB$, where p is the particle momentum and q is its charge. Hence, in order to be able to escape the cosmic accelerator, the particle must have sufficiently high energy. If the size and magnetic field strength of the potential CR source are known then it is possible to estimate up to which energy the particle can be accelerated.

The Hillas criterion allows an estimation of possible CR sources for different energy regions of the CR spectrum, Fig. 1.3. The possible galactic CR sources illustrated on the plot are pulsars, such as neutron stars [32] and white dwarfs [33], sun spots (for low-energy CRs) [34], microquasars (binary system involving a black hole and a companion star) [35], interplanetary medium [36], supernova remnants [37], galactic disc [38] and halo [39]. Also, there are several extragalactic candidate sources, in particular active galactic nuclei [40], gamma ray bursts [41], blazars [42], lobes of radio galaxies [43], galaxy clusters [44], wind from starburst galaxies [45], and intergalactic medium [46].

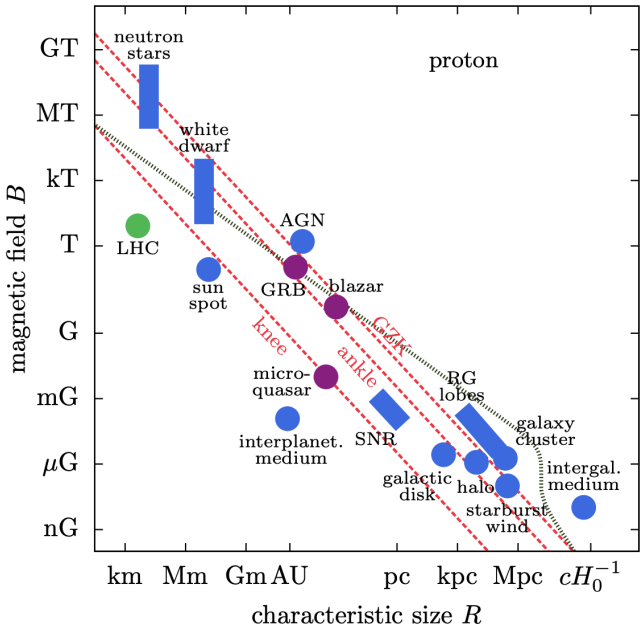

Figure 1.3: The Hillas plot in its modern adaptation. The figure shows the upper limits of the CR energy that can be reached in different sources. The limits depend on the size of the cosmic object and on its magnetic field strength. The red-dashed lines illustrate the knee and ankle transition regions and the GZK cut-off for proton CRs. The dotted gray line is the upper limit from synchrotron losses in the sources and interactions with the cosmic photon background. The green dot represents the size and the magnetic field strength of the LHC experiment. This figure is taken from [47].

1.3 Acceleration mechanism

Exact mechanisms that can explain how CRs gain their energies for the whole spectrum still remain unclear. One possible and commonly used model of CR acceleration is the so-called Fermi mechanism. It was first proposed by Enrico Fermi in 1949 to explain the origin of CRs [48]. The mechanism is based on the interactions ("encounters") between charged particles and magnetic fields, which can lead to the iterative energy gain of the particles. There are the first- and second-order Fermi acceleration mechanisms, that differ in the way particles are scattered and accelerated.

In his original paper, Fermi considered the charged particle interactions with the magnetized interstellar clouds. This is now known as the second-order Fermi acceleration mechanism which is discussed here firstly in Sec. 1.3.1. The first-order mechanism involves interactions of particles with a large plane shock front, Sec. 1.3.2.

1.3.1 Second-order Fermi acceleration

Scheme of the second-order acceleration mechanism is illustrated in Fig. 1.4 [1]. A charged particle with initial energy E_1, in the lab frame, encounters with a cloud of magnetized plasma that moves at a speed $\vec{V}$. The particle enters the cloud at an angle θ_1 and leaves it at an angle θ_2 with respect to the cloud's moving direction.

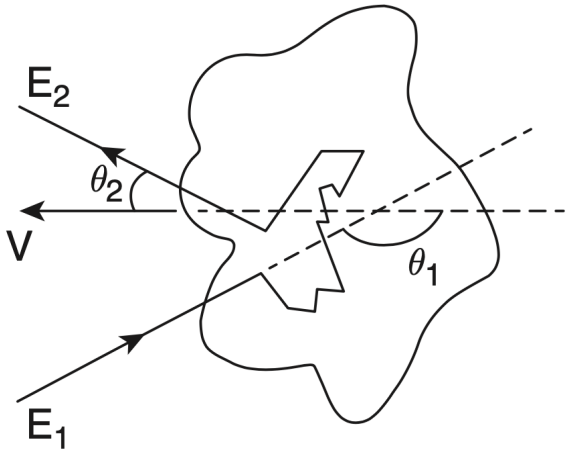

Figure 1.4: Sketch of the second-order Fermi acceleration mechanism for the charged particle with initial energy E_1 encountering with the magnetized cloud of a speed $\vec{V}$. The figure is taken from [1].

In order to estimate the energy difference before and after the interaction, it is useful to recalculate the particle energy in the cloud reference frame, i.e. the frame where the magnetized plasma is at rest. This energy, E_1', is given by [49]:

$$E_1' = \frac{E_1 - (\vec{V} \cdot \vec{p})}{\sqrt{1 - V^2/c^2}} = \frac{E_1 - \frac{V}{c} pc \cos\theta_1}{\sqrt{1 - V^2/c^2}}, \tag{1.1}$$

where $\vec{p}$ is the particle momentum. Denoting $1/\sqrt{1 - V^2/c^2} = \gamma$ and $\frac{V}{c} = \beta$, and assuming that the particle is highly-relativistic so that $E_1 \approx pc$, Eq. 1.1 becomes

$$E_1' = \gamma E_1 (1 - \beta \cos\theta_1). \tag{1.2}$$

Since all the interactions in the cloud magnetic field are elastic, the particle energy after leaving the cloud remains the same, $E_2' = E_1'$. The final energy in the lab frame after the encounter is then:

$$E_2 = \gamma E_2' (1 + \beta \cos\theta_2') = \gamma^2 E_1 (1 - \beta \cos\theta_1)(1 + \beta \cos\theta_2'). \tag{1.3}$$

Hence, the relative difference between the final and initial energy is

$$\frac{\Delta E}{E_1} = \gamma^2 (1 - \beta \cos\theta_1)(1 + \beta \cos\theta_2') - 1 = \frac{1 - \beta \cos\theta_1 + \beta \cos\theta_2' - \beta^2 \cos\theta_1 \cos\theta_2'}{1 - \beta^2} - 1. \tag{1.4}$$

In order to estimate the average energy difference, the result obtained in Eq. 1.4 must be averaged over the possible incoming, $\cos\theta_1$, and outgoing, $\cos\theta_2'$, directions. All the scatterings in the cloud magnetic field are assumed to be isotropic, therefore the probability per unit solid angle, $dP/d\Omega_2$, that the particle leaves the cloud at an angle θ_2' is the same for each angle:

$$\frac{dP}{d\Omega_2} = \text{constant} = k. \tag{1.5}$$

Hence, the average value, $< \cos\theta_2' >$, is obtained as

$$\begin{aligned} < \cos\theta_2' >= & \int (\cos\theta_2' \frac{dP}{d\Omega_2}) d\Omega_2 \Big/ \int (\frac{dP}{d\Omega_2}) d\Omega_2 \\ < \cos\theta_2' >= & \frac{\int_0^{2\pi} d\phi \int_{-1}^{1} k \cos\theta_2' d\cos\theta_2'}{\int_0^{2\pi} d\phi \int_{-1}^{1} k d\cos\theta_2'} = 0. \end{aligned} \tag{1.6}$$

The probability that the particle enters the cloud at a solid angle Ω_1 is proportional to the rate of collisions between the particle and the cloud which depends on their relative velocity:

$$\frac{dP}{d\Omega_1} \sim v - V\cos\theta_1, \tag{1.7}$$

with v being the particle velocity. The average value of $\cos\theta_1$ is then

$$< \cos\theta_1 >= \frac{\int_0^{2\pi} d\phi \int_{-1}^{1} k \cos\theta_1 (v - V\cos\theta_1) d\cos\theta_1}{\int_0^{2\pi} d\phi \int_{-1}^{1} k (v - V\cos\theta_1) d\cos\theta_1}. \tag{1.8}$$

Dividing nominator and denominator by c and assuming that the particle is highly-relativistic so that $v/c \approx 1$, Eq. 1.8 turns into

$$< \cos\theta_1 >= \frac{\int_{-1}^{1} \cos\theta_1 (1 - \beta\cos\theta_1) d\cos\theta_1}{\int_{-1}^{1} (1 - \beta\cos\theta_1) d\cos\theta_1} = -\frac{1}{3}\beta. \tag{1.9}$$

Incorporating the results of Eq. 1.6 and Eq. 1.9 into Eq. 1.4 and assuming that the clouds are non-relativistic ($1 - \beta^2 \approx 1$), the average relative energy gain per each encounter in the second-order Fermi mechanism is

$$< \frac{\Delta E}{E_1} >= \frac{1 + \frac{1}{3}\beta^2}{1 - \beta^2} - 1 \approx \frac{4}{3}\beta^2. \tag{1.10}$$

Since the random velocities of interstellar clouds in the galaxy and the diffusion velocities of supernova remnants are very small, $\beta \sim 10^{-4}$ and $\beta \sim 10^{-3} - 10^{-2}$, correspondingly [21], the second-order mechanism is not efficient enough to explain the measured CR spectrum. A linear energy gain is needed which occurs during the particle interactions with shock waves as described below.

1.3.2 First-order Fermi acceleration

The first-order Fermi mechanism implies that the charged particle interacts with a shock front, Fig. 1.5. The front velocity in the lab frame is $-\vec{u}_1$ and the shocked gas moves away from the front with relative velocity $\vec{u}_2$, $|u_2| < |u_1|$.

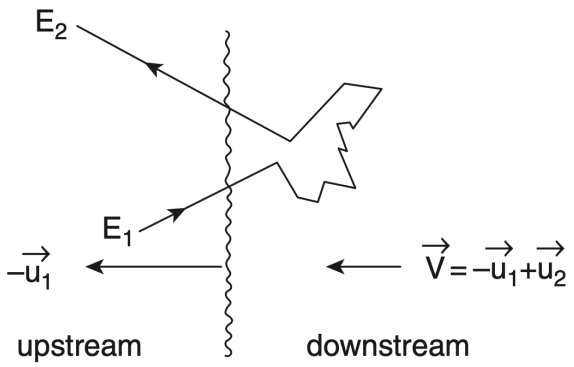

Figure 1.5: Scheme of the first-order Fermi mechanism. The particle interacts with the shock front. The figure is taken from [1].

The calculation of the relative difference in the particle energy before and after scattering on the shock front is the same as in Sec. 1.3.1 and it leads to Eq. 1.4. In this case, $\vec{V}$ is the speed of the shocked gas in the lab frame, $\vec{V} = -\vec{u_1} + \vec{u_2}$. The main difference between the two mechanisms is the calculation of the angular averages. In case of the plane shock front, which is assumed to be infinite, the particle always faces it from the upstream side, $\pi/2 \leq \theta_1 \leq 3\pi/2$, and, thus, $-1 \leq \cos\theta_1 \leq 0$, and it leaves the shock front in the opposite direction, $-\pi/2 \leq \theta_2' \leq \pi/2$ ($0 \leq \cos\theta_2' \leq 1$). The probability that the particle leaves the shock front at a solid angle Ω_2 is determined as the normalized projection of an isotropic flux onto a plane:

$$\frac{dP}{d\Omega_2} = \cos\theta_2'. \tag{1.11}$$

Hence, the average value of $\cos\theta_2'$ is

$$< \cos\theta_2' >= \frac{\int_0^{2\pi} d\phi \int_0^1 (\cos\theta_2')^2 d\cos\theta_2'}{\int_0^{2\pi} d\phi \int_0^1 \cos\theta_2' d\cos\theta_2'} = \frac{2}{3}. \tag{1.12}$$

The distribution of $\cos\theta_1$ for the plane shock is also the same projection, therefore,

$$< \cos\theta_1 >= \frac{\int_{-1}^0 (\cos\theta_1)^2 d\cos\theta_1}{\int_{-1}^0 \cos\theta_1 d\cos\theta_1} = -\frac{2}{3}. \tag{1.13}$$

Finally, the average energy gain in the first-order Fermi mechanism is obtained omitting the squared β terms. The energy gain is linear in β:

$$< \frac{\Delta E}{E_1} >= \frac{1 + \frac{2}{3}\beta + \frac{2}{3}\beta + \frac{4}{9}\beta^2}{1 - \beta^2} - 1 = \frac{4}{3}\beta. \tag{1.14}$$

1.3.3 Power-low energy spectrum

Both acceleration schemes lead to a power-low spectrum for CRs. As was shown above, the energy of a particle increases proportionally to its initial value, $\Delta E = \xi E$. Another important assumption is that the energy gain process is repeated several times. After n interactions, the particle energy becomes

$$E_n = E_0(1 + \xi)^n. \tag{1.15}$$

The number of interactions needed to reach the energy E_n is then given by

$$n = \ln\left(\frac{E}{E_0}\right)/\ln(1+\xi). \tag{1.16}$$

Assuming that the probability to remain in the acceleration region after one encounter is p, the proportion of particles accelerated up to energies greater than E_n is

$$N(\geq E_n) \propto p^n. \tag{1.17}$$

Inserting the Eq. 1.16 into the Eq. 1.17, the energy distribution is obtained:

$$N(\geq E) \propto p^{\ln(\frac{E}{E_0})/\ln(1+\xi)} = \left(\frac{E}{E_0}\right)^{\ln p/\ln(1+\xi)} = \left(\frac{E}{E_0}\right)^{-\gamma}, \tag{1.18}$$

where $\gamma = \ln(1/p)/\ln(1+\xi)$. Hence the CR spectrum at the sources is

$$\left(\frac{dN}{dE}\right)_{\text{source}} \propto \left(\frac{E}{E_0}\right)^{-(\gamma+1)}. \tag{1.19}$$

Therefore, the Fermi acceleration mechanism leads to the observed power-low spectrum of CRs. A value of γ is around one for the supersonic shock of a monoatomic gas as predicted by the kinetic theory of gases [50]. In order to estimate the CR spectrum observed on the Earth, one needs to take into account also the propagation effects which modify the spectrum proportionally to $E^{-\delta}$ [21]:

$$\left(\frac{dN}{dE}\right)_{\text{Earth}} \propto \left(\frac{dN}{dE}\right)_{\text{source}} \times E^{-\delta} \propto \left(\frac{E}{E_0}\right)^{-(\gamma+\delta+1)}. \tag{1.20}$$

A value of δ can be obtained from the measurements of the boron-to-carbon ratio in CRs [22]. This value is around $0.3 - 0.6$ so the final value of the spectrum power is $\approx -(2.3 - 2.6)$, in agreement with the measured value mentioned in Sec. 1.1. Therefore, the first-order Fermi acceleration mechanism predicts not only the power-law shape of the CR spectrum but also a theoretical value of the power close to the observed one.

The Fermi mechanism can explain the CR spectrum below the knee ($\sim 10^6$ GeV) assuming SNR as the CR accelerators [1]. For the higher energies, however, additional theories are required such as the particle acceleration through electromagnetic mechanisms associated with time-varying magnetic fields [22].

1.4 Direct CR experiments

The CR flux at the energies below a few hundred TeV is high enough to perform direct measurements. For instance, the flux at around 100 GeV is about two particles per square meter per steradian per second. Thus, it is possible to measure CRs directly before they interact with the Earth's atmosphere. The precise measurements of CRs with energies below 1 TeV/nucleon are carried using detectors with magnetic spectrometers located at the International Space Station, e.g. AMS [14], or on satellites, e.g. PAMELA [51]. For the higher energies, a calorimeter detector system without a magnetic spectrometer is used that allows a larger geometrical acceptance, e.g. the CREAM experiment uses this technology [16]. It was placed on a large balloon and conducted its measurements during several flights over Antarctica. The result obtained by the CREAM experiment is the CR spectrum from 1 GeV up to 100 TeV.

Fig. 1.6 illustrates the CR composition as measured by several direct experiments, AMS [14, 15], ATIC [52], BESS [53], CREAM [16], CRN [54], HEAO [18], HESS [55], JACEE [56], PAMELA [51], RUNJOB [57], and TRACER [58]. The most abundant CRs are protons, about 90% of the total flux, helium constitutes another 9% and the rest are heavier nuclei.

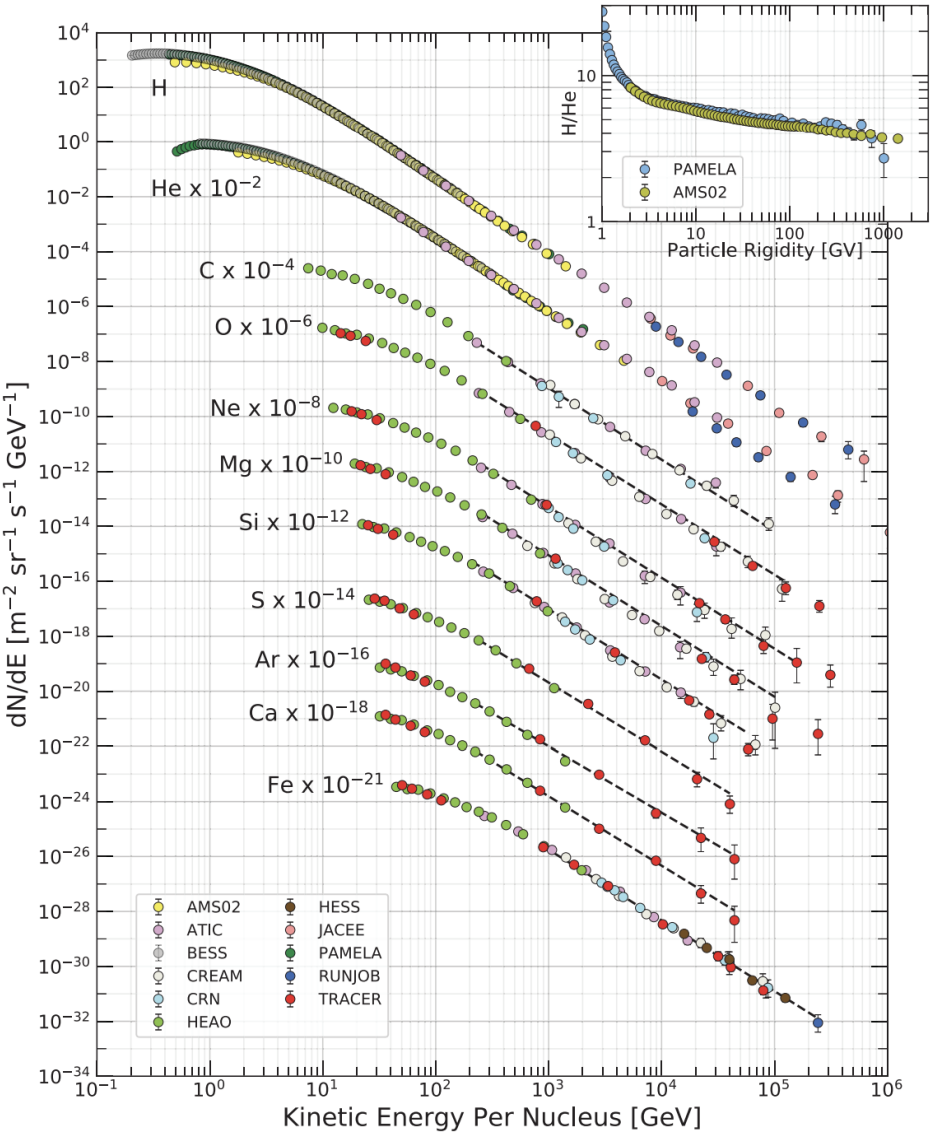

Figure 1.6: Fluxes of CR nuclei as a function of an energy per nucleus as measured by several direct experiments. The top right sub-plot shows the ratio of protons to helium nuclei as a function of rigidity. The figure is taken from [59].

1.5 Extensive Air Showers

The CR flux at the energies above 1 PeV is less than a few tens of particles per square meter per year. Hence, in order to measure such a low flux, either a large aperture or a long time exposure is required. Neither of these is possible with the direct CR detectors. Thus, they are

replaced by the indirect ground-based observatories that may cover up to several thousands of km^2 [12] or by the underground/underwater experiments [60, 61, 62, 63]. The showers are the cascades of particles initiated by high-energy CRs interacting in the upper atmosphere. EAS are of particular interest of the KM3NeT experiment since they are the sources of high-energy muons detected by the telescopes.

There are three components of EAS: electromagnetic, muonic, and hadronic. A sketch that illustrates a shower cascade is presented in Fig. 1.7.

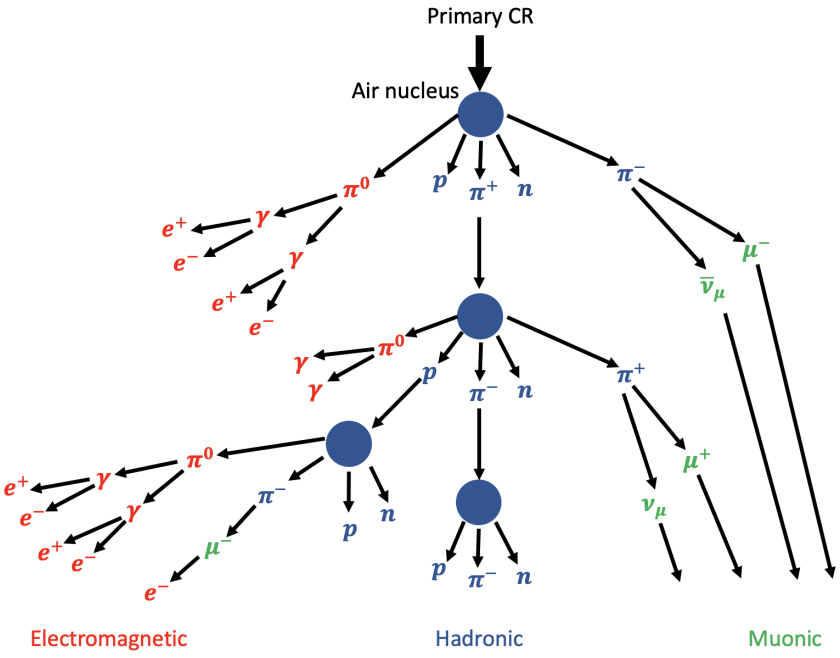

Figure 1.7: Sketch of an EAS cascade. Particles that constitute the electromagnetic, hadronic, and muonic components are shown in red, blue, and green, correspondingly.

The electromagnetic component consists of electrons, positrons, and photons that are produced in the decays of muons and neutral pions. Photons with energies higher than two electron rest masses may produce an electron-positron pair in the vicinity of an atomic nucleus. Leptons lose their energy due to radiation processes like Bremsstrahlung which leads to the emission of more photons. Hence, there is a cascade of secondary particles, called electromagnetic cascade.

The muonic component of EAS consists of muons that penetrate deeper into the atmosphere than the electrons and photons since the muon bremsstrahlung cross-section is smaller. The muon cascade can extend over several kilometers and can be detected on the ground [64]. High-energy muons may penetrate also few kilometres below the sea level and can be detected by the KM3NeT telescopes. These muons are the main research subject of this work.

The hadronic component includes protons, neutrons, pions, kaons, and heavier hadrons and they are responsible for most of the energy transfer from the primary CRs to the atmosphere. The hadronic cascade feeds the electromagnetic part of the shower, primarily by photons from the decay of neutral pions. The charged pions and kaons decay into muons and feed the muonic component.

1.5.1 Description of Extensive Air Showers

The development of EAS can be described by means of coupled differential equations [20]. The equations represent the evolution of the density, n, of particles of a certain type, k, as a function of slant depth, X:

$$\begin{aligned}\frac{dn}{dX} = &-(\frac{1}{\lambda_{\text{int},k}(E)} + \frac{1}{\lambda_{\text{dec},k}(E,X)})n(E,X) - \frac{d}{dE}(\mu_k(E)n(E,X)) \\ &+ \sum_l \int_E^\infty dE_l \frac{c_{l\to k}(E_l,E)}{\lambda_{\text{int},l}(E_l)n_l(E_l,X)} + \sum_l \int_E^\infty dE_l \frac{d_{l\to k}(E_l,E)}{\lambda_{\text{dec},l}(E_l,X)n_l(E_l,X)}.\end{aligned} \tag{1.21}$$

Here, $\lambda_{\text{int},k}(E)$ and $\lambda_{\text{dec},k}(E,X)$ are the interaction and decay lengths, correspondingly. They depend on the particle energy, E, and, in the case of the decay length, on the slant depth traveled. The function $\mu_k(E)$ incorporates the energy losses due to ionization. The last two terms describe gains in the particle density from interactions and decays of particles of type l, which depend on the transfer probabilities $c_{l\to k}$ (for interactions) and $d_{l\to k}$ (for decays).

The equations offer exact solutions if all relevant processes are implemented. Assuming an initial condition from the energy spectra of cosmic nuclei, $n_k(E,0)$, the particle densities can be calculated for an average air shower, e.g. with the MCEq software [65]. Shower-to-shower fluctuations can be accounted for with Monte Carlo methods, e.g. CORSIKA [66].

Two main observables that are used for the CR composition measurements with indirect experiments are the depth of the shower maximum where the maximal number of charged particles is reached, X_{max}, and the number of muons in the shower, N_μ. The values of these observables depend on the type of nucleus that initiated the shower. This is discussed below in Sec. 1.5.2 within the Heitler-Matthews model [67].

1.5.2 The Heitler-Matthews model

In order to have an insight into how the EAS properties depend on the type of primary without the need to solve the cascade equations, the qualitative approach is useful to be considered. Such an approach that is often used for the EAS development description [20] is the Heitler-Matthews model [67].

The model implies that the shower contains only neutral, π^0, and charged, $\pi^\pm$, pions. Neutral pions are assumed to decay immediately into photon pairs. Charged pions undergo further interactions until their energy becomes equal to the critical energy, E_c, i.e. when the decay length is equal to the interaction length. At that point, the cascade development stops, and all the charged pions that remain in the shower decay into muons.

Energy is assumed to be distributed equally between all the pions in each step. The number of particles produced in each interaction is n_{tot} and the fraction of charged pions produced is α.

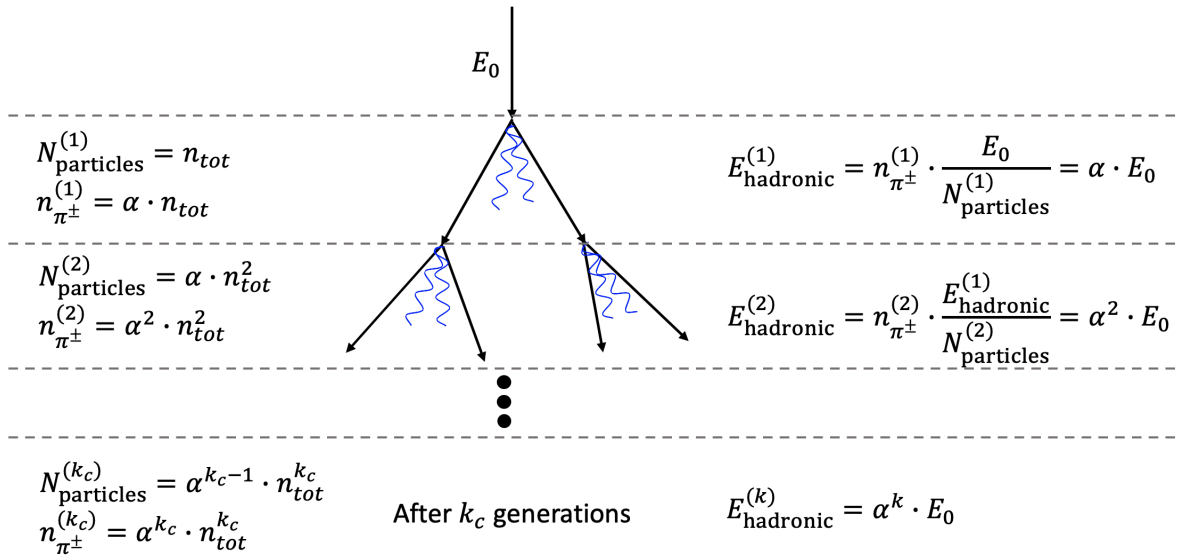

Figure 1.8: Scheme of the EAS development in the Heitler-Matthews model. The shower is initiated with a primary of energy E_0. The total number of pions in i-th step is denoted as $N^{(i)}_{\text{particles}}$, and the number of charged pions is $n^{(i)}_{\pi^\pm}$.The energy remaining in the hadronic (charged pions) component of cascade in i-th step is $E^{(i)}_{\text{hadronic}}$.

Number of muons in EAS

Under the aforementioned assumptions, the number of muons in the proton-induced shower can be calculated, N^p_μ. First, the total number of shower generations, k_c, should be obtained. The shower development stops when $E_{\pi^\pm} = E_c$. The energy remaining in the charged pion component of the shower after k_c steps is $\alpha^{k_c} E_0$, and the number of charged pions is $N_\mu = (\alpha n_{\text{tot}})^{k_c}$. Hence, the final energy of each pion is $E_{\pi^\pm} = \alpha^{k_c} E_0/(\alpha n_{\text{tot}})^{k_c}$. Therefore, equating this energy to the critical energy, the number of shower generations is obtained:

$$\begin{aligned} \alpha^{k_c} E_0/(\alpha n_{\text{tot}})^{k_c} &= E_c \\ \Rightarrow k_c &= \frac{\ln(E_0/E_c)}{\ln n_{\text{tot}}} \end{aligned} \tag{1.22}$$

The number of charged pions after k_c steps can be then calculated:

$$\begin{aligned} N^p_\mu(E_0) &= (\alpha n_{\text{tot}})^{k_c(E_0)} \\ \ln(N^p_\mu(E_0)) &= k_c(E_0) \ln(\alpha n_{\text{tot}}) \\ \ln(N^p_\mu(E_0)) &= \beta \ln(E_0/E_c), \end{aligned} \tag{1.23}$$

where $\beta = \frac{\ln(\alpha n_{\text{tot}})}{\ln(n_{\text{tot}})} \approx 0.82 - 0.95$ from full Monte Carlo (MC) simulations [1]. Finally, exponentiating the last part of Eq. 1.23, N^p_μ is obtained:

$$N^p_\mu(E_0) = (E_0/E_c)^\beta. \tag{1.24}$$

In order to calculate the number of muons from other primary nuclei, the superposition model is assumed. The shower initiated by a nucleus with A nucleons is treated as A independent showers with energies $E_A = E_0/A$. Since the number of muons non-linearly depends on primary

energy (Eq. 1.24), showers of the same energy induced by different nuclei can be distinguished. The number of muons from the primary nucleus with A nucleon is

$$\begin{aligned} N_\mu^A(E_0) &= A \times N_\mu^p(E_0/A) \\ N_\mu^A(E_0) &= A \times (\frac{E_0/A}{E_c})^\beta \\ N_\mu^A(E_0) &= A^{(1-\beta)} \times N_\mu^p(E_0). \end{aligned} \tag{1.25}$$

Therefore, the EAS initiated by nucleon with A nucleus has $A^{(1-\beta)}$ times more muons than the shower induced by a proton with the same energy.

Fig. 1.9 shows the average difference in the number of muons that reach the sea level originating from the proton and iron showers. The plot was obtained with MCEq software [65] using the Sibyll 2.3c model for the hadronic interactions. The difference is around 40% on the PeV and EeV scales.

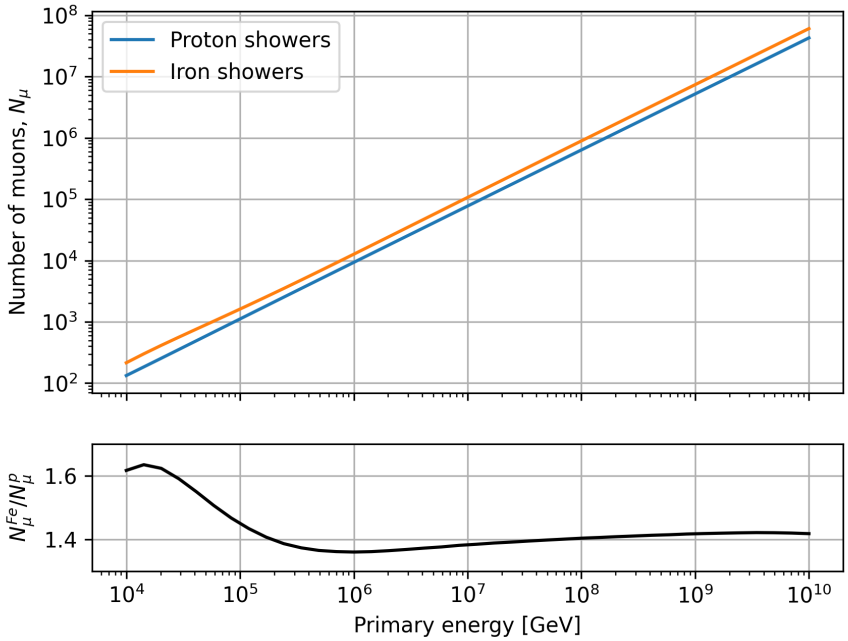

Figure 1.9: Number of muons reaching the sea level from proton (blue curve) and iron (orange curve) showers as a function of primary energy. The bottom plot show the ratio of the number of muons originating from the iron shower with respect to the proton shower.

Depth of the shower maximum

Using the Heitler-Matthews model, it is also possible to estimate another observable that is often measured by indirect experiments for the composition studies, the depth of the shower maximum, $X_{\max}$. The shower maximum is defined as the stage of the shower development where the maximum number of charged particles is produced. In the Heitler-Matthews model,

the maximum number of changed pions is reached after k_c generations. Hence, the depth of shower maximum induced by a proton with energy E_0 is

$$X^p_{\max}(E_0) = k_c \lambda_{\text{int}} = \frac{\ln(E_0/E_c)}{\ln(n_{\text{tot}})}\lambda_{\text{int}}, \tag{1.26}$$

where λ_{int} is the charged pion interaction length in the air. The $X_{\max}$ value for the shower that was initiated by the nucleus with energy E_0 and with A nucleon can be estimated using the superposition model described above. In that case, the depth of the shower maximum is equivalent to the one of the proton shower with energy E_0/A:

$$\begin{aligned} X^A_{\max}(E_0) &= X^p_{\max}(E_0/A) = \frac{\ln(E_0/(AE_c))}{\ln(n_{\text{tot}})}\lambda_{\text{int}} \\ X^A_{\max}(E_0) &= \frac{\ln(E_0/E_c)}{\ln(n_{\text{tot}})}\lambda_{\text{int}} - \frac{\lambda_{\text{int}}}{\ln(n_{\text{tot}})}\ln(A) \\ X^A_{\max}(E_0) &= X^p_{\max}(E_0) - D_p \ln(A), \end{aligned} \tag{1.27}$$

where $D_p(E_0) = \frac{dX^p_{\max}(E_0)}{d\ln E_0}$ is the so-called elongation rate for the proton shower that is usually estimated from the full MC simulations.

The difference in the $X_{\max}$ values for the proton and iron showers is plotted in Fig. 1.10. On average, the proton showers develop deeper in the atmosphere by about 150-100 g cm^{-2} with respect to the iron showers of the same energy at the PeV-EeV scale.

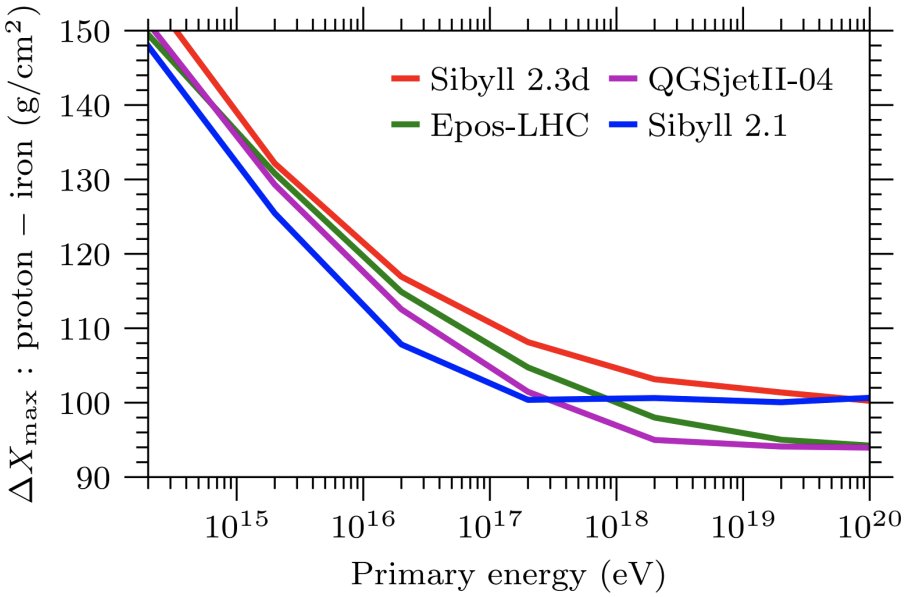

Figure 1.10: The difference in the values of the shower maximum depth between the proton and iron showers, $X^p_{\max} - X^{Fe}_{\max}$. The results were obtained for four different hadronic interaction models, Sibyll 2.1 [68] (blue curve), Sibyll 2.3d [69] (red curve), QGSjetII-04 [70] (purple curve), and EPOS-LHC [71] (green curve). The figure is taken from [69].

1.5.3 Experimental results

The all-particle spectrum obtained with the indirect CR experiments is shown in Fig. 1.2. The results of the CR composition measurements by the EAS detectors are presented in Fig. 1.11. The indirect CR experiments are sensitive to logarithmic mass number, $\ln A$, rather than A, since the composition observations are based on the EAS properties ($X_{\max}$ and N_μ) which fluctuate from shower to shower and these fluctuations are larger than the average values of these observables for the neighboring elements [19].

Interpretation of the results of indirect CR experiments relies on air shower simulations. The core feature of the simulations is the model of the high-energy hadronic interactions. The dominating hadronic collisions in EAS are those with small momentum transfer, which cannot be calculated with perturbative quantum chromodynamics. Also, the collisions lay in the very forward region of rapidities which is only partially covered by the accelerator experiments. Hence, the hadronic models rely necessarily on the extrapolations of the existing experimental results [20]. Therefore, the uncertainty of the mass composition measurements with the EAS detectors is dominated by the systematics. The uncertainties are shown as bands in Fig. 1.11.

The results presented in the figure were obtained with the pre-LHC hadronic interaction models. The uncertainties are expected to be reduced using the recent models. However, it is known that the models still cannot describe the detected muon content of EAS [20]. This discrepancy is known as the muon puzzle and it is discussed in more details in Sec. 1.6.

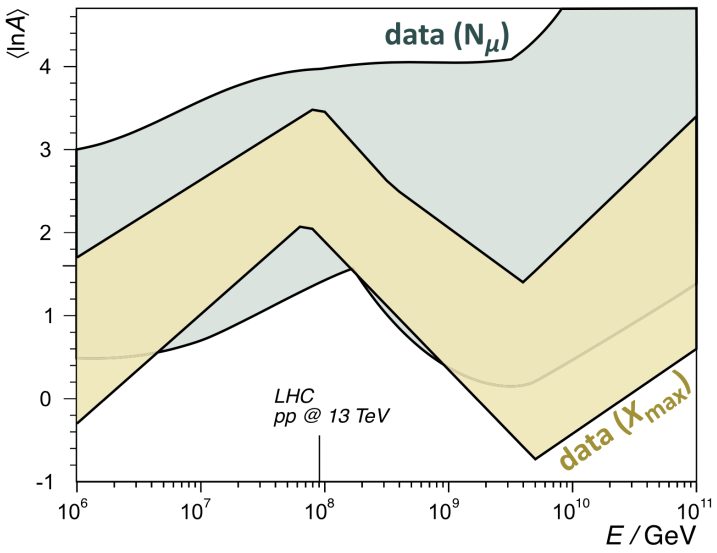

Figure 1.11: The experimental results of the CR mass composition measurements with the EAS detectors using the two mass-sensitive variables, $X_{\max}$ and N_μ . The yellow (green) band shows show the uncertainties of the mass composition measurements using $X_{\max}$ (N_μ). The figure is taken from [20].

1.6 The muon puzzle

Ground-based CR experiments are able to measure the GeV muons of EAS. In 2015 the Pierre Auger Observatory (PAO) reported that the measured number of muons is larger than the one predicted by the current theoretical models [72]. Although, the PAO results were not

the first claiming that this discrepancy is present, e.g. [73, 74], but their studies were the first nearly model-independent with well-controlled systematics and post-LHC hadronic models. This observation triggered other experiments to perform follow-up measurements or to re-analyze previously collected data, and several of them confirmed the PAO results [75, 76, 77].

This muon deficit in the shower simulations was called "the muon puzzle". Having the contributions from several experiments and the data that covers a wide CR energy range, the Working group on Hadronic Interactions and Shower Physics (WHISP) was formed to review the existing results involving members of eight experimental collaborations [78]. In order to combine the measurements from different experiments, WHISP introduced the z-value which can be computed using the results obtained by every experiment and corresponding MC simulation with different hadronic interaction models:

$$z = \frac{\ln\langle N_\mu\rangle - \ln\langle N_\mu\rangle_p}{\ln\langle N_\mu\rangle_{\mathrm{Fe}} - \ln\langle N_\mu\rangle_p}. \tag{1.28}$$

Here, $\langle N_\mu\rangle$ is the average measured number of muons in a certain primary energy interval, $\langle N_\mu\rangle_p$ and $\langle N_\mu\rangle_{\mathrm{Fe}}$ are the muon numbers obtained from the MC simulations for the same energy interval assuming pure proton and pure iron composition of the flux, correspondingly. If there is no discrepancy between the data and simulations then the value of z is in between 0 and 1 since proton and iron are the limits of the CR mass composition range. If the z-value exceeds 1 that means that there are more muons observed in the data in comparison to the simulations which cannot be explained by the physical CR flux composition. This excess was indeed found for several experiments and hadronic models, Fig. 1.12.

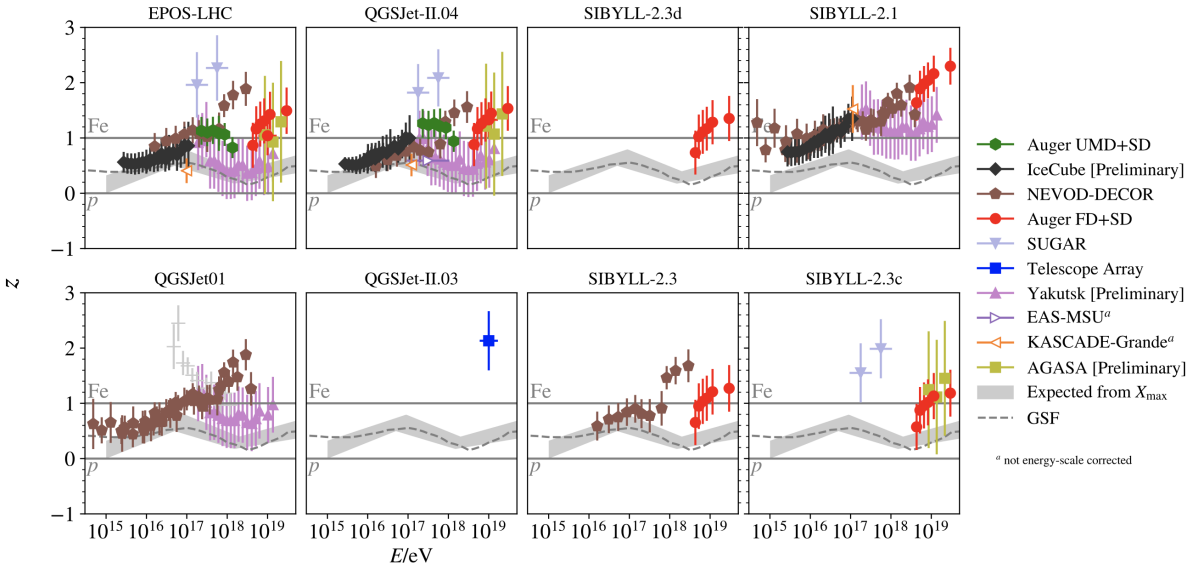

Figure 1.12: The z-value distributions obtained for the different experiments and hadronic interaction models. The discrepancy starts to emerge for the primary CR energies around 10 PeV. The figure is taken from [20].

One of the main goals of this work is to investigate if there is a discrepancy in the muon content predicted by the recent theoretical models and the one observed by the KM3NeT telescopes. The underwater or underground experiments measure muons with higher energies with respect to the ground-based detectors. Muons must have sufficient energy at sea level to be able to

travel several kilometers of overburden. In the case of the KM3NeT experiment, this low-energy threshold is around 500 GeV with the majority of muons having energies in the TeV range as discussed in Chapter 3. Also, the CR energy range of the KM3NeT telescopes differs from the one in which the ground-based detectors are operating. Therefore, the KM3NeT results can provide important additional input for the studies of theoretical models that aim to describe CRs.

2 The KM3NeT neutrino telescopes

The KM3NeT research infrastructure comprises two neutrino telescopes at the bottom of the Mediterranean Sea [79]. The telescope detection technology and the design are the same for both detectors but the scientific goals are different thanks to the difference in the detector geometries. Both telescopes are still under construction but they are already taking data and the first physics results were already obtained [80].

As of June 2023, the KM3NeT Collaboration includes around 250 members from more than 50 institutes. The map that shows the location of the KM3NeT institute members and the sites of the two telescopes is illustrated in Fig. 2.1.

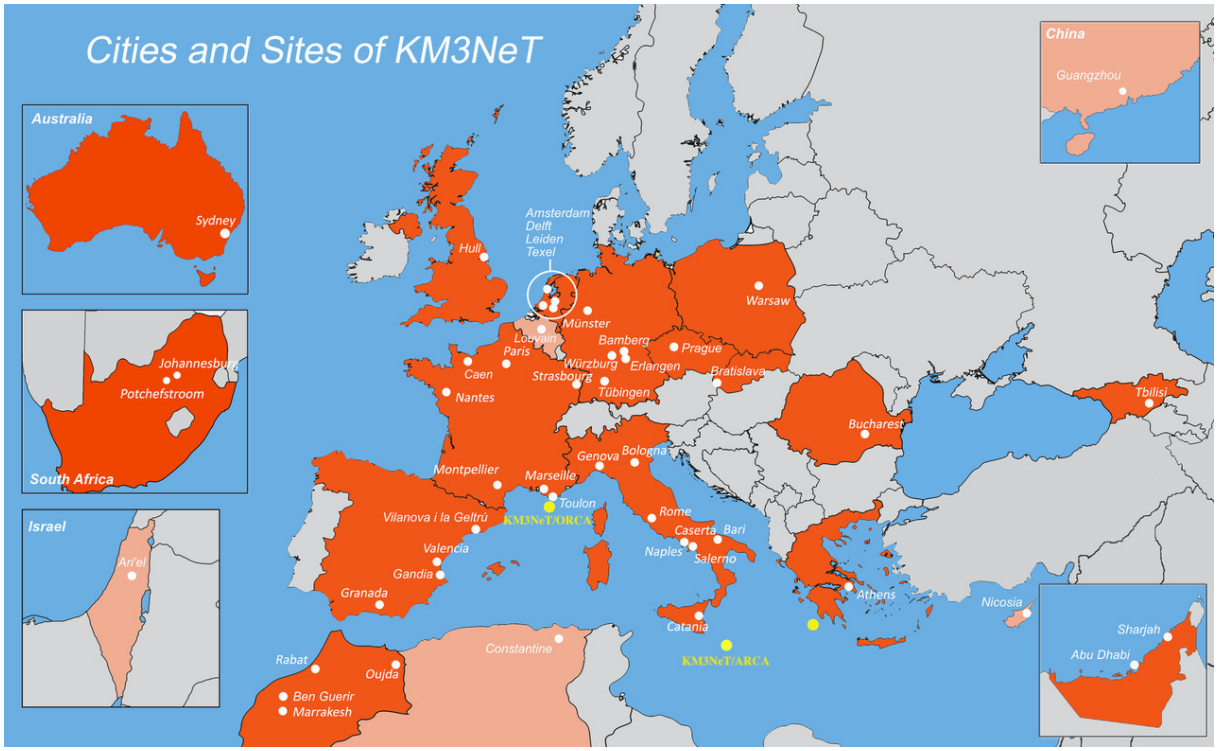

Figure 2.1: Location of the KM3NeT Collaboration institutes. The full KM3NeT members are shown with a bright orange color, and the associated members are reported with a pale color. The sites of the KM3NeT telescopes are indicated as yellow points. The yellow point near the coast of Greece is the proposed position of the possible third KM3NeT site. This picture is taken from the KM3NeT official website, https://www.km3net.org/.

This chapter starts with a description of the detection principle that is exploited in the KM3NeT experiment, Sec. 2.1. The detector design is discussed in Sec. 2.2. Topological signatures of the events that are registered by the KM3NeT detectors are reported in Sec. 2.3.

Finally, a brief discussion of the other neutrino telescopes is presented in Sec. 2.4

2.1 Detection principle

2.1.1 Cherenkov radiation

The particle detection in KM3NeT is based on the observation of the Cherenkov radiation [81]. The phenomenon occurs when a charged particle travels through a medium transparent to light at a speed that is greater than the speed of light in that medium.

The Cherenkov radiation is a joint emission of atoms of the medium located along the trajectory of the particle and polarized by its electric field. The wavefront of the radiation is the surface of a cone, the vertex of which is the particle, and the axis is its trajectory. The schematic illustration of the Cherenkov radiation induced by a charged particle with a speed $\vec{v}$ is presented in Fig. 2.2. This figure can be used to calculate the opening angle of the cone, θ_{Ch}. The spherical wave emitted at point A reaches point B when a charged particle is at point C. Therefore, the cosine of θ_{Ch} is

$$\cos\theta_{\text{Ch}} = \frac{AB}{AC} = \frac{tcn}{tv} = \frac{1}{\beta n}, \tag{2.1}$$

where t is the time needed for the particle to travel the distance AC and the wave to travel AB, n is the medium refractive index, and $\beta = v/c$ is the ratio of the velocity, v, of the charged particle to the speed of light in vacuum, c. The seawater refractive index is around 1.38 [82]. Hence, the angle of the Cherenkov cone for relativistic particle ($\beta \approx 1$) in seawater is 43.6°. The Cherenkov light wavelength in water lays in the visible blue - ultraviolet part of the spectrum.

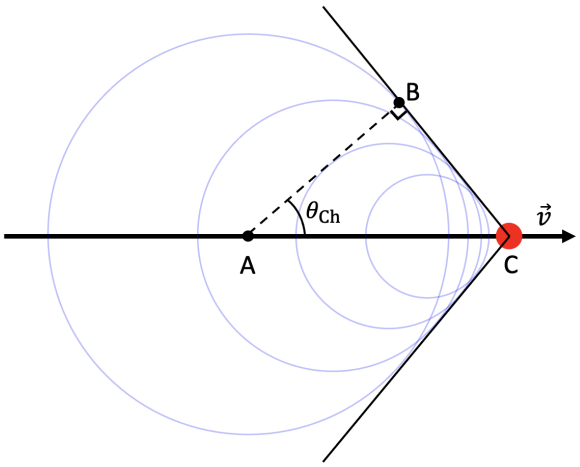

Figure 2.2: Sketch of the Cherenkov radiation. Charged particle (red circle on the plot) travels with a speed, $\vec{v}$, that is greater than the speed of light in the medium. The angle of the Cherenkov radiation cone is denoted as θ_{Ch}. Emitted Cherenkov light is illustrated as light blue circles.

The overwhelming majority of charged particles that are detected by the KM3NeT neutrino telescopes are atmospheric muons. These muons originate from EAS that are caused by the interactions of CRs with the atmosphere as discussed in Chapter 1. High-energy (TeV) muons

may travel several kilometers in water and reach the depth of the KM3NeT telescope. The mean free path length of muons in water as a function of their energy is presented in Fig. 2.3. Detailed discussion on the muon energy losses in water is reported in Chapter 3. The study of atmospheric muons is the main subject of this work since these particles provide information about the CR properties.

For neutrino studies, however, atmospheric muons are the main source of background. The neutrino observations are possible thanks to the charged particles that originate from the neutrino interactions with matter in the telescope sensitive volume or its vicinity. The neutrino interactions are discussed in Sec. 2.1.2.

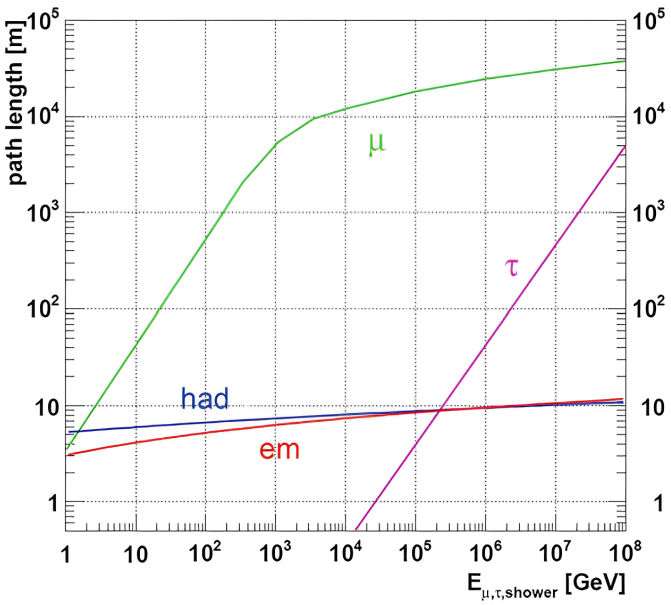

Figure 2.3: Mean free path of muons in water as a function of their energy (green line). The paths of other charged particles that are produced in the neutrino interactions are shown for comparison: the purple line is for tau leptons, and the red and blue lines are for the electromagnetic and hadronic showers, correspondingly. This figure is taken from [22].

2.1.2 Neutrino interaction with matter

Interactions of neutrinos with matter occur through the exchange of weak bosons. The interactions may happen due to the exchange of the charged bosons, $W^{\pm}$, the so-called Charge Current (CC) interactions, or via the exchange of the neutral boson, Z^0, the Neutral Current (NC) interactions. In the CC reactions, a charged lepton of the corresponding neutrino flavour is produced. As for the NC reactions, the final state lepton remains the neutrino of the same flavour. Examples of the CC and NC interactions are presented in Fig. 2.4.

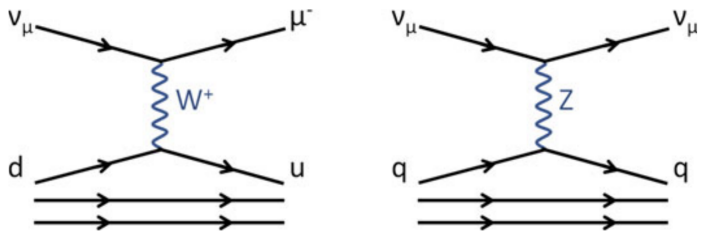

Figure 2.4: Feynman diagrams for the CC (left plot) and NC (right plot) muon neutrino interactions. The figure is taken from [21].

For the neutrino energies in the range that is of interest in the KM3NeT experiment (GeV-PeV), several interaction categories can be distinguished that are briefly described below. The cross-section for these processes is shown in Fig. 2.5.

Elastic and quasielastic scattering

The interaction between neutrino and an entire nucleon can lead to elastic scattering, causing the release of a nucleon or multiple nucleons from the target. In the case of CC neutrino scattering, this process is called quasielastic scattering, while in the case of NC interactions, it is known as elastic scattering [83].

Resonance production

Excitation of the target nucleon by incoming neutrino may lead to the formation of baryon resonances (Δ or N^*) [84]. The resonances decay into different combinations of nucleons and mesons.

Deep inelastic scattering

Neutrinos with energies above 10 GeV start to interact with the constituents of nucleons, quarks and gluons, which may lead to the formation of jets and hadronic showers [85].

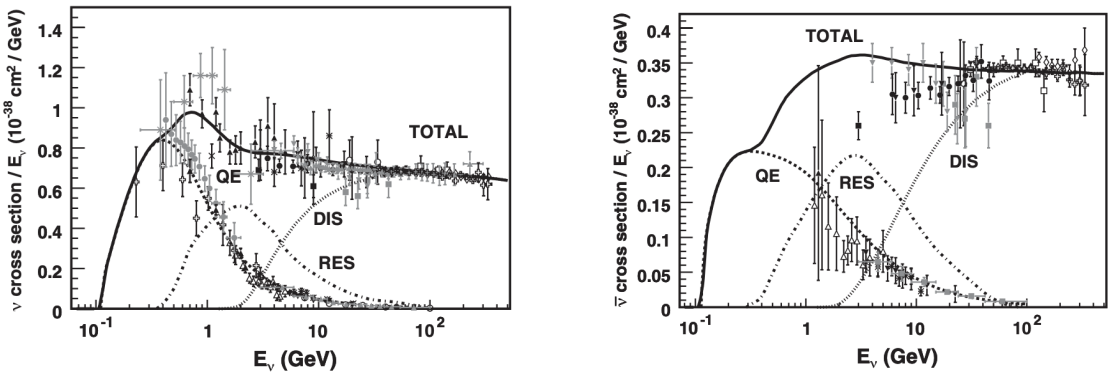

Figure 2.5: Total neutrino (right plot) and antineutrino (left plot) cross sections for the CC interactions divided by neutrino energy (solid line). The data points are shown with different markers. Lines represent the contributions from different processes: quasielastic scattering (dashed), resonance production (dot-dashed), and deep inelastic scattering (dotted). The figure is taken from [83].

2.2 Detector design

2.2.1 PMTs of the KM3NeT experiment

In the KM3NeT experiment, photons of the Cherenkov light are detected by an array of three-inch PhotoMultiplier Tubes (PMTs). The PMTs have a convex bialkali photocathode, with a diameter of 80 mm, and a 10-stage dynode structure. Around the head of each PMT, polished metal rings are placed at an angle of 45 degrees providing a 92% reflectance for photons in the wavelength range 375-500 nm. The metal rings allow to increase the photon acceptance by 20-40%, with most of the gain attained in the forward direction [86].

When a photon hits the PMT's photocathode, it can be absorbed and release an electron through the photoelectric effect. The probability of the photoelectric effect to occur for a certain PMT is called quantum efficiency. The efficiency of PMTs used in the KM3NeT telescopes (Hamamatsu PMTs [87]) is shown in Fig. 2.6. The first released electron is then accelerated by an electromagnetic field towards the PMT dynode and causes the emission of additional electrons. There are ten dynodes in total in Hamamatsu PMTs with the electric potential increasing from one dynode to the next. Thus, the interactions of electrons with each dynode lead to a cascade of electrons, and the original signal is amplified by a factor of more than 10^6 [87]. The amplified electron cascade reaches the anode that generates an output electrical pulse. If the amplitude of the pulse exceeds the predefined threshold then the signal is recorded. In particular, the beginning time of the signal and the timespan in which the amplitude was over the threshold (Time-Over-Threshold, ToT) are saved. This information together with the information about which PMT has recorded the signal is called a "hit".

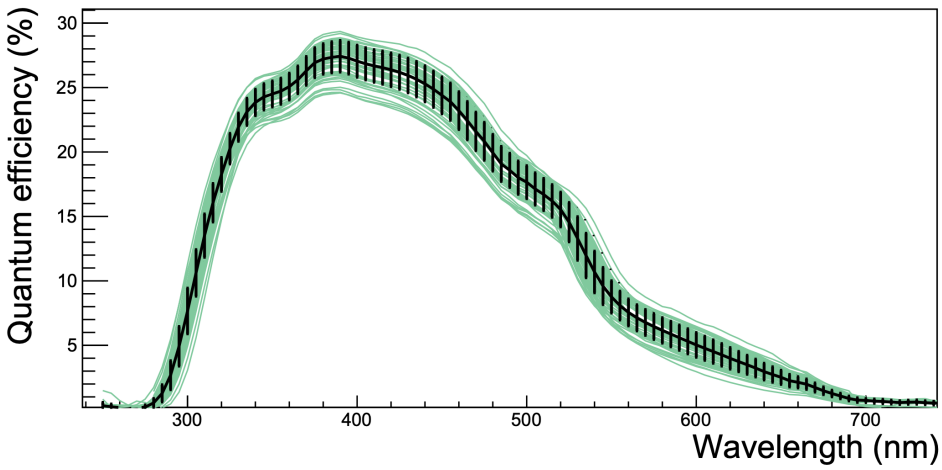

Figure 2.6: Quantum efficiency of the KM3NeT PMTs as a function of the light wavelength. Each green line corresponds to one of the 56 PMTs used in the measurements. The black line is the mean value for each wavelength. The vertical error bars indicate one standard deviation. The figure is taken from [87].

For the KM3NeT PMTs, the time interval between the moment a photon interacts with the photocathode until the cascade of electrons reaches the anode is around 30 ns [87]. This interval is referred to as the transit time of a PMT. The left plot in Fig. 2.7 illustrates the probability density function representing the transit time distribution for a typical KM3NeT PMT. The spread around the average transit time, known as the transit time spread, is about 2 ns. This spread is the main source of uncertainty in determining the arrival time of photons.

In addition to the main peak, there is a secondary peak in the transit time distribution occurring between 40 and 65 ns. This peak is caused by delayed pulses, originating from a secondary electron that back-scatters from the first dynode [87]. The back-scattered electron is then re-accelerated towards the first dynode, resulting in a delayed pulse, typically characterized by a lower amplitude compared to the main pulse. Another reason for the delayed pulse is photoelectrons emitted from a location on the photocathode where the electric field strength is relatively weak. Consequently, the released photoelectrons experience a significantly longer drift time. Also, there is a pulse with a small amplitude and a brief transit time in the transit time distribution, named prepulse. It occurs when photons release a photoelectron from one of the first dynodes, rather than from the photocathode.

A typical PMT pulse, as measured in a laboratory, is shown on the right plot in Fig. 2.7. The horizontal line represents the predefined threshold voltage.

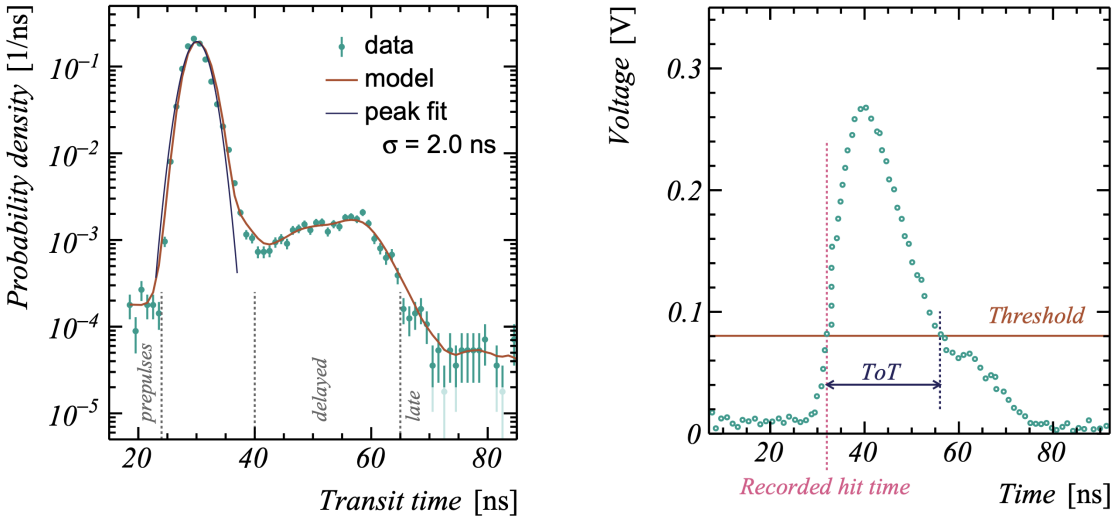

Figure 2.7: The left figure represents the transit time distribution of the KM3NeT PMTs. The right figure shows the typical recorded PMT pulse. The figures are taken from [88].

A set of signal hits which are pair-wise causally connected form a "cluster". If a sufficiently large cluster is found the event is triggered. In order to reduce the trigger rate due to pure noise and reduce computing time, the triggers take into account the fact that the hit probability decreases with distance away from the photon emission position. This is implemented by assuming a maximal photon travel distance. This reduces the number of DOMs to be considered and the maximal allowed time window for causally connected hits. Hence, an improvement of the signal-to-noise ratio compared to the general causality relation can be obtained. Depending on the assumed event topology, the relations that follow from causality, i.e. the matching condition for clustering, are different for the track-like and shower-like events that are described below in Sec. 2.3.

2.2.2 Digital Optical Module

The PMTs are placed in a pressure-resistant 17-inch diameter glass sphere, called Digital Optical Module (DOM) [79], Fig. 2.8. Each DOM houses 31 PMTs and their associated readout electronics. The PMTs are arranged in five rings of six PMTs and a single PMT at the bottom (south pole) of the DOM pointing downwards.

In addition to the PMTs, every DOM contains calibration tools, power-related electronics, and a Central Logic Board (CLB). The CLB collects all information produced by the PMTs and other instruments such as piezo sensors, compass/tiltmeters, nanobeacons, humidity sensors, and temperature sensors, and transmits it to the control station [89]. Piezo sensors which receive acoustic signals from acoustic emitters placed on the sea floor together with compass/tiltmeters serve as instruments for the DOM position calibration [86]. Nanobeacons are used in order to calibrate the detector elements in time [82].

The usage of multi-PMT DOMs instead of traditional optical modules with single large PMTs like the ones used in ANTARES [90] or IceCube [91] brings several advantages. The multi-PMT configuration allows a larger photo-cathode area per DOM and wider angular coverage. Also, it is possible to better eliminate the background by using the coincidences between different PMTs inside each DOM, which is essential for the core-collapse supernova studies [86].

Figure 2.8: Picture of the KM3NeT DOM fixed on the two parallel Dyneema® ropes. This picture is taken from the KM3NeT official website, https://www.km3net.org/.

2.2.3 Detection Unit

A detection unit (DU) consists of a pair of long Dyneema® ropes with 18 DOMs attached to them trough titanium collars. The DU is secured to the sea floor with an anchor and it has a buoy at the top to keep the DU in a vertical position. The anchor is the interface with the seabed infrastructure housing an interlink cable and a base module. The module is connected to a cable running to shore using a network of junction boxes.

The vertical spacing between the DOMs and the horizontal distance between each DU is different for the KM3NeT/ARCA and KM3NeT/ORCA telescopes as described below.

2.2.4 Configuration of the KM3NeT telescopes

The KM3NeT/ARCA (Astroparticle Research with Cosmics in the Abyss) telescope is being built near the coast of Sicily (Italy), about 100 km offshore Portopalo di Capo Passero. Its main scientific goal is to study the high-energy cosmic neutrinos in the TeV-PeV range [92]. In its final configuration, the KM3NeT/ARCA detector will consist of two so-called "building blocks", each comprising 115 DUs. The horizontal spacing between the DUs is around 90 m and the distance between the DOMs on each DU is 36 m. The radius of the one KM3NeT/ARCA building block is ∼500 m.

The KM3NeT/ORCA (Oscillation Research with Cosmics in the Abyss) detector is smaller and denser with respect to KM3NeT/ARCA since its main goal is the study of atmospheric neutrino oscillation and neutrino mass hierarchy [93]. Hence, a lower energy threshold (GeV) for the neutrino detection is needed. The detector is located offshore the coast of France, about 40 km away from Toulon. The KM3NeT/ORCA telescope will comprise one building block with 115 DUs. The distance between the DUs is around 20 m and the DOMs on each DU are 9 m apart.

The KM3NeT/ARCA and KM3NeT/ORCA telescopes in their final configurations are sketched in Fig. 2.9. The location of DUs that were installed as of August 2023 relative to one building block configuration is shown in Fig. 2.10: 21 DUs installed with 19 taking data in KM3NeT/ARCA, and 16 DUs out of 18 DUs deployed are taking data in KM3NeT/ORCA. The analysis presented in this work was performed with the data taken by the KM3NeT/ARCA and KM3NeT/ORCA telescopes in six DU configuration at each site. In the following, this configuration is denoted

as ARCA6 and ORCA6 for two detectors, correspondingly. The ARCA6 and ORCA6 detector layouts are presented in Fig.2.11.

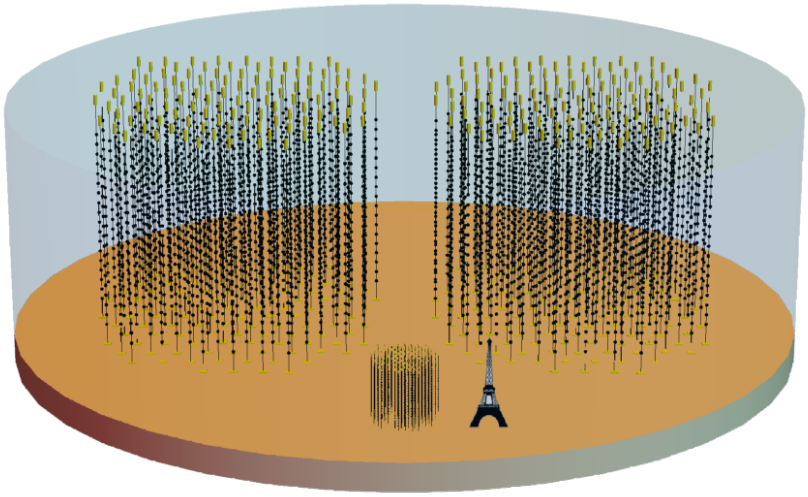

Figure 2.9: Sketch of the KM3NeT telescopes. The top part of the figure shows the two KM3NeT/ARCA building blocks while the central bottom part illustrates the KM3NeT/ORCA detector. Vertical lines are the DUs. Every sphere represents a DOM, the buoy and the base module are shown in yellow at the top and bottom of the DUs, correspondingly. The Eiffel Tower is shown for the size comparison.

Figure 2.10: Installed DUs of the KM3NeT/ARCA (left plot) and the KM3NeT/ORCA (right plot) telescopes as of August 2023. DUs that take data are shown in green, DUs that were installed but currently experience issues with the data acquisition are in red. CTF stands for a cable termination frame and JB denotes a junction box [79].

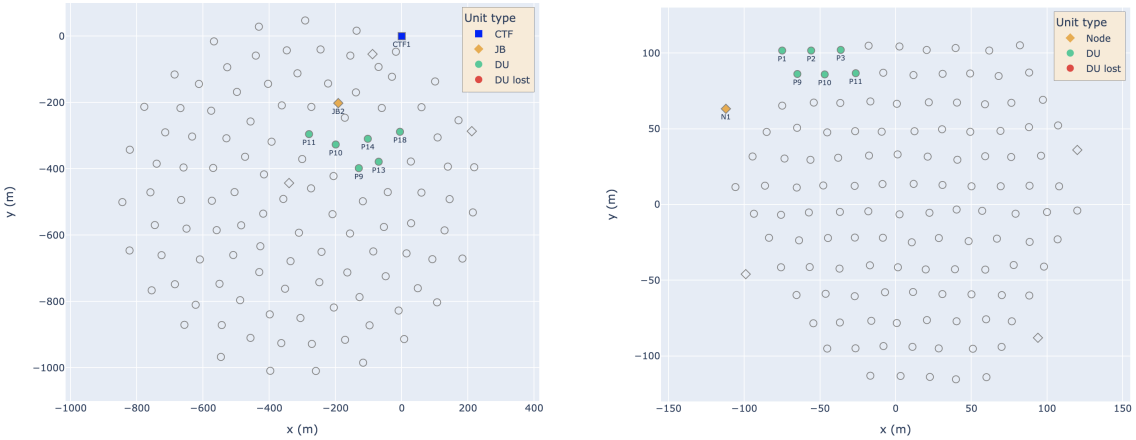

Figure 2.11: The KM3NeT/ARCA (left figure) and the KM3NeT/ORCA (right figure) detector configuration which were used in this work. Working DUs are shown as green circles. Blue rectangle is a cable termination frame and orange rhombus is a junction box.

2.3 Event topology

Different types of particles produce varying event signatures inside a detector. Here below different event topologies are discussed.

Track-like events

The track-like events correspond to muons crossing the sensitive volume of the detector. The events that are the golden channel for neutrino studies are muon tracks induced by the CC interactions of muon (anti-)neutrinos. Reconstruction of the direction of such events is precise since they leave a long track inside the detector and the Cherenkov light produced by their passage triggers many PMTs. Although, the energy reconstruction is less accurate since not all the particle energy is deposited inside the detector. The direction and energy reconstruction capabilities are discussed in Chapter 3.

Other particles which also leave the track-like signatures in the KM3NeT telescopes are atmospheric muons. The study of these particles is the main goal of this thesis.

The track-like event signatures are illustrated on the first two schemes of Fig. 2.12.

Shower-like events

Shower-like (or cascade-like) events are caused by the NC interactions of neutrinos of all three flavours and by the CC interactions of the electron neutrinos. In both cases, the electromagnetic shower from the hadronic cascade is created and can be detected by the PMTs. The energy of the shower-like events is well reconstructed since the energy deposit is fully contained in the detector. The direction reconstruction is less precise though since the shower-like events usually trigger only the neighbouring DOMs. The shower-like event topology is presented in the third scheme of Fig. 2.12.

Also, there is another class of events caused by the CC interaction of the high-energy (PeV) tau neutrinos with matter [94]. Such interactions are characterized by the double-cascade signature. Firstly, the tau neutrino CC interaction leads to the tau lepton production and the hadronic

cascade. Then, the high-energy tau lepton travels some distance in water (∼50 m for 1 PeV tau lepton as shown in Fig. 2.3) before it decays producing another cascade. If the distance between the two cascades is long enough for their separation then the so-called "double-bang" event can be identified as shown in the very right plot in Fig. 2.12.

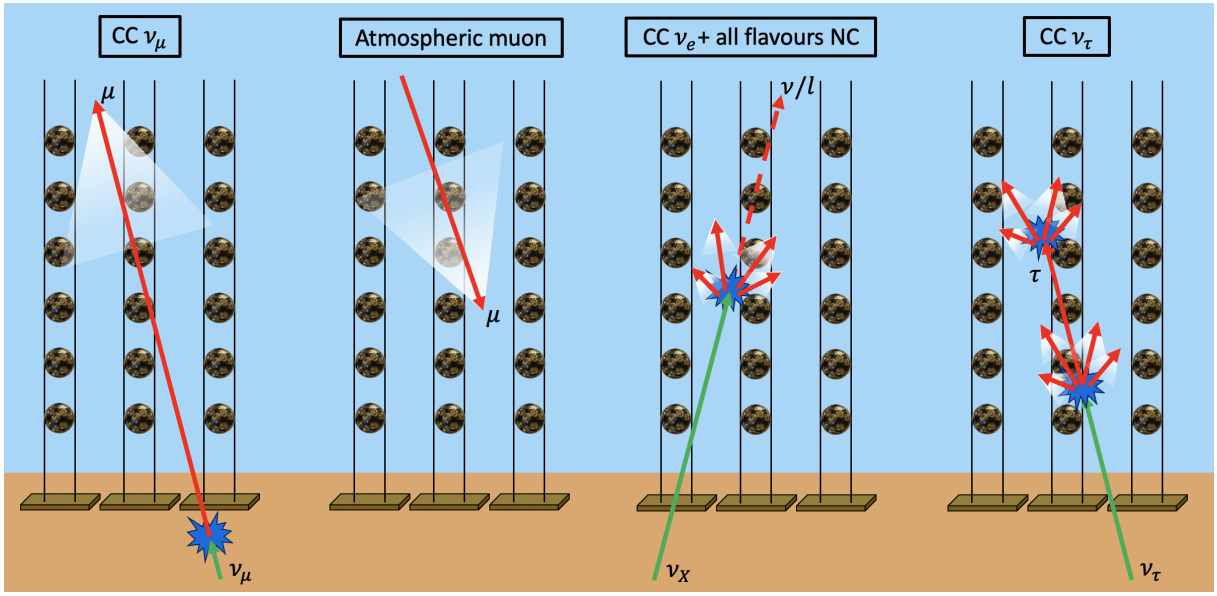

Figure 2.12: Topologies of the events that can be detected by the KM3NeT neutrino telescopes.

Algorithms that are used in the KM3NeT experiment to reconstruct the aforementioned events are discussed in Chapter 3.

2.4 Other neutrino telescopes

Besides the KM3NeT experiment, there are several large-volume detectors that aim to measure the neutrino properties using Cherenkov radiation. These telescopes are discussed briefly here below. Together with the KM3NeT project, these experiments comprise the Global Neutrino Network that aims for a closer collaboration and a coherent strategy among the large-volume neutrino telescopes [95].

ANTARES

The ANTARES neutrino telescope [90] is the predecessor of the KM3NeT project. It was also located in the Mediterranean Sea near the coast of France, close to the site of the KM3NeT/ORCA detector. ANTARES was operational in its full configuration from May 2008 until February 2022. The detector was comprised of 12 DUs and had an instrumented volume of more than 0.01 km^3. Each DU included up to 75 optical modules with a single 10-inch PMT. The successful deployment and operation of the ANTARES telescope demonstrated the viability of conducting neutrino studies with large-volume detectors in the deep sea.

Baikal-GVD

The Baikal-GVD neutrino telescope is currently under construction in Lake Baikal in Rus-

sia [96]. The detector design includes clusters of eight DUs each. Every DU is composed of 36 single PMT optical modules. The deployment of the facility began in the spring of 2015. The first construction phase is planned to be finished in 2024 with 15 clusters deployed, the detector will reach an effective volume of 0.75 km^3.

IceCube

The IceCube neutrino observatory is located deep in the Antarctic ice at the South Pole [97]. The IceCube detector is continuously taking data in its full configuration since 2011. The telescope is comprised of 5160 optical modules with a single PMT in each. The modules are placed on 86 vertical DUs located at depths between 1450 m and 2450 m. IceCube includes also a smaller and denser array of optical modules that allows measuring neutrinos with lower energies (> 10 GeV), called DeepCore [98]. Additionally, an array of Cherenkov tanks filled with clear ice is located at the surface for the EAS detection, IceTop [99].

3 Simulation of atmospheric muons for the KM3NeT neutrino telescope

The simulation of muons for the KM3NeT experiment starts in the upper layers of the atmosphere and ends deep underwater. It can be divided into five steps. The first step is to simulate the interactions of the primary CRs with the air nuclei and the subsequent propagation, interaction, and decay of the secondary particles. The result is the muon distribution at sea level. This step is performed with the full MC simulation code, CORSIKA [66]. The description of the CORSIKA simulation is presented in Sec. 3.1-3.3.

The second step of the simulation is the propagation of muons in water down to the KM3NeT detectors, Sec. 3.4. The third one is the generation of the Cherenkov light from muons and its detection by the telescope PMTs, Sec. 3.5. Then, the detector response to the light is simulated together with the optical background, Sec. 3.6. Finally, the reconstruction of muon tracks is performed, Sec. 3.7. Results of the atmospheric muon simulations are reported in Sec. 3.8.

3.1 CORSIKA simulation

CORSIKA version 7.7410 was used for the MC simulation of EAS. It was initially developed to perform simulations for the KASCADE experiment [100] at Karlsruhe. Nowadays, CORSIKA is a simulation tool used by many experiments that perform the CR studies [62, 101, 64].

There are several inputs that are needed for the CORSIKA simulation. Firstly, the properties of the primaries have to be specified. In particular, the nuclei that will be assumed as primary CRs, their energy, the zenith angle range, and the number of showers to generate, Sec. 3.1.1. Secondly, there are models that describe the interactions and atmosphere density profile that must be specified, Sec. 3.1.2 and Sec. 3.1.3, correspondingly.

3.1.1 Properties of the primaries

Muons detected by the KM3NeT telescopes originate from the interactions of primary CRs that have energies in a certain range. The CR energy range is limited on the lower end of the spectrum since muons from EAS must have sufficient energy to reach the depths of the detectors. This energy is around 500 GeV [102] and the vast majority of muons reaching the KM3NeT detectors has energies in the TeV range. Hence, the lower limit on the primary energy was set to 1 TeV per nucleon in the simulation. Fig. 3.1 shows the sea level flux of muons that reach the ORCA6 detector as a function of their energies. The highlighted area indicates the 90% fraction of events counting from the maximum of the distribution. The energy range of the fraction spans from 0.8 TeV to 4.5 TeV. The upper limit arises due to the fast decrease of the CR flux with the energy.

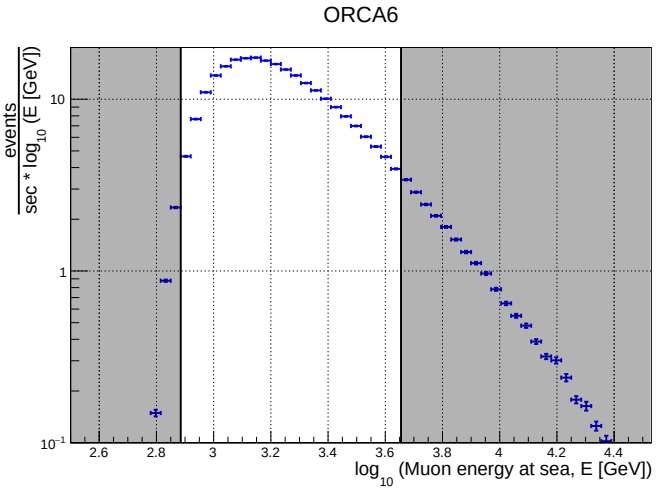

Figure 3.1: Sea level rate of generated muons that reach the ORCA6 depth as a function of their energy. The highlighted area illustrates the energy range (0.8 - 4.5 TeV) that includes a 90% fraction of events.

Five nuclei were used as primaries in the simulation: hydrogen ($^{1}_{1}$H), helium ($^{4}_{2}$He), carbon ($^{12}_{6}$C), oxygen ($^{16}_{8}$O), and iron ($^{56}_{26}$Fe). Other primaries were taken into account by enlarging the flux weights of C, O, and Fe according to the flux of nuclei that were missing in the simulations.

The primary energy range of the simulations was divided into 3 sub-ranges (named "TeV_low", "TeV_high", and "PeV") to have sufficient statistics in each sub-range. A summary of the production energy ranges is reported in Table 3.1. The number of generated showers in each production and per each primary is listed in Table 3.2.

Nucleus	Energy range [TeV]		
	TeV_low	TeV_high	PeV
p	1 - 6	6 - 1.1 $\times$ 10^3	1.1 $\times$ 10^3 - 9 $\times$ 10^4
He	4 - 10	10 - 1.1 $\times$ 10^3	1.1 $\times$ 10^3 - 9 $\times$ 10^4
C	12 - 30	30 - 1.1 $\times$ 10^3	1.1 $\times$ 10^3 - 9 $\times$ 10^4
O	16 - 30	30 - 1.1 $\times$ 10^3	1.1 $\times$ 10^3 - 9 $\times$ 10^4
Fe	56 - 100	100 - 1.1 $\times$ 10^3	1.1 $\times$ 10^3 - 9 $\times$ 10^4

Table 3.1: Energy range of primaries used in the CORSIKA simulation.

Nucleus	Number of generated showers		
	TeV_low	TeV_high	PeV
p	3 $\times$ 10^9	3 $\times$ 10^9	4 $\times$ 10^7
He	2 $\times$ 10^9	2 $\times$ 10^9	4 $\times$ 10^7
C	1 $\times$ 10^9	7.5 $\times$ 10^8	2.5 $\times$ 10^7
O	1 $\times$ 10^9	7.5 $\times$ 10^8	2.5 $\times$ 10^7
Fe	5 $\times$ 10^8	2 $\times$ 10^8	2 $\times$ 10^7

Table 3.2: Number of showers generated in the simulation.

3.1.2 Hadronic interaction models

In CORSIKA, the URQMD (Ultra-relativistic Quantum Molecular Dynamics) 1.3 model [103] was used to perform the elastic and inelastic interactions of hadrons below 80 GeV in air. As described in Sec. 3.1.1, the low-energy threshold for muons at the sea level is around 500 GeV. Hence, the low-energy interaction model is of less importance.

Interactions of hadrons with protons and nuclei are well studied up to several hundreds of GeV (in target rest frame) at fixed target detectors [69]. For the higher energies, it is necessary to rely on model extrapolations from collider experiments. Muons that are reconstructed in the KM3NeT telescopes originate from primary CRs with energies starting from several TeV up to PeV as discussed below in Sec. 3.8. The LHC energy of 13 TeV in the center-of-mass frame corresponds to the target rest frame energy of 90 PeV which is above the upper threshold of the KM3NeT energy range that contains 90% of events. Hence, one might assume that all the properties of the interactions of protons with air nuclei have been already measured and that there should be no tensions and uncertainties caused by the interaction models. However, this is not true. Most LHC experiments focus their instrumentation on the mid-rapidity region where new heavy particles such as the Higgs boson are best observed. But muons that are seen by the KM3NeT detectors lay in the very forward region of rapidities. Fig. 3.2 demonstrates pseudorapidity values of muons reaching the ORCA6 (left) and ARCA6 (right) telescopes. Pseudorapidity converges to the definition of rapidity for highly relativistic particles. On the figure below, it is defined as $\eta = -\ln[\tan(\frac{\theta}{2})]$, where θ is the angle between the primary particle and secondary muon at the sea level. The peak of the distributions is located at $\eta \approx 9$.

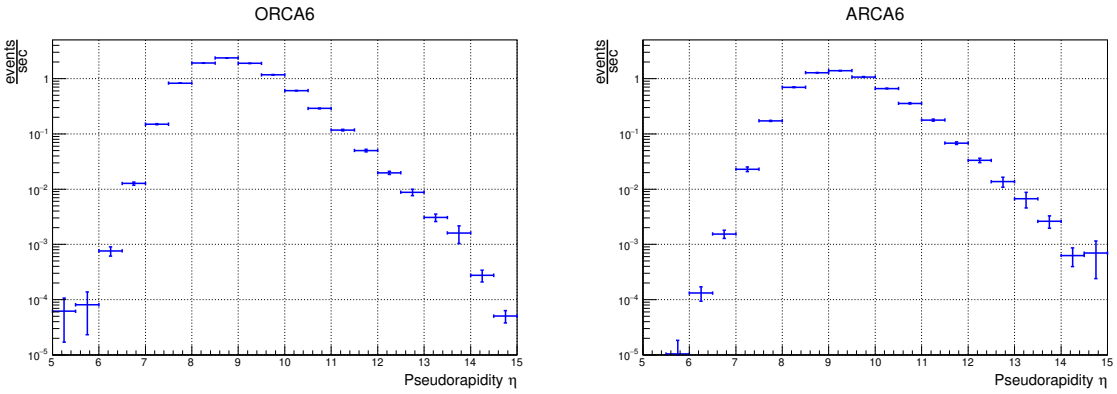

Figure 3.2: Pseudorapidity distribution of muons reaching the ORCA6 (left plot) and ARCA6 (right plot) detectors. The value of pseudorapidity is derived using the angle between the primary nuclei and muons at the sea level.

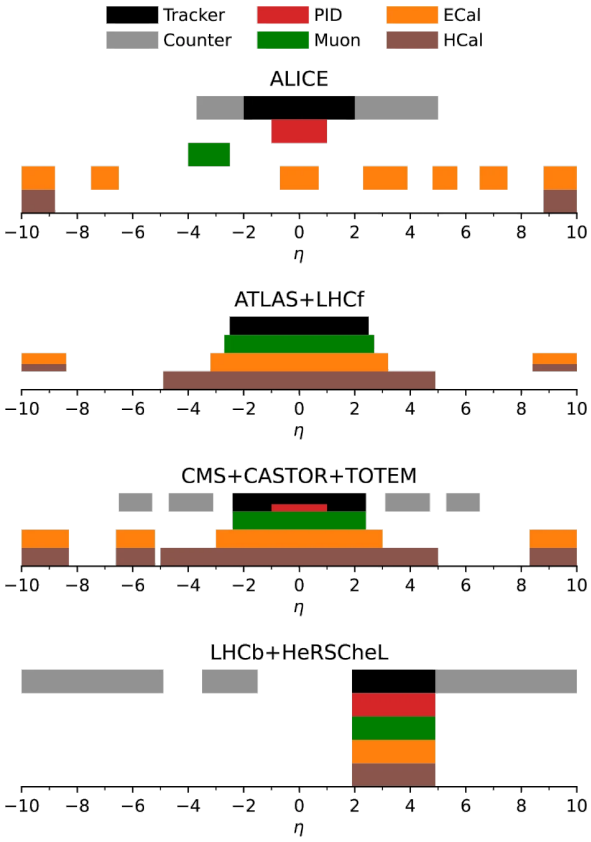

Figure 3.3: Acceptances in terms of pseudorapidity of the LHC experiments ALICE [104], ATLAS [105], LHCf [106], CMS with its CASTOR forward calorimeter [107], TOTEM [108], and LHCb [109] with forward scintillators HeRSCheL [110]. In the legend, a tracker follows individual particles in a magnetic field, a counter measures particle densities in η-intervals. Muon stands for a special muon tracker, PID refers to the ability to identify individual particles, ECal and HCal are electromagnetic and hadronic calorimeters, respectively. The figure is taken from [20].

In Fig. 3.3, the acceptances of the LHC experiments as a function of pseudorapidity is shown. As it can been seen from this plot, the LHC experiments cover the pseudorapidity region above 8. However, none of the experiments has been designed to perform precision tracking and particle identification at forward rapidities higher than 5. Moreover, the most common interaction in an air shower is $\pi - \mathrm{N}$, and the most important first interaction is $p - \mathrm{N}$. These reactions are different from both $p - p$ and $p - \mathrm{Pb}$ which measurements had been performed at LHC in Run 1 and 2. Hence, there is still a remaining uncertainty in the extrapolation of the inelastic cross-section from $p - p$ to $p -$ air as demonstrated in Fig. 3.4 [20]. This uncertainty could be reduced with future data from $p - \mathrm{O}$ and $\mathrm{O} - \mathrm{O}$ collisions that were proposed for Run 3 of LHC [111].

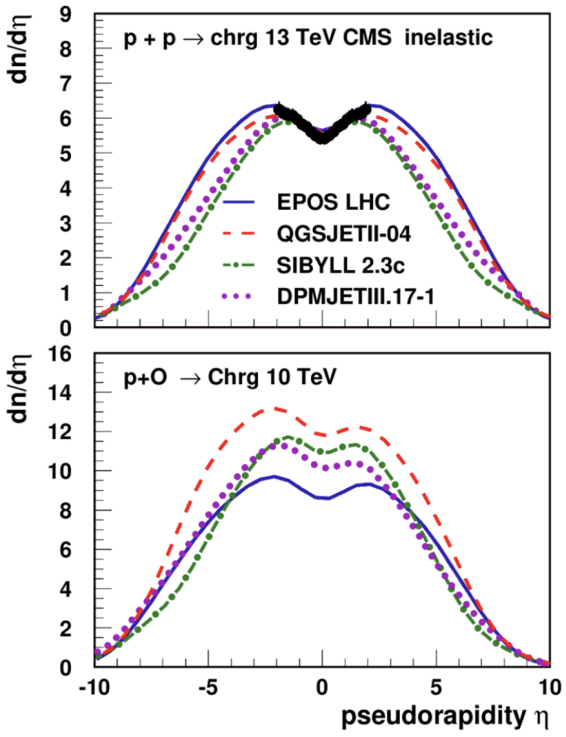

Figure 3.4: Number of charged particles obtained with different hadronic generators as a function of pseudorapidity in $p-p$ interactions at 13 TeV (top plot) and $p-\mathrm{O}$ at 10 TeV (bottom plot). Models are in agreement at a level below 5% for $p-p$ collisions at mid-rapidity, but the spread in $p-\mathrm{O}$ collisions is 50%. The figure is taken from [20].

There are several post-LHC high-energy hadronic interaction models available in CORSIKA, namely EPOS [71], QGSJETII-04 [70], Sibyll 2.3d [69], and DPMJET III [112]. Among these models, only the DPMJET III and Sibyll 2.3d include the charm hadron production which is essential for some KM3NeT analyses, e.g. search for the prompt muon component in the atmospheric muon flux [113]. However, DPMJET III was still under development at the time of writing this work. Hence, the Sibyll 2.3d model was chosen for the simulations. Differences in the high-energy muon flux induced by choosing the different hadronic interaction models were treated as systematic uncertainties.

Core features of Sibyll are based on the dual parton model [114] and the minijet model [115]. Its basic goal is to account for the main features of strong interactions and hadronic production as needed for understanding air-shower cascades. Therefore, it focuses on the description of particle production at small angles and on the flow of energy in the projectile direction. Rare processes, such as the production of particles or jets at large transverse momentum or electroweak processes, are either included approximately or neglected.

3.1.3 Atmosphere

The atmosphere is divided into five layers in CORSIKA. The atmospheric overburden as a function of the altitude above the sea level, $T(h)$ [g/cm^2], is parametrized in each layer. For the first four layers, $T(h)$ is parametrized as an exponential function:

$$T(h) = a_i + b_i \cdot e^{-\frac{h}{c_i}}, 1 \leq i \leq 4, \tag{3.1}$$

while in the fifth layer the $T(h)$ dependence is linear:

$$T(h) = a_5 - b_5 \cdot \frac{h}{c_5}. \tag{3.2}$$

Here, i is the layer number, and a_i, b_i, and c_i are the fitting parameters.

NRLMSIS-2.0 [116] was used as an atmosphere model and its data were fitted to get the values of parameters. Since the atmospheric conditions vary depending on time and location, the fit was performed on the model predictions averaged over 3 years period (2019-2021) and over the ORCA and ARCA sites. Each of the 5 CORSIKA atmosphere layers was fitted separately. Each of the fits was bound at least from one side due to the requirement that the global $T(h)$ function must be continuous. The result is presented in Fig. 3.5. Values of fitted parameters are reported in Table 3.3. The atmosphere fit was performed by another colleague with whom the author of this thesis was developing the atmospheric muon simulation software in KM3NeT.

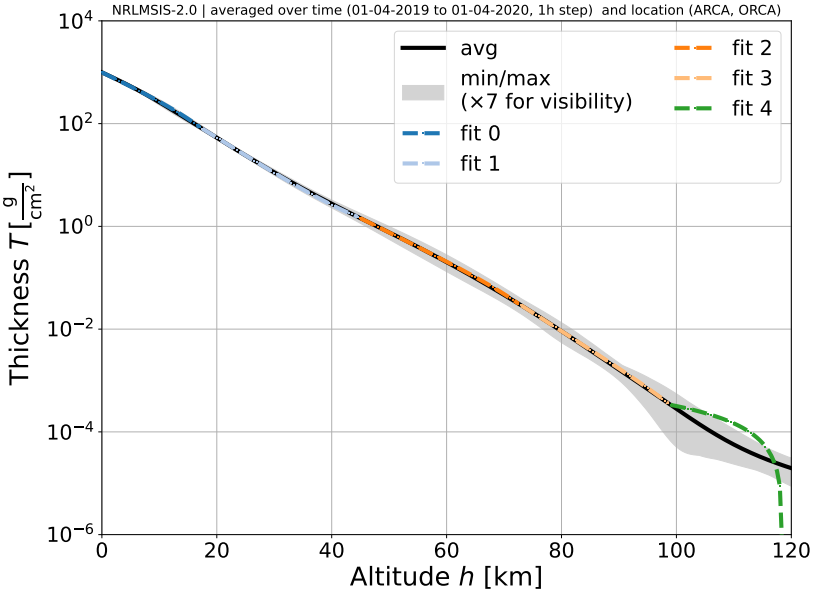

Figure 3.5: Fit of the atmospheric overburden, T, taken from the NRLMSIS-2.0 model as a function of the altitude, h, with Eq. 3.1 and 3.2. The figure is taken from [117]

Layer number	Height	Fitted a value	Fitted b value	Fitted c value
1	0 - 17.5 km	-58.45	10.71×10^2	8.65×10^5
2	17.5 - 45 km	0.50	13.81×10^2	6.23×10^5
3	45 - 73 km	-0.015	4.50×10^2	7.90×10^5
4	73 - 101.3 km	-4.29×10^{-5}	5.71×10^3	5.99×10^5
5	101.3 - 125 km	3.0×10^{-3}	-38.86	-1.41×10^{11}

Table 3.3: Values of the parameters resulting from the $T(h)$ fit.

3.2 Cosmic Ray composition model

The most recent model of the CR mass composition is the Global Spline Fit (GSF) [19]. The model is a purely data-driven parametrization of the CR flux with the only assumption that the flux is smoothly varying. The parametrization is done with a linear combination of B-splines [118]. The GSF does not assume the flux components with power-law shape and rigidity-dependent cutoffs in contrast to other mass composition models [119, 120]. Hence, it does not try to explain the physical origin of the data, but describes the measurements.

The flux of primary nuclei is divided into four mass groups in the GSF model. The groups are split in roughly equal ranges in logarithmic mass number, $\ln A$, following measurements from EAS experiments. The groups are named after the element that has the largest contribution on the total flux in each group, the so-called leading element. There are the proton ($Z = 1$), helium ($Z = 2$), oxygen ($3 \leq Z \leq 10$), and iron ($11 \leq Z \leq 28$) mass groups.

The differential flux of the leading element as a function of rigidity, $J_L(R)$, is parametrized by a linear combination of splines. The splines are fitted to the data to get the coefficient values. The data is the combination of results obtained by the direct, HEAO [18], PAMELA [51, 121], AMS-02 [14, 15], CREAM-I and II [16, 17], and indirect, ARGO-YBJ [122], TUNKA [123, 124], IceCube [9], KASCADE-Grande (KG) [10, 11], Telescope Array (TA) [125], and the Pierre Auger Observatory (Auger) [12, 13], CR experiments.

Fluxes of other nuclei within each group as a function of rigidity, $J_i(R)$, are recalculated keeping the ratio, f_{iL}, to the leading element flux, $J_L(R)$, constant: $J_i(R) = f_{iL} \times J_L(R)$. This approximation is motivated by the low-energy data from the direct CR experiments. Fig. 3.6 demonstrates that the fluxes of elements within the mass group have roughly the same shape so f_{iL} can be treated as a constant.

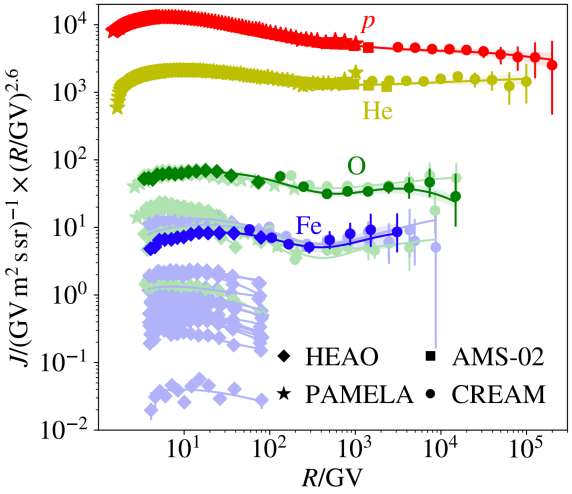

Figure 3.6: Fluxes of primaries as a function of rigidity as measured by the direct CR experiments. Pale colors show the fluxes of sub-leading group elements. The figure is taken from [19].

Since there are 5 primaries simulated in CORSIKA and 28 primaries available in the GSF model, the following approach was used to include all available nuclei. The proton and helium w_{CR} weights are taken directly from the GSF tables. The carbon w_{CR} weight is the sum of the GSF weights of nuclei with Z from 3 to 6, the oxygen weight is $w_{\mathrm{CR}} = \sum_{Z=7}^{10} w_{\mathrm{CR}}^{Z}$, and the iron weight is $w_{\mathrm{CR}} = \sum_{Z=11}^{28} w_{\mathrm{CR}}^{Z}$.

In Fig. 3.7, the total flux of primaries and the individual fluxes of nuclei used in the simulations as a function of primary energy, E, are shown. The flux was multiplied by $E^{2.6}$ to compensate for a fast drop of the flux with energy. The shaded areas illustrate the flux uncertainties reported in the GSF model.

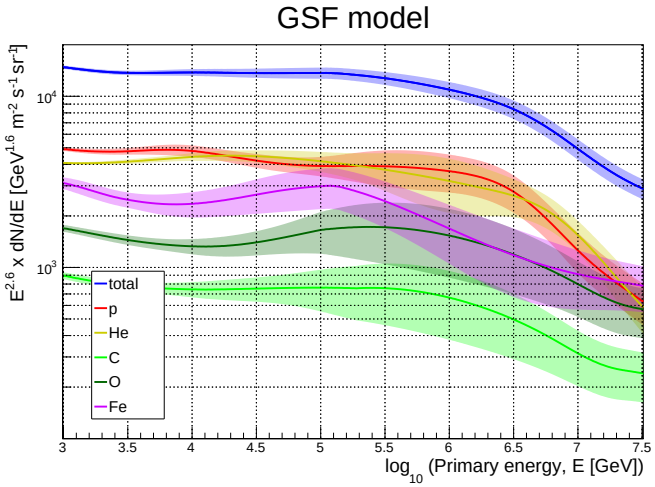

Figure 3.7: Total flux of primaries (blue line) together with the individual fluxes of the proton (red), helium (yellow), carbon (light green), oxygen (dark green), and iron (purple) primaries. Shaded areas represent the uncertainties from the GSF model.

3.3 Event weighting scheme

In order to have the flux of muons, one needs to assume a certain model of the CR mass composition as described in Sec. 3.2. The model defines a CR flux weight, w_{CR}, for each primary that depends on the type of nuclei and on the energy, E_{pr}. The unit of the w_{CR} weight is GeV$^{-1}\cdot$ m$^{-2}\cdot$ sec$^{-1}\cdot$ sr^{-1}. In order to have the rate of events [s^{-1}], the so-called generation weight must also be taken into account. The generation weight is defined as

$$w_{\mathrm{gen}} = S \cdot I_{\theta} \cdot I_{E_{\mathrm{pr}}} \cdot E_{\mathrm{pr}}^{\gamma}. \tag{3.3}$$

Here, S [m^2] is the sum of projected areas of the top and side of the detector *can*, cylinder surrounding the detector that is used as a generation surface. The can height and radius are larger than the detector dimensions by 4 light absorption lengths in the seawater (70 m $\times$ 4) to account for the light emitted by muon before reaching the detector. $I_{\theta} = 2\pi(\cos\theta_{\mathrm{min}} - \cos\theta_{\mathrm{max}})$ [sr] is the angular phase space factor with θ_{min} (θ_{max}) being the minimum (maximum) zenith angle of simulation, and $I_{E_{\mathrm{pr}}}$ is the energy phase space factor which is calculated as

$$I_{E_{\mathrm{pr}}} = \int_{E_{\mathrm{min}}}^{E_{\mathrm{max}}} E_{\mathrm{pr}}^{-\gamma} dE_{\mathrm{pr}} = \begin{cases} \frac{E_{\mathrm{pr}}^{1-\gamma}|_{\mathrm{max}} - E_{\mathrm{pr}}^{1-\gamma}|_{\mathrm{min}}}{1-\gamma} & \text{if } \gamma \neq 1 \\ \ln(\frac{E_{\mathrm{pr}}|_{\mathrm{max}}}{E_{\mathrm{pr}}|_{\mathrm{min}}}) & \text{if } \gamma = 1, \end{cases} \tag{3.4}$$

where γ is the simulation spectral index. The unit of the generation weight is GeV $\cdot$ m$^2\cdot$ sr. Then, to have the rate of muons, one needs also to account for the number of generated showers, $n_{\mathrm{gen\ showers}}$, per each primary and sub-production used in the CORSIKA simulation, the sub-productions were described in Sec. 3.1.1. Therefore, the final weight that must be applied to the events is

$$w = \frac{w_{\mathrm{CR}} \cdot w_{\mathrm{gen}}}{n_{\mathrm{gen\ showers}}}\ [\mathrm{sec}^{-1}]. \tag{3.5}$$

3.4 Muon propagation in water

CORSIKA simulation output is a binary Fortran file containing the distribution of muons at sea level. In order to propagate muons in water down to the KM3NeT detector cans, the gSeaGen code [126] was used. The code was modified for the muon propagation with PROPOSAL [127] since originally gSeaGen was developed as a GENIE-based [128] application for the neutrino simulation.

PROPOSAL is a MC code for the propagation of leptons and gamma-rays through media. It calculates the final position, direction, and energy of a particle given the corresponding initial condition and the distance of the propagation in the medium. Processes that determine the muon energy losses and scattering are described below.

Ionization losses in water are dominant for muons with energies less than $\sim$ 100 GeV, while the radiative losses prevail at higher energies, the left plot in Fig. 3.8. The energy loss rate per unit of path length may be expressed as $-dE/dx = a(E) + b(E)E$, where $a(E)$ incorporates the losses due to ionization, and $b(E)$ is the energy-scaled contribution from radiative processes. This equation illustrates the fact that, unlike the ionisation losses, the radiative losses increase proportionally with energy. Radiative losses include bremsstrahlung [129], e^+/e^- pair production [130], and photo-nuclear interactions [131]. The contributions of each processes to the $b(E)$ term are shown on the right plot in Fig. 3.8. Despite the energy loss calculations, PROPOSAL also takes into account the Landau–Pomeranchuk–Migdal effect [132].

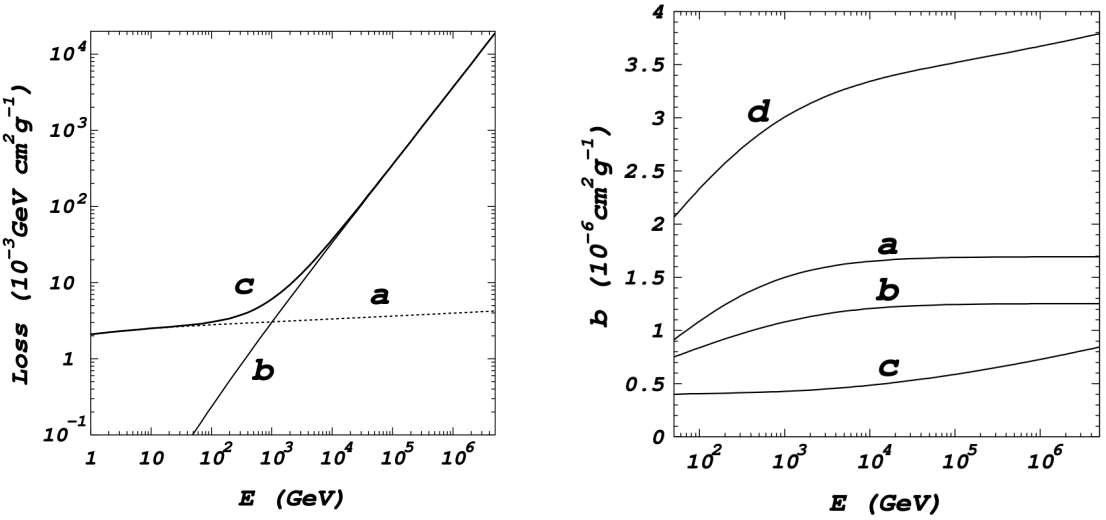

Figure 3.8: Left: mean muon energy losses in water. Curve a represents the ionization losses, curve b shows the radiative ones, and c are the total energy losses. Right: contributions to the radiative energy losses in water: a - e^+/e^- pair production, b - bremsstrahlung, c - photonuclear interactions, and d - sum of the radiative losses. The figure is taken from [133].

3.4.1 Ionization

Energy loss due to ionization per unit of length is described by the Bethe-Bloch formula:

$$\langle -\frac{dE}{dx} \rangle = K \frac{Z}{A} \frac{1}{\beta^2} [\frac{1}{2} \ln \frac{2m_e c^2 \beta^2 \gamma^2 Q_{\max}}{I^2} - \beta^2 - \frac{\delta}{2} + \frac{1}{8} \frac{Q^2_{\max}}{(\gamma m c^2)^2}] + \left| \Delta \frac{dE}{dx} \right| . \tag{3.6}$$

Here $K = 4\pi N_A r_e^2 m_e c^2$, N_A is Avogadro's number, r_e is the classical electron radius, $m_e c^2$ is the electron mass, Z and A are the charge and the atomic mass of medium, $\beta = v/c$ and $\gamma = 1/\sqrt{1-\beta^2}$ are the usual kinematic variables. $Q_{\max}$ is the kinematic maximum possible electron recoil kinetic energy, I is the mean excitation energy, δ includes the density-effect correction, $\Delta \frac{dE}{dx}$ stands for the high-energy corrections. Parameters describing ionization energy losses of muons in water that were used in PROPOSAL are reported in Table 3.4 [134]. The density effect correction is calculated using Sternheimer's parametrization [135]:

$$\delta = \begin{cases} 2(\ln 10)x - \overline{C} & \text{if } x \geq x_1, \\ 2(\ln 10)x - \overline{C} + a(x_1 - x)^k & \text{if } x_0 \leq x < x_1, \\ \delta_0 10^{2(x-x_0)} & \text{if } x < x_0, \end{cases} \tag{3.7}$$

where $x = \log_{10}(\beta\gamma)$, $\overline{C} = -C$ reported in Table 3.4.

Mass density	Mean excitation energy	Density correction constants					
ρ [g/cm^3]	I [eV]	a	m_s	x_0	x_1	C	δ_0
1.03975	75.0	0.09116	3.4773	0.2400	2.8004	-3.5017	0

Table 3.4: Parameters describing ionization energy losses of muons in the seawater.

3.4.2 Bremsstrahlung

During the propagation of a charged particle in a medium, it is scattered in the electric fields of atomic nuclei and electrons. Acceleration and deceleration of a particle lead to electromagnetic radiation which is called Bremsstrahlung.

Bremsstrahlung cross section for electrons was obtained by Bethe and Heitler [136]. In order to calculate the cross sections for muons, it is necessary to take into account nuclear screening which was first done consistently by Petrukhin and Shestakov [137]. More recent calculations done by Kelner et al. [129] were used as input for PROPOSAL in this work.

The differential cross section includes bremsstrahlung from a nucleus and electrons. For the nucleus, the cross section is expressed as follows:

$$\left.\frac{d\sigma}{d\nu}\right|_{\text{brems, nucl}} = \alpha(2Z\frac{m_e}{M_\mu}r_e)^2(\frac{4}{3}-\frac{4}{3}\nu+\nu^2)\frac{\Phi(\delta)}{\nu}. \tag{3.8}$$

Here ν is the fraction of the muon energy transferred to a photon, α is the fine structure constant, M_μ is the muon mass,

$$\Phi(\delta) = \ln(\frac{BM_\mu Z^{-1/3}/m_e}{1+\delta\sqrt{e}BZ^{-1/3}/m_e}) - \Delta_n(\delta), \tag{3.9}$$

where $B = 182.7$ ($B = 202.4$ for hydrogen), e is Euler's number, $\delta = M_\mu^2\nu/2E(1-\nu)$, and $\Delta_n(\delta)$ is the nuclear screening correction factor:

$$\Delta_n(\delta) = \ln(\frac{D_n}{1+\delta(D_n\sqrt{e}-2)/M_\mu}), \text{where } D_n = 1.54A^{0.27}. \tag{3.10}$$

The cross section for the bremsstrahlung from electrons is given by:

$$\left.\frac{d\sigma}{d\nu}\right|_{\text{brems, elec}} = \alpha Z(2\frac{m_e}{M_\mu}r_e)^2(\frac{4}{3}-\frac{4}{3}\nu+\nu^2)\frac{\Phi_{\text{in}}(\delta)}{\nu}, \tag{3.11}$$

with

$$\Phi_{\text{in}}(\delta) = \ln(\frac{M_\mu/\delta}{M_\mu\delta/m_e^2+\sqrt{e}}) - \ln(1+\frac{m_e}{\delta BZ^{-2/3}\sqrt{e}}), \tag{3.12}$$

where $B = 1429$ ($B = 446$ for hydrogen), and $\delta = M_\mu^2\nu/2E(1-\nu)$, as above.

3.4.3 Pair production

High-energy muons in the electric field of a nucleus produce virtual photons that lead to the production of electron-positron pairs. This process has an energy threshold since the photon energy must be greater than two electron masses. The differential cross section of the pair production was obtained by Kokoulin and Petrukhin and it is widely used in muon transport calculations. The full expression for the cross section can be found in [130].

3.4.4 Photonuclear interactions

Photonuclear interactions emerge due to the muon interaction with nuclei via the exchange of a virtual photon. The cross section that was used in PROPOSAL for this process was taken from the Abramowicz and Levy work [131].

3.4.5 LPM effect

Due to the low longitudinal momentum transfer between the nucleus and the fast particle, bremsstrahlung is not instantaneous but occurs over a finite formation zone [138]. During this time, external influences can perturb the fast particle and suppress the photon emission. It affects first the radiation of soft photons and is, therefore, most important for the bremsstrahlung energy loss. Hence, the standard Bethe and Heitler formula for the cross section no longer holds and has to be modified. Initially, Landau and Pomeranchuk studied the suppression effect by multiple scattering using a semiclassical argument [132]. Later, Migdal presented a full quantum treatment [139]. The calculation for the standard rock shows that the effect becomes noticeable at muon energy of 10 PeV and leads to a 10% decrease of the bremsstrahlung cross section at 10^3 PeV [140]. Therefore, this effect is of a less importance for the KM3NeT atmospheric muon simulations.

3.4.6 Water composition

The relative content of the seawater components is listed in Table 3.5. This is a standard water composition that is used in the KM3NeT simulations. The composition was taken from [141] corrected for the salinity at the ANTARES site [142]. The ANTARES location was nearby to the ORCA detector, the salinity at the ARCA site differs from the ANTARES one at a level below 1% [143, 144]. In the recalculations to correct for salinity, the content of all the elements except for hydrogen and oxygen was multiplied by a factor corresponding to the relative difference in salinity. However, the sea salt sulfate was neglected. Hence, also the relative content of oxygen should be recalculated properly. In this thesis work, the recalculation was performed using a more recent seawater composition [145]. The resulting chemical composition is presented in Table 3.6.

H	O	Na	K	Mg	Ca	Cl	S
2.0	1.00884	0.00943	0.000209	0.001087	0.000209	0.01106	0.00582

Table 3.5: Relative content of the seawater elements used in PROPOSAL. The content of hydrogen atoms is predefined to be equal to 2, the content of other elements is calculated relative to hydrogen.

H	O	Na	K	Mg	Ca	Cl	S
2.0	1.0024	0.00962	0.000209	0.001083	0.000211	0.01119	0.000579

Table 3.6: Recalculated content of the seawater elements. The recalculation was performed with the more recent seawater composition [145]. Also, it properly treats oxygen content enlargement due to the presence of sulfate in the seawater.

A test was performed in order to evaluate the influence of the new water composition on the simulation results. Also, it was noticed that a more recent value of the water mean excitation energy exists, $I = 79.7$ eV [134], instead of $I = 75.0$ eV as mentioned above. Hence, this value was also changed for the test.

Muons with initial energies from 1 TeV up to 10 TeV with a step of 500 GeV were propagated down to 2 km depth in water. The propagation was done with PROPOSAL using two different compositions mentioned above. The energy losses of muons were compared in two cases, the

results are presented in Fig. 3.9 left. The plot shows the ratio of the average energy losses of muons in the seawater with the new chemical composition and the mean excitation energy with respect to the standard KM3NeT water, vertical error bars represent the statistical errors. The same test was repeated for 3 km water depth, Fig. 3.9 right. The difference in both cases was found to be below 0.5%, so the original simulation results can be used.

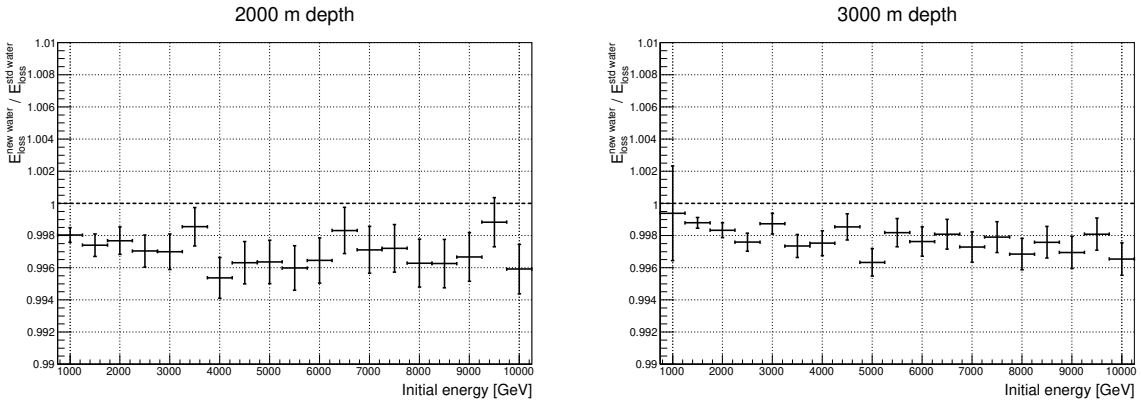

Figure 3.9: Impact of the seawater composition difference on the mean energy losses of muons traveling 2000 m (left figure) and 3000 m (right figure) as a function of initial energy. The relative differences induced by the new composition are below 0.5% in both cases.

3.5 Light generation

The light generation step of the simulation chain includes the particle propagation inside the can and the simulation of the Cherenkov light reaching the PMTs. There are two main programs used in the KM3NeT experiment for these simulations. The first one is called KM3Sim and it uses the GEANT4 package [146] for particle propagation. The simulation with GEANT4 is precise but also highly CPU-time consuming since it includes various energy loss processes and tracks all the particles. An alternative internal KM3NeT software is JSirene, which uses tabulated values of the probability density function (PDF) of the arrival time of light and the interpolation methods [147]. The light from a muon includes that of a minimum ionizing particle, δ-rays, and Bremsstrahlung showers. In this work, the JSirene simulation tool was used for light generation. The output of the light generation step is the information on the hit times of Cherenkov photons on the PMT photocathodes.

Simulation of light depends on the water properties. In particular, it depends on the light absorption and scattering lengths that are discussed below.

The light absorption length has been measured by the NEMO Collaboration at the "KM4" site [148]. The measurements were performed for attenuation and absorption, independently, using two different light paths and spanning the light spectrum over nine different wavelengths (412, 440, 488, 510, 532, 555, 650, 676, and 715 nm). The "KM4" site is 80 km offshore Capo Passero (36°2'N, 16°00'E) which is nearby to the ARCA location, the length at the ORCA site was assumed to be the same. The measurements were performed also in 5 different periods and about ±10% variation is seen in the absorption length distribution at 400-500 nm [148]. This is taken into account for the final data/MC comparison performed in this work, Chapter 5. The points below the NEMO results in Fig. 3.10 (below 412 nm) are coming from the ANTARES test device with 3-inch PMT [149] and from the Smith & Baker work [150]. Points at 290 nm

and 720 nm were added artificially. The average absorption length of photons with a wavelength of 440 nm is around 67 m.

The model used in the simulations for the light scattering description is the so-called ANTARES water model (which is also known as partic-0.0075). It includes two components: Rayleigh scattering which is the elastic scattering of light by particles that are typically much smaller than the wavelength of the light [151] and the scattering on large particles such as dust. The latter is described by Mie's solution of the Maxwell equations [152].

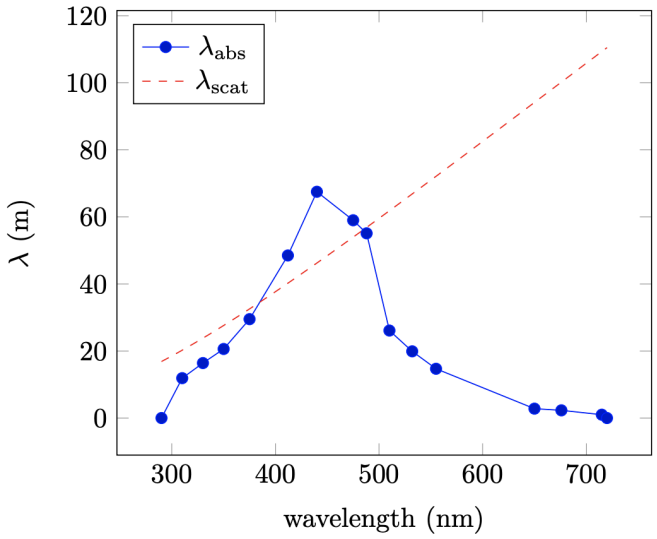

Figure 3.10: Light absorption (blue points) and scattering (red dashed line) lengths in seawater as a function of the photon wavelength. The figure is taken from the KM3NeT internal document.

3.6 Detector response simulation

The next step of the simulation chain is to model the detector response including the environmental optical background. The background includes the contribution from β-decays of ^{40}K, bioluminescent light [153], and other radioactive decays of nuclei in the DOM glass and water. For the simulation of response to the incoming photons, the characteristics of PMTs and the effects of front-end electronics are taken into account. The trigger-level simulation is usually performed in a so-called run-by-run approach, i.e. the simulation is subdivided into batches corresponding to the actual data-taking periods in order to reproduce the time variability of the detector conditions. In particular, the position and orientation of PMTs and values of PMT quantum efficiencies are considered individually for each run in the simulation. The background event rates are also extracted from the data.

3.7 Reconstruction

In a broad sense, the reconstruction is a fit of a model to the data. The same reconstruction algorithms are applied to both, the real data and the MC simulations. Neutrino interacting with matter produce two different event topologies. In this work, the track-like event reconstruction

arising from the secondary muon tracks is described in more details since this algorithm is used to reconstruct the atmospheric muons. A description of the shower-like event reconstruction can be found in [154].

3.7.1 Track reconstruction

The track reconstruction is performed in five consequent steps, the so-called reconstruction chain, that allows to estimate the direction and the energy of the muon tracks. The chain was developed within the Jpp software framework [155] widely used in the KM3NeT experiment for different purposes. The first three steps of the chain aim to reconstruct the position and direction of the track and the last two estimate the track length and energy. Names of the steps are given in the scheme below.

$$\text{JMuonPrefit} \rightarrow \text{JMuonSimplex} \rightarrow \text{JMuonGandalf} \rightarrow \text{JMuonStart} \rightarrow \text{JMuonEnergy}$$

JMuonPrefit

The muon trajectory is described by its direction and position at each point in time, resulting in 5 independent parameters. The main difficulty in trajectory reconstruction is the non-linearity of the problem. In order to reduce the problem to the linear one, different track directions are assumed and the remaining unknown parameters are, thus, the position of the muon at a given time.

JMuonPrefit performs an initial fit by considering N track direction hypotheses covering the whole solid angle of the sky with a predefined step. This process assumes a direction and fits the position of the muon and the time at which it crosses a reference plane perpendicular to the muon direction. The iterative procedure aims to minimize the χ^2 which is calculated based on the time difference between the expected arrival time of a photon and its actual arrival time and is normalized to an assumed time resolution. A specified number of the best fits, usually 40, is saved by JMuonPrefit and then passed on to JMuonSimplex for the next step of the muon trajectory reconstruction.

JMuonSimplex

An intermediate fit of the muon trajectory is performed with JMuonSimplex. It uses the best-fit solutions from JMuonPrefit and performs the further minimization of the photon arrival time residuals via an algorithm called Powell's method [156].

JMuonGandalf

JMuonGandalf is the main part of the muon trajectory reconstruction. It takes the fits from JMuonSimplex, performs a scan around the corresponding track hypothesis, and minimizes a chi-square function in terms of the track direction and position. The method of chi-square estimation relies on the semi-analytical arrival time distributions. These distributions describe the number of photo-electrons detected by PMT taking into account its position and orientation with respect to the muon track. Various factors are considered when determining the arrival time distributions, such as the PMT's quantum efficiencies, transit-time spreads, and angular acceptances. The distributions take into account the light produced by different sources, including direct and single scattered Cherenkov light, emission from electromagnetic and hadronic

showers, the light produced by delta-rays created along the track, and the light due to the energy loss of a muon. For the transmission of light, the wavelength-dependent effects of dispersion, absorption, and scattering in the medium are considered. The angular acceptance and the quantum efficiency of the PMTs are also taken into account. The arrival time distributions are used to define the PDFs which determine the chance to observe a first photo-electron at a relative time with respect to the arrival time expectation for a direct hit caused by an unscattered Cherenkov photon. Fig. 3.11 shows the PDF distributions obtained for 1 TeV muon passing the PMT at a distance of closest approach of 50 m for different relative orientations of the PMTs.

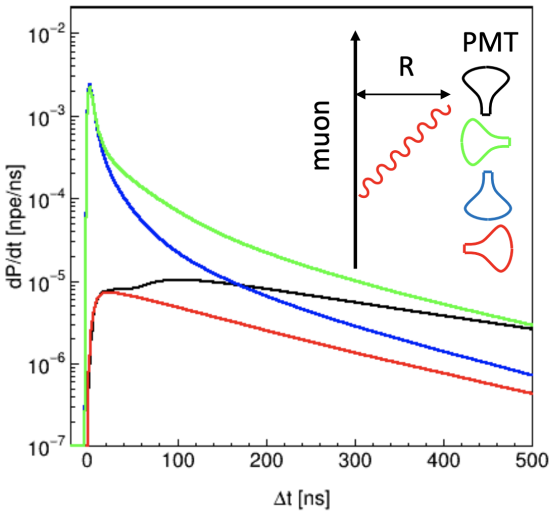

Figure 3.11: The PDFs obtained for a 1 TeV muon track located at 50 m from the PMT for different relative orientations.

Using the PDFs described above, the likelihood functions under two hypotheses are defined. The H_1 hypothesis implies that a track particle is responsible for a given cluster of hits within the detector, while the H_0 hypothesis assumes that the hit pattern was caused by background radiation only. The natural logarithm of a ratio of two likelihood functions asymptotically follows a chi-square distribution according to Wilks' theorem [157]. JMuonGandalf finds a minimum of this function that corresponds to the track which is most compatible with the signal hypothesis and least with the background-only model. The final chi-square value corresponding to the obtained minimum is saved and is used to define the quality metric, $Q = -\chi^2$, of the fit.

JMuonStart

JMuonStart uses back-projection of hits onto the track under the Cherenkov angle to determine the starting position of the muon trajectory. The first associated emission point which exceeds the random background level is selected as the start position.

JMuonEnergy

JMuonEnergy evaluates the muon energy. The evaluation is based on the minimization of a likelihood function in terms of the track energy. The function consists of a sum over the logarithm of the hit and no-hit probabilities in a cylinder surrounding the muon track. For each PMT in the cylinder, the number of photon hits induced by the background from ^{40}K decays,

by delta-rays, by electromagnetic showers, and by the ionization and radiative energy losses of the muon are estimated from the tabulated PDFs. The probability that the i-th PMT observes n hits is given by the Poisson distribution,

$$P(n;\mu_i(E)) = \frac{\mu_i(E)^n}{n!}e^{-\mu_i(E)}, \tag{3.13}$$

where μ_i is an expected number of hits on the i-th PMT as a function of the muon energy, E. Therefore, the probability that there are no hits observed is

$$P(n=0;\mu_i(E)) = e^{-\mu_i(E)}, \tag{3.14}$$

and the probability to have at least one hit on the i-th PMT is

$$P(n>0;\mu_i(E)) = 1 - P(n=0;\mu_i(E)) = 1 - e^{-\mu_i(E)}. \tag{3.15}$$

The likelihood as a function of the energy, $L(E)$, is minimized using an M-estimation method. The likelihood is defined differently for energy reconstruction in ORCA and ARCA. In ORCA, the null M-estimator is used and $L(E)$ is defined as

$$L_{\text{ORCA}}(E) = -\sum_{i=1}^{N} \ln[(1-2e^{-\mu_i(E)})\mathbf{I}_{n>0} + e^{-\mu_i(E)}]. \tag{3.16}$$

Here N is the total number of PMTs inside the cylinder, $\mathbf{I}_{n>0}$ equals 1 if $n>0$ and equals 0 otherwise.

For ARCA, it was shown that the energy evaluation algorithm performs better using a sum over Lorentzian functions, $\rho(x) = 1 + \frac{1}{2}x^2$, to determine the likelihood:

$$L_{\text{ARCA}}(E) = \sum_{i=1}^{N} \Big[1 + \frac{1}{2}\ln^2[(1-2e^{-\mu_i(E)})\mathbf{I}_{n>0} + e^{-\mu_i(E)}]\Big]. \tag{3.17}$$

3.7.2 Reconstruction performance

The capabilities to reconstruct the muon properties are discussed in Chapter 5. Here, the neutrino reconstruction performance is considered. Fig. 3.12 demonstrates the median angular resolution of the ORCA detector with 115 lines as a function of neutrino energy. Four different classes of events are considered, the charged current (CC) interactions of electron and muon neutrino and the corresponding anti-neutrino. The resolution is better than 15 degrees for neutrino energies above 5 GeV. The energy resolution of the ORCA detector in its full configuration is shown in Fig. 3.13. The left plot on the figure shows the true vs reconstructed energy distribution for the track-like events from the muon neutrino CC interactions, the right plot on the same figure was obtained for the shower-like events resulting from the electron neutrino CC interactions. The energy resolution is Gaussian-like with $\Delta E/E \approx 25\%$ for the shower-like events. The energy resolution for the track-like events is lower, $\Delta E/E \approx 35\%$, since muon tracks are not always fully contained inside the instrumented volume. The red diagonal line indicates perfect energy reconstruction.

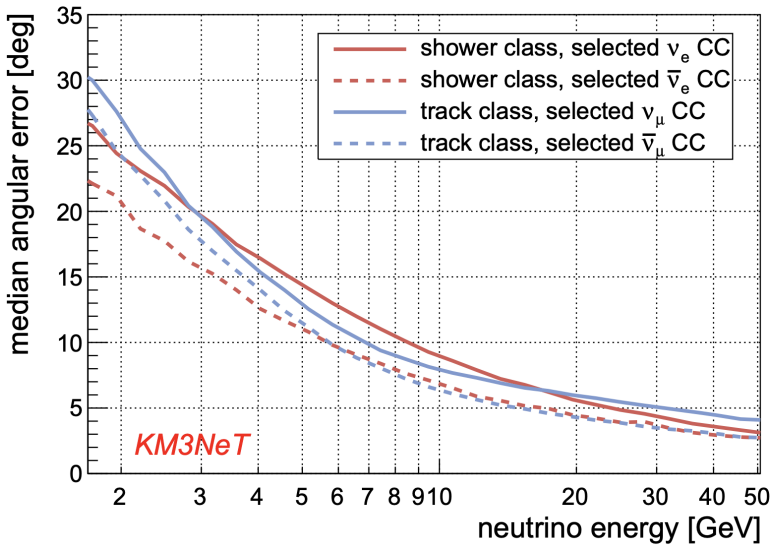

Figure 3.12: Angular resolution for the CC muon (blue) and electron (red) events reconstructed with ORCA115. The figure is taken from [93]

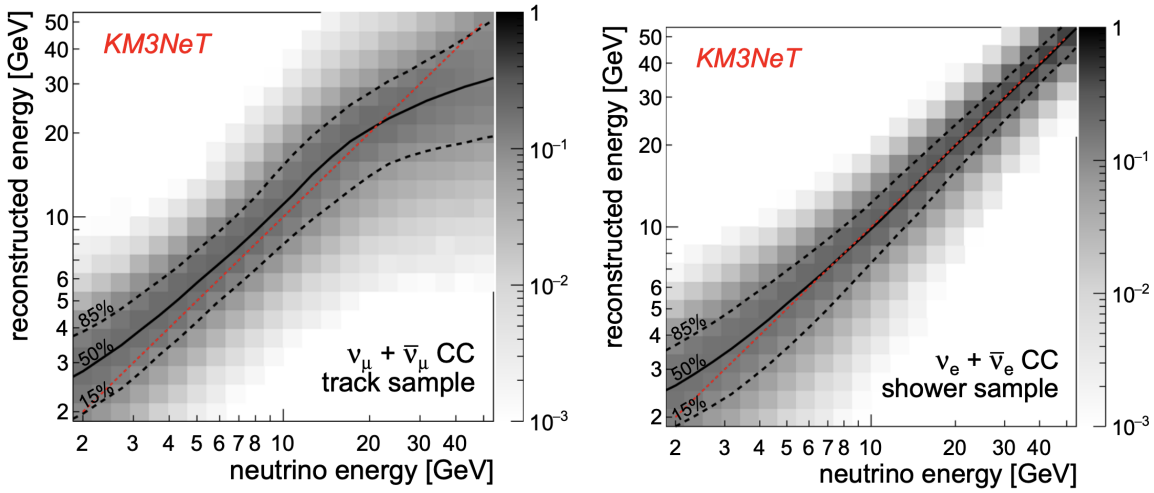

Figure 3.13: Energy resolution obtained for the ORCA115 detector for the track-like (left plot) and shower-like (right plot) events as a function of neutrino energy. The figure is taken from [93]

The reconstruction performance for the angular resolution of the ARCA detector in its full configuration is shown in Fig. 3.14. The red line on the left plot demonstrates the angular resolution as a function of neutrino energy for the track-like events, the resolution is below 1° for neutrino energy above 1 TeV. The green line is the average angle between the parent neutrino and secondary muon. The shaded areas correspond to 1 σ deviation from the average values. The black dashed line is the IceCube performance [158] shown for comparison. The ARCA angular resolution for the shower events is shown on the right part of Fig. 3.14. The AAshower fit is the standard KM3NeT reconstruction algorithm while the timing information algorithm is the improved one [159]. The energy reconstruction performance for the track (shower) events is

shown on the left (right) of Fig. 3.15. The energy resolution obtained for the track-like events is 0.27 units in $\log_{10}(E_\mu)$ for 10 TeV $\leq E_\mu \leq$ 100 PeV. The shower-like events resolution for the energy reconstruction is around 10% for events above 70 TeV.

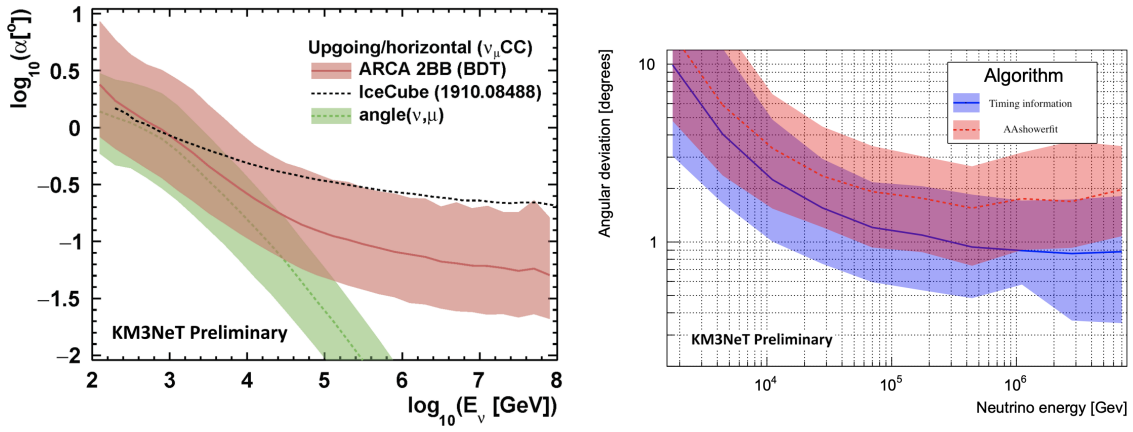

Figure 3.14: Angular resolution with the 2 full building blocks of ARCA for the tracks (left plot taken from [160]) and showers (right plot taken from [159]).

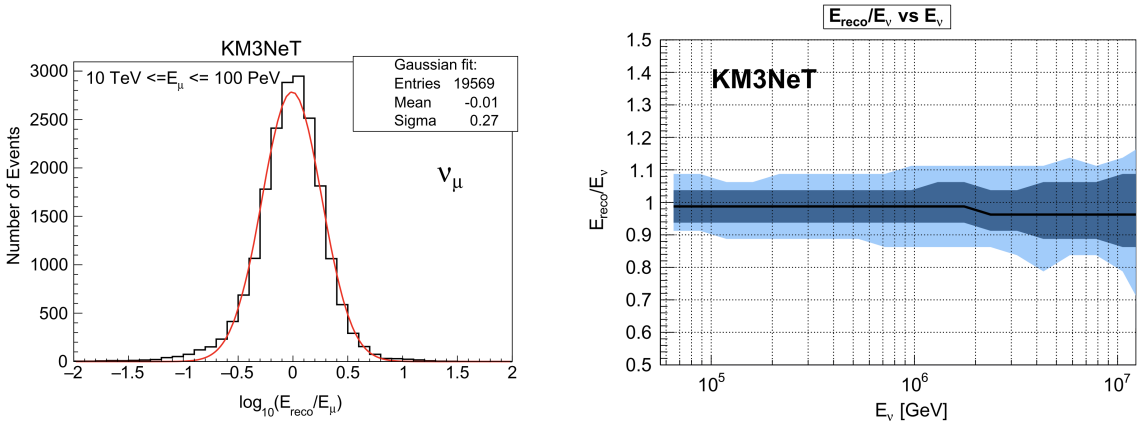

Figure 3.15: The energy reconstruction performance with the completed ARCA detector. The left plot presents the energy reconstruction of the tracks, the right one is for the showers. The figure is taken from [79].

3.8 Results of the atmospheric muon simulations

The top (bottom) plot in Fig. 3.16 demonstrates the rate of events reconstructed with the ORCA6 (ARCA6) detector as a function of the primary energy. The highlighted area indicates the 90% fraction of the total number of events counting from the maximum of the distribution. The corresponding energy range spans from 3 to 350 TeV for ORCA6 and from 4 TeV to 1 PeV for ARCA6. The same plot but for the full ORCA (ARCA) detector configuration is presented on top (bottom) of Fig. 3.17. The energy ranges for the completed detectors are $3 - 250$ TeV for ORCA115 and 6 TeV $-$ 1 PeV for ARCA115.

As it can be seen from the figures below, most of the events detected by the KM3NeT telescopes originate from proton and helium nuclei. Detailed comparisons of the simulation result with the real data are presented in Chapter 5.

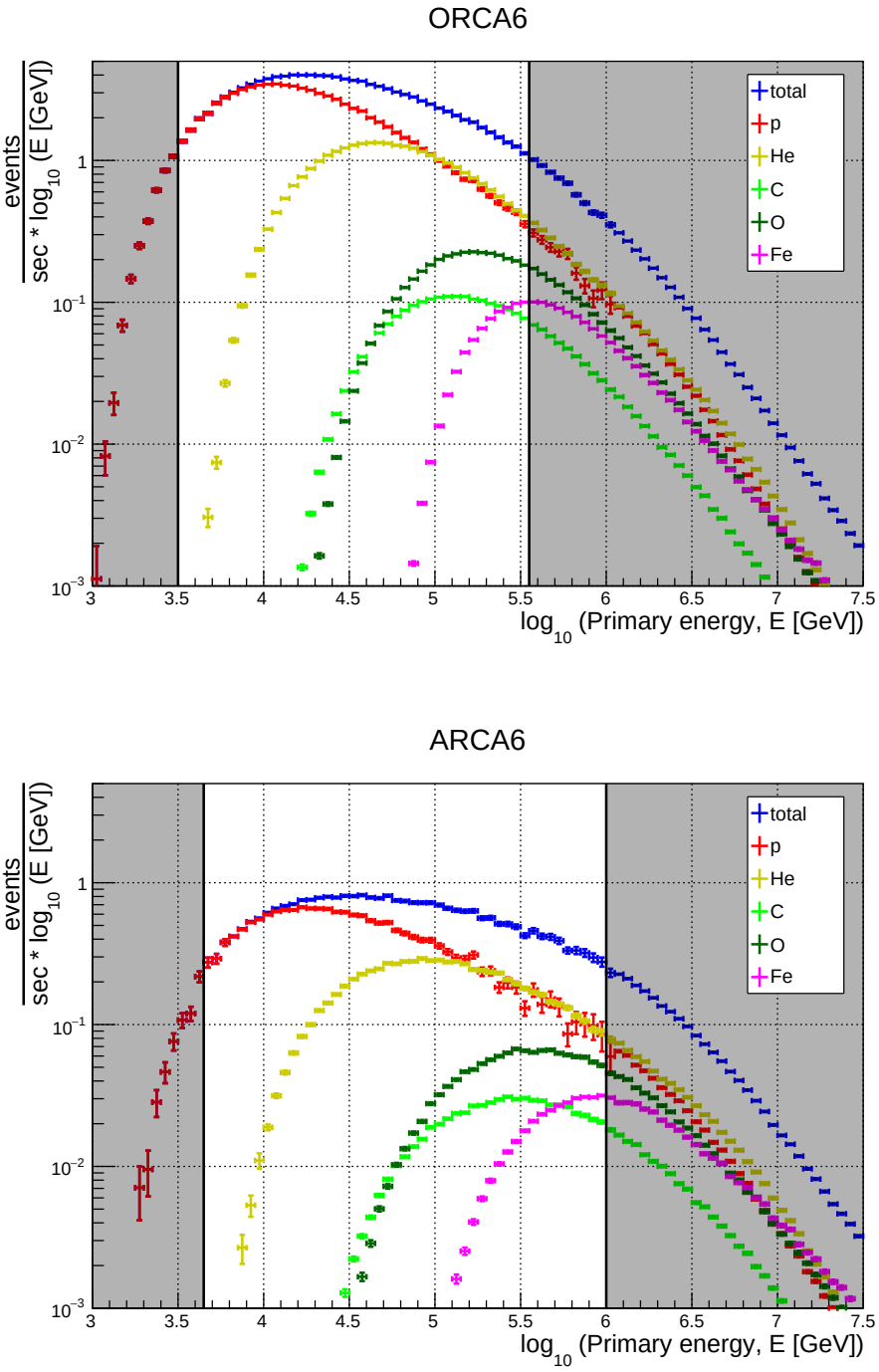

Figure 3.16: Event rate of the atmospheric muon events reconstructed with the ORCA6 (top plot) and ARCA6 (bottom plot) detectors as a function of the primary CR energy. The highlighted area corresponds to the 90% fraction of events.

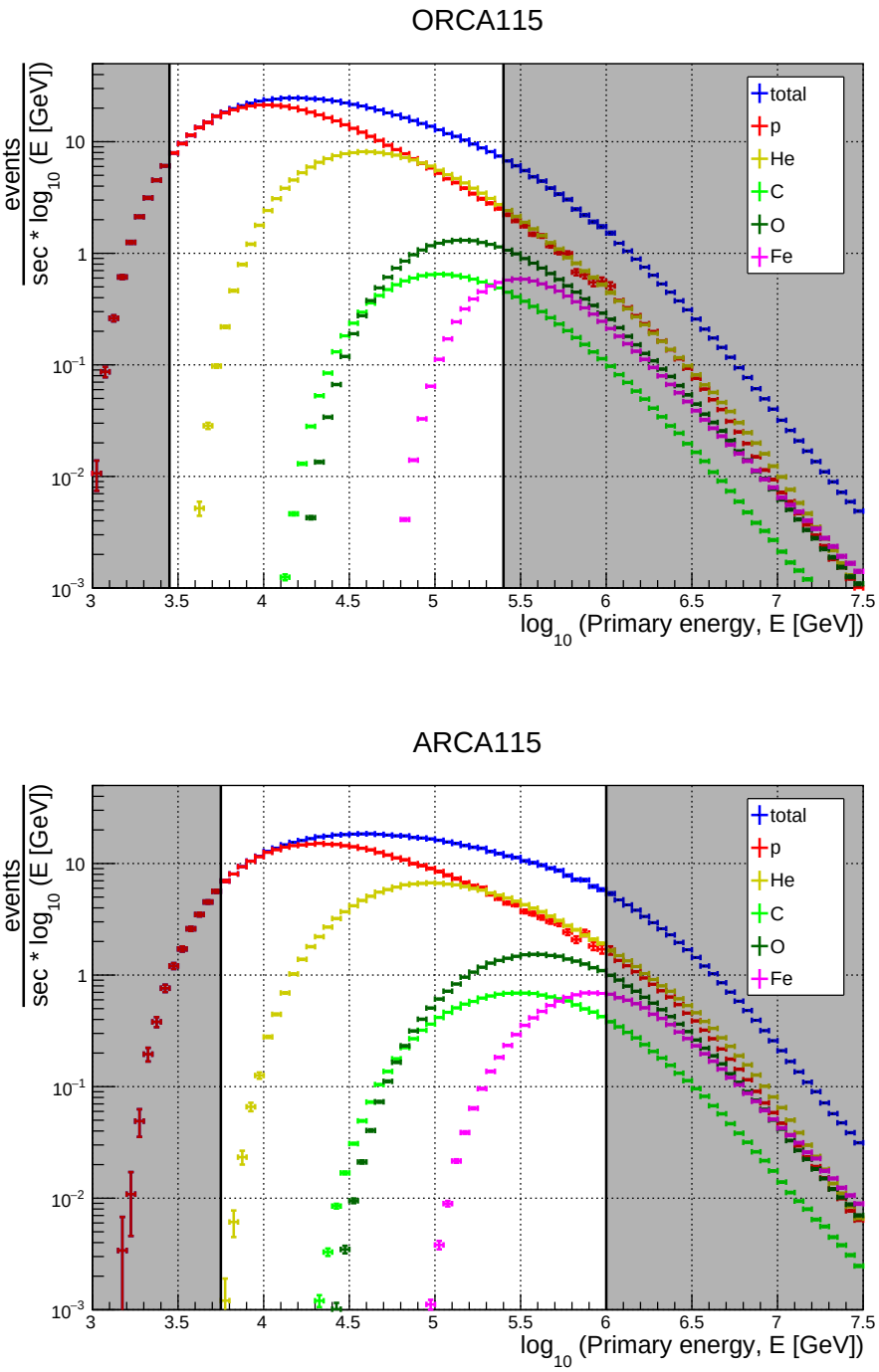

Figure 3.17: Atmospheric muon rates reconstructed with the ORCA (top plot) and ARCA (bottom plot) detectors in their completed configurations.

4 Tuning of the MUPAGE parameters on the CORSIKA simulation

This chapter describes the framework that the author of this work developed for the MUPAGE [161] parameters tuning on the CORSIKA full MC simulation [66].

4.1 Motivation

CORSIKA provides the full simulations of EAS as described in Chapter 3. However, the main drawback of using the full simulation is that it is highly CPU time-consuming. The KM3NeT telescopes are currently under construction and the new detector configurations arise every sea campaign. Hence, the simulations must be redone for every new detector layout. Moreover, the software is being modified and improved continuously which in its turn requires new simulations to be performed for every new software release. Finally, the KM3NeT simulations are based on the so-called Run-by-Run (RbR) approach, i.e. the simulations are subdivided into batches corresponding to the actual data-taking periods in order to reproduce the time variability of the detector conditions. In particular, the calibrated position and orientation of PMTs and values of PMT quantum efficiencies are considered individually for each run in the simulation. The RbR simulations are not possible with CORSIKA due to the large CPU time needed for the full MC simulations.

To fulfill these requirements, the KM3NeT simulation of atmospheric muons is based on the fast MC generator originally developed for the ANTARES neutrino telescope [90], MUPAGE (Atmospheric MUons from PArametric formulas: a fast GEnerator for neutrino telescopes) [161]. MUPAGE generates the muon bundle properties for a certain sea depth and zenith angle based on parametric formulas. The formulas describe the flux of the single and multiple muons in the bundles, the differential energy spectrum, and the distance of muons from the bundle axis. Values of the parameters were initially obtained by fitting the muon distributions at different depths resulting from the HEMAS full MC simulation [162]. In this work, a framework was developed in order to tune the MUPAGE parameters using the CORSIKA simulation software and the most recent models available that describe the high-energy hadronic interactions, Sibyll 2.3d [69], and CR flux, GSF [19].

4.2 Muon propagation in water

The CORSIKA simulation code was used to obtain muon distributions at the sea level originating from CR showers. As it was described in the Chapter 3, there is a dedicated internal KM3NeT software for the muon propagation in water, gSeaGen [126]. However, it is only possible to propagate muons down to the detector cans with gSeaGen, while the MUPAGE parametrization is obtained by fitting the muon distribution at the plane perpendicular to the EAS axis. To take into account these differences, the CaP (CORSIKA and PROPOSAL) code

was developed in this work. The CaP results helped to resolve the issues that were present in the standard KM3NeT software for the atmospheric muon simulations.

4.2.1 The CaP code

The CaP software reads CORSIKA binary output files, propagates muons down in seawater using PROPOSAL v6 [127], and saves the output in the standard KM3NeT data format. This subsection describes the propagation geometry used in CaP.

The shower axis intersects the sea-surface at (0, 0, 0) point in the CORSIKA coordinate system, muons are located around the shower axis at the surface which is tangential to the Earth's curvature, Fig. 4.1.

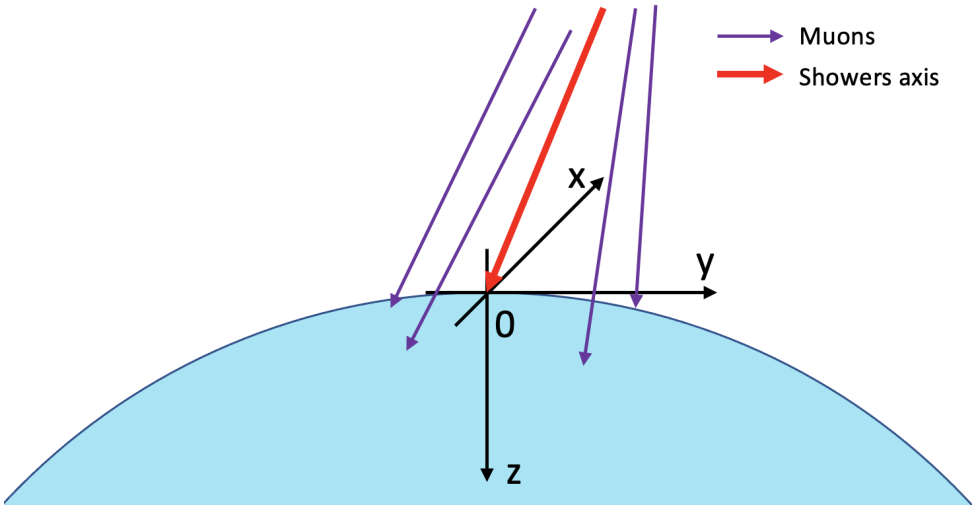

Figure 4.1: Sketch of the CORSIKA coordinate system. The shower axis is shown as a red arrow, the atmospheric muons are purple arrows.

The origin of the CaP coordinate system is the Earth center and the z-axis points to the sea surface, opposite to the CORSIKA z-axis. The goal is to rotate each shower so that the shower axis intersects the CaP z-axis at $(0, 0, R-d)$ point, the green circle in Fig. 4.2. Here $R = 6371.3$ km is the Earth radius and d is the propagation depth. The first step of the rotation is to find an intersection point between the original shower axis and a sphere with a radius of $R - d$, the red circle in Fig. 4.2.

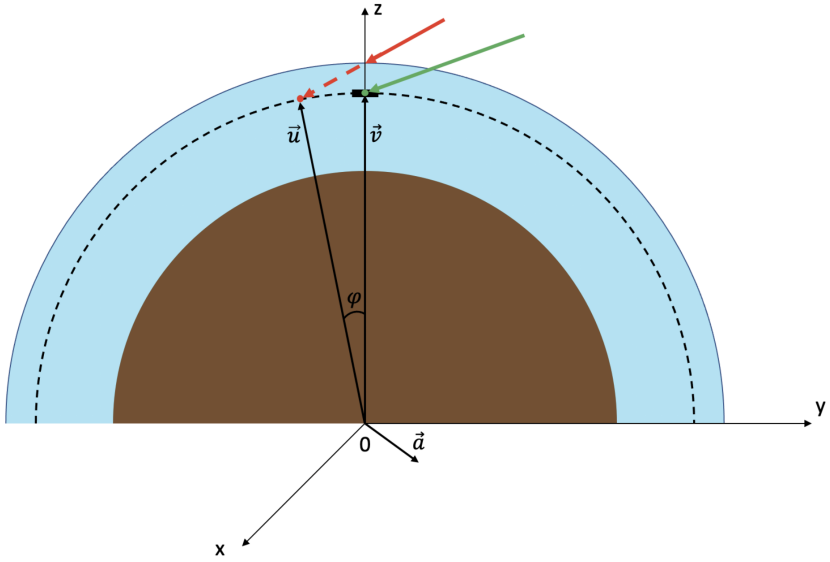

Figure 4.2: The shower rotation geometry used in CaP. The red arrow is the shower direction from the CORSIKA simulations and the green arrow is the rotated shower.

The equation that describes the sphere with a radius of $R - d$ is

$$x^2 + y^2 + z^2 = (R - d)^2. \tag{4.1}$$

The shower axis line is

$$\begin{cases} x = \alpha_x t, \\ y = \alpha_y t, \\ z = R + \alpha_z t, \end{cases} \tag{4.2}$$

where α_x, α_y, and α_z are direction cosines of a primary and t is a parameter. Hence, in order to find the intersection point, x, y and z coordinates in Eq. 4.1 must be replaced with the corresponding coordinates from Eq. 4.2:

$$\begin{gathered} (\alpha_x t)^2 + (\alpha_y t)^2 + (R + \alpha_z t)^2 = (R - d)^2 \Rightarrow \\ \begin{cases} t_1 = -R\alpha_z - \sqrt{(R\alpha_z)^2 - [R^2 - (R - d)^2]} \\ t_2 = -R\alpha_z + \sqrt{(R\alpha_z)^2 - [R^2 - (R - d)^2]} \end{cases} \end{gathered} \tag{4.3}$$

The smaller value of the two solutions is t_1 because α_z is always negative since the EAS are downward-going. The t_1 value is chosen for the further calculations since an intersection point closer to (0, 0, $R - d$) is needed. Therefore, the coordinates of $\vec{u}$ and $\vec{v}$ in Fig. 4.2 are known, $\vec{u} = (\alpha_x t_1, \alpha_y t_1, R + \alpha_z t_1)$ and $\vec{v} = (0, 0, R - d)$.

Hence, sine and cosine of an angle between $\vec{u}$ and $\vec{v}$, the rotation angle φ, can be calculated as

$$\begin{aligned} \cos\varphi &= \frac{\vec{u}\cdot\vec{v}}{||\vec{u}||\cdot||\vec{v}||} \\ \sin\varphi &= \frac{||\vec{u}\times\vec{v}||}{||\vec{u}||\cdot||\vec{v}||}. \end{aligned} \tag{4.4}$$

The rotation axis is determined as a cross product of $\vec{u}$ and $\vec{v}$,

$$\vec{a} = \frac{\vec{u}\times\vec{v}}{||\vec{u}\times\vec{v}||}. \tag{4.5}$$

Matrix for rotation around the vector $\vec{a}$ by the angle φ is given by the Rodrigues' rotation formula [163]:

$$R = \begin{bmatrix} \cos\varphi + a_x^2(1-\cos\phi) & a_x a_y(1-\cos\varphi) - a_z\sin\varphi & a_x a_z(1-\cos\varphi) + a_y\sin\varphi \\ a_y a_x(1-\cos\varphi) + a_z\sin\varphi & \cos\varphi + a_y^2(1-\cos\phi) & a_y a_z(1-\cos\varphi) - a_x\sin\varphi \\ a_z a_x(1-\cos\varphi) - a_y\sin\varphi & a_z a_y(1-\cos\varphi) + a_x\sin\varphi & \cos\varphi + a_z^2(1-\cos\phi) \end{bmatrix}$$

Starting positions and directions of primaries and muons are then recalculated using the R matrix. Hence, the shower is rotated so that it intersects the plane perpendicular to its direction at a given depth and all the muons are rotated accordingly.

4.2.2 Statistics of the muon simulation

Atmospheric muons were propagated down in water up to 7 depths, from 2000 to 3500 m with a step of 250 m. Fig. 4.3 shows the flux of muons at 3500 m depth as a function of the primary energy for the five different nuclei that were used in the CORSIKA simulations. As can be seen from the plot, the statistics are enough for the whole energy range and for every primary.

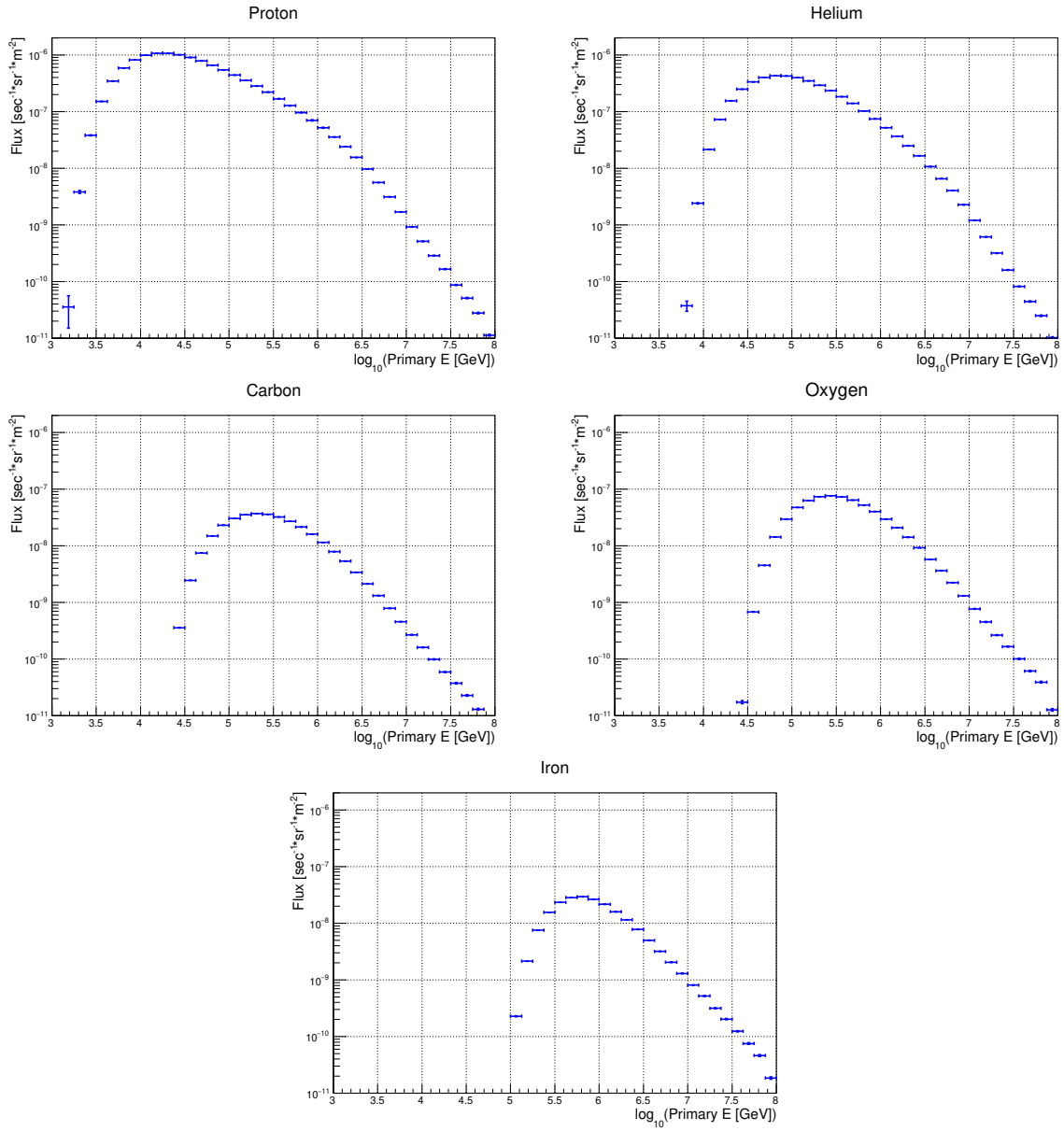

Figure 4.3: Flux of muons at 3500 m.w.e depth as a function of the primary energy for five nuclei used in the simulations.

4.3 The MUPAGE tuning

In order to obtain new values of the MUPAGE parameters, histograms of the muon properties, e.g. flux of single muons, were fitted with the corresponding MUPAGE function.

4.3.1 Flux of single muons

Underwater muon flux is parametrized in MUPAGE using the following function:

$$\Phi(m; h, \theta) = \frac{K(h, \theta)}{m^{\nu(h,\theta)}}. \tag{4.6}$$

Here m is the multiplicity (number of muons in the bundles), h is depth in km.w.e, θ is zenith angle, K and ν are free parameters.

As a first step, the flux of single muons ($m = 1$) as a function of the cosine of the zenith angle was fitted. In this case, Eq. 4.6 becomes:

$$\Phi(m = 1; h, \theta) = K(h, \theta) = K_0(h) \cos\theta \cdot \mathrm{e}^{K_1(h) \sec\theta}. \tag{4.7}$$

The fit was performed at seven values of vertical depth, from 2 km down to 3.5 km with a step of 0.25 km. The bin size of $\cos\theta$ was set to 0.025. An example of the fit at 2 km depth is shown in Fig. 4.4.

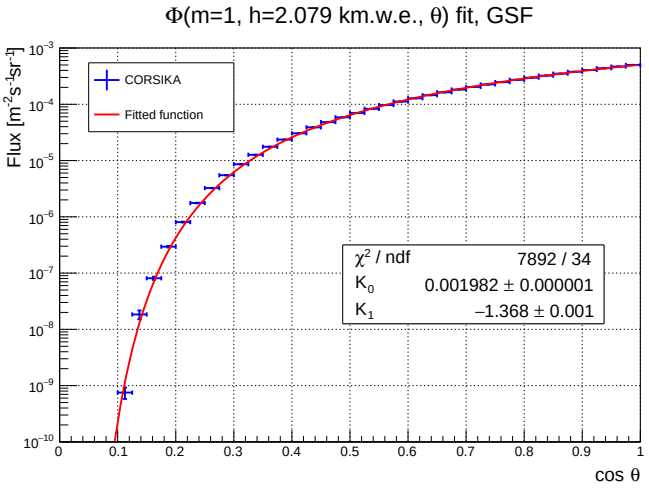

Figure 4.4: Single muon flux as a function of zenith angle at 2 km depth fitted with Eq. 4.7. Blue points represent the CORSIKA distribution, the red line is the MUPAGE fitting function.

Values of the parameters K_0 and K_1 depend on depth which is described by the following MUPAGE functions:

$$K_0(h) = K_{0a} \cdot h^{K_{0b}}, \tag{4.8}$$

$$K_1(h) = K_{1a} \cdot h + K_{1b}. \tag{4.9}$$

The $K_0(h)$ and $K_1(h)$ fit results are shown in Fig. 4.5. A list of the new K parameters compared with the nominal ones is reported in Table 4.1.

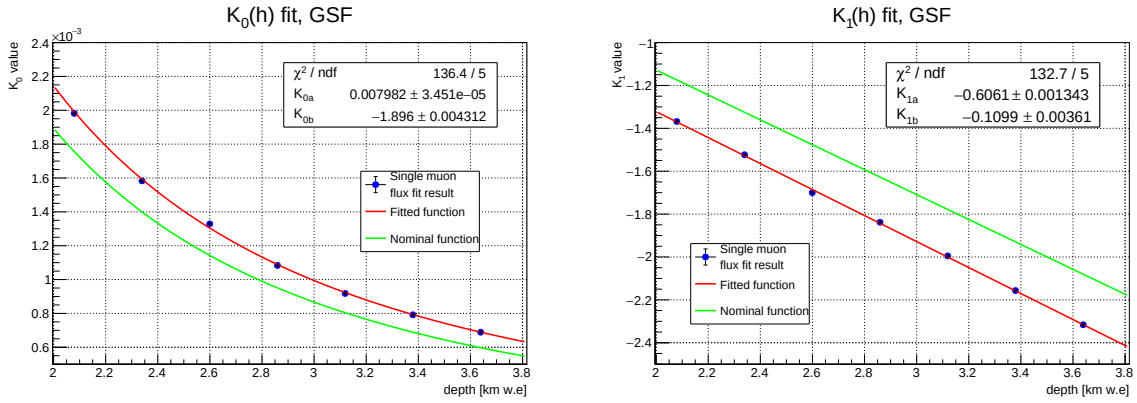

Figure 4.5: Left (right) plot shows the parameter K_0 (K_1) values as a function of depth fitted with Eq. 4.8 (Eq. 4.9). Blue points represent the parameter values obtained from the single muon flux fit at the 7 depths mentioned above. The red line is the MUPAGE function used for the fit, the green line is the same function but with the nominal MUPAGE parameters.

Name	Nominal Value	Fitted value
K_{0a}	7.20 $\times 10^{-3}$	7.98 $\times 10^{-3}$
K_{0b}	-1.927	-1.896
K_{1a}	-0.581	-0.606
K_{1b}	0.034	-0.110

Table 4.1: List of the nominal and fitted values of the parameters that describe the flux of single muons.

In order to check whether the new parametrization of single muon flux describes the corresponding CORSIKA distribution, a ratio between the MUPAGE function and the CORSIKA flux was obtained. Examples for 2 and 3.5 km depths are shown in Fig. 4.6. The MUPAGE results with the tuned parameters agree with the CORSIKA distributions, the largest discrepancy is for the very inclined muons.

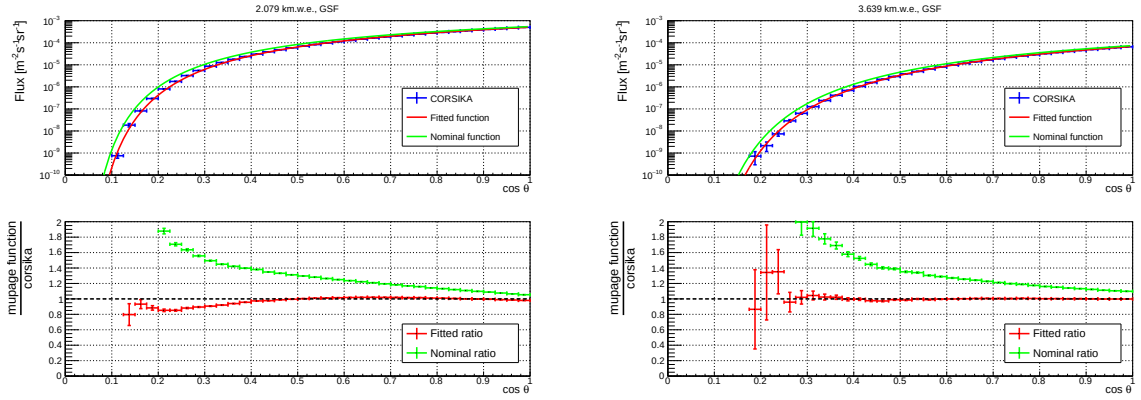

Figure 4.6: Ratios of the single muon zenith flux distribution from the CORSIKA simulation (blue points) with respect to the nominal (green line) and the fitted (red line) MUPAGE functions at 2 (left plot) and 3.5 km (right plot) depths.

4.3.2 Flux of multiple muons

In order to obtain new values of the parameters that describe the number of muons in the bundles, flux of muons as a function of multiplicity was fitted with Eq. 4.6, where K parameter was fixed to the value calculated with the new parametrization obtained in Sec. 4.3.1. Hence, the fitting function had only one free parameter, ν.

Multiplicity distributions were produced for several cosines of the zenith angle at each of the seven depths mentioned above. The same step in $\cos\theta$ space was used as for the single muon flux histograms, resulting in 40 histograms at each depth. The multiplicity fitting range was set from 2 up to 100 muons in the bundles. An example of the fit of vertical muon bundles ($0.975 \leq \cos\theta \leq 1.0$) at 2 km depth is presented in Fig. 4.7.

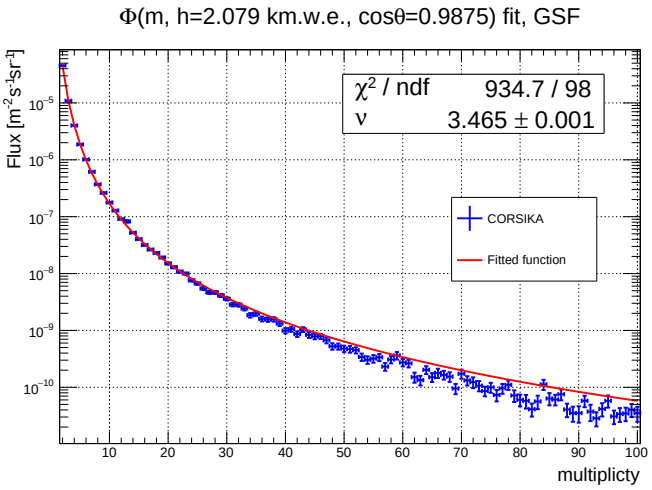

[H]

Figure 4.7: Flux of vertical muon bundles ($0.975 \leq \cos\theta \leq 1.0$) as a function of multiplicity at 2 km depth (blue points) fitted with Eq. 4.6 (red line).

At a given depth, MUPAGE parametrizes ν as a function of $\cos\theta$:

$$\nu(h;\theta) = \nu_0(h) \cdot \mathrm{e}^{\nu_1(h)/\cos(\theta)}. \tag{4.10}$$

Therefore, the fit of the parameter ν values as a function of $\cos\theta$ was performed at each depth. Fig. 4.8 illustrates the fit for 2 km depth. The fit result is the ν_0 and ν_1 values at each depth. Due to the lack of statistics for inclined muons with $\cos\theta < 0.2$, the fit range was restricted to $0.2 <= \cos\theta <= 1.0$ ($0.25 <= \cos\theta <= 1.0$ for 3.5 km depth).

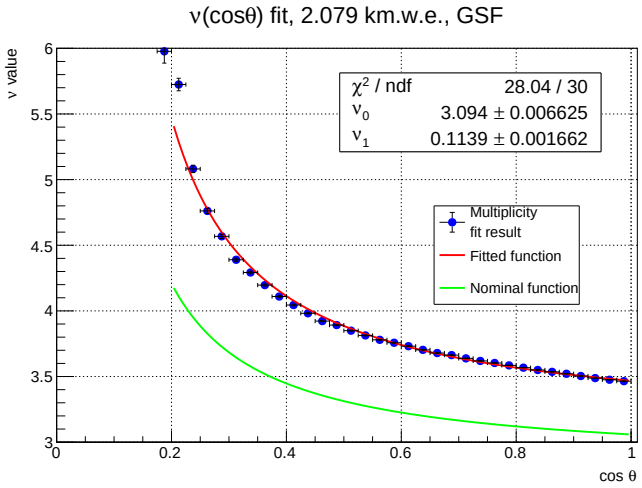

Figure 4.8: The parameter ν dependence on $\cos\theta$ at 2 km depth (blue points) fitted with Eq. 4.10 (red line).

The ν_0 and ν_1 depth dependence is parametrized as

$$\nu_0(h) = \nu_{0a} \cdot h^2 + \nu_{0b} \cdot h + \nu_{0c}, \tag{4.11}$$

$$\nu_1(h) = \nu_{1a} \cdot e^{\nu_{1b} h}. \tag{4.12}$$

The $\nu_0(h)$ and $\nu_1(h)$ fit results are shown in Fig. 4.9.

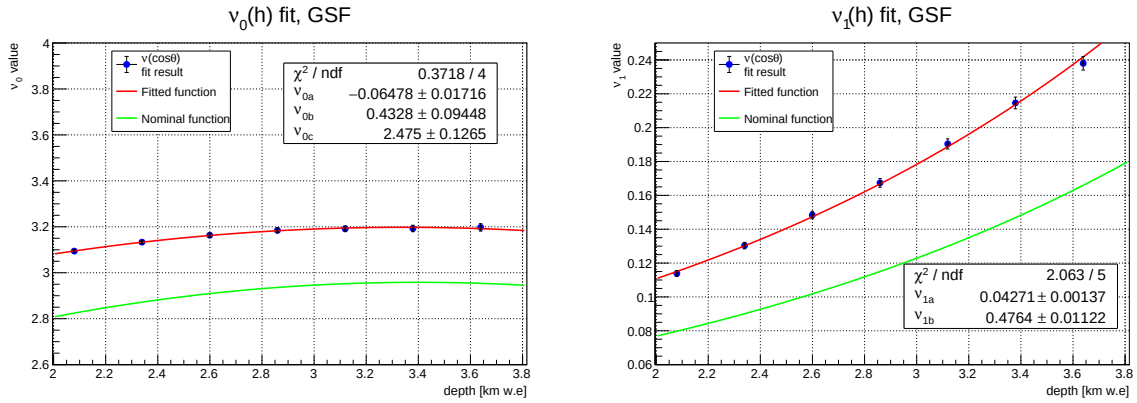

Figure 4.9: Left (right) plot demonstrates the parameter ν_0 (ν_1) values obtained from the $\nu(\theta)$ fit (blue points) fitted with Eq. 4.11 (Eq. 4.12). The fitted function is shown in red, the nominal MUPAGE function is in green.

The nominal and new values of MUPAGE parameters which describe the muon multiplicity are listed in Table 4.2.

Name	Nominal Value	Fitted value
ν_{0a}	-7.71 $\times$ 10^{-2}	-6.48 $\times$ 10^{-2}
ν_{0b}	0.524	0.433
ν_{0c}	2.068	2.475
ν_{1a}	0.030	0.043
ν_{1b}	0.470	0.476

Table 4.2: List of the nominal and fitted values of the multiplicity parameters.

Examples of a ratio of the MUPAGE function with the nominal and fitted parameter values with respect to the CORSIKA multiplicity distribution for the vertical muon bundles ($0.975 \leq \cos\theta \leq 1.0$) reaching 2 km and 3.5 km depths are plotted in Fig. 4.10. Ratios for inclined muon bundles with $0.5 \leq \cos\theta \leq 0.525$ are shown in Fig. 4.11. The MUPAGE functions with the new parameter values are in good agreement with the CORSIKA distributions. The nominal functions significantly overestimate the CORSIKA multiplicity distributions.

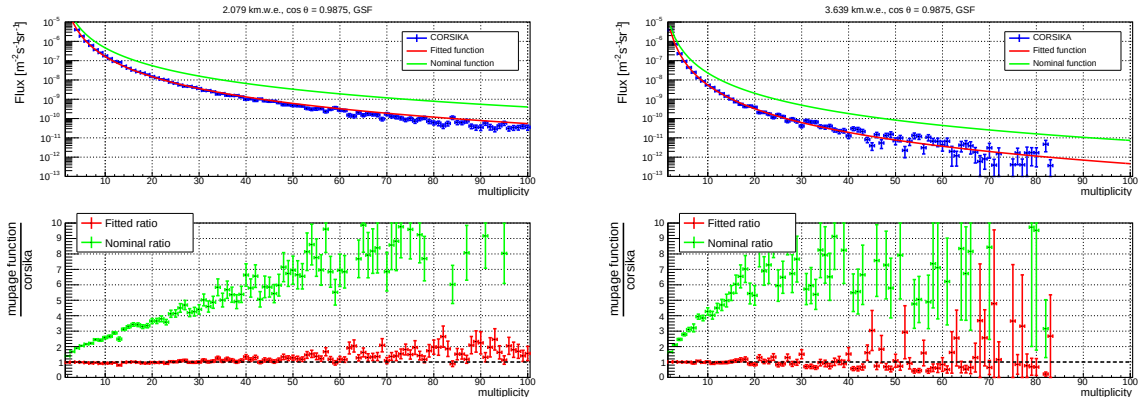

Figure 4.10: Ratio of the CORSIKA multiplicity distribution (blue points) for the vertical muon bundles ($0.975 \leq \cos\theta \leq 1.0$) at 2 km (left plot) and 3.5 km (right plot) depths with respect to the nominal (green line) and the fitted (red line) MUPAGE functions.

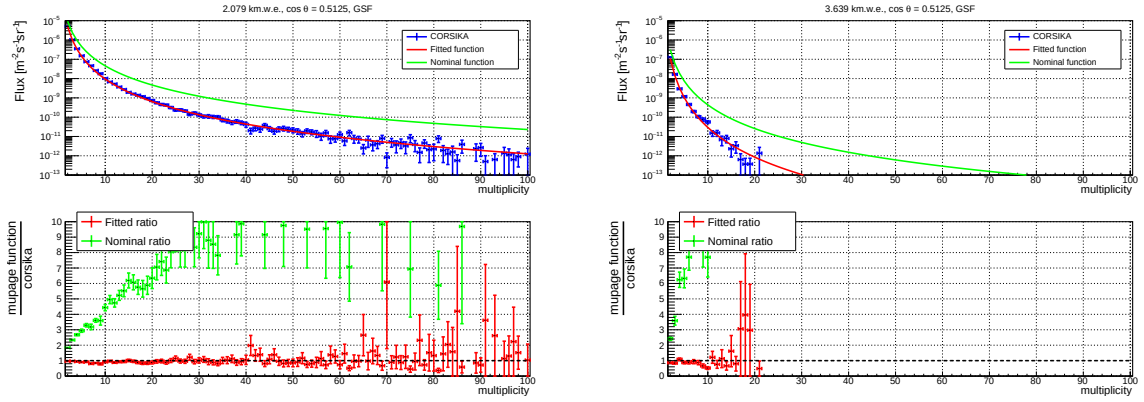

Figure 4.11: Multiplicity distributions of inclined muon bundles, $0.5 \leq \cos\theta \leq 0.525$, (blue poins) compared to the fitted (red line) and nominal (green line) MUPAGE functions at 2 km (left plot) and 3.5 km (right plot) depths.

4.3.3 Energy spectrum of single muons

The energy distribution of single muons is parametrized in MUPAGE as

$$\frac{\mathrm{d}N}{d(\log_{10}E_\mu)} = G \cdot E_\mu \mathrm{e}^{\beta X(1-\gamma)}[E_\mu + \epsilon(1-\mathrm{e}^{-\beta X})]^{-\gamma}. \tag{4.13}$$

Here E_μ [TeV] is the muon energy, $X = h/\cos\theta$ [km.w.e] is the slant depth, and ϵ, β, γ are free parameters. The constant G is a normalization factor:

$$G = 2.3 \cdot (\gamma - 1) \cdot \epsilon^{(\gamma-1)} \cdot \mathrm{e}^{(\gamma-1)\beta X} \cdot (1-\mathrm{e}^{-\beta X})^{(\gamma-1)}. \tag{4.14}$$

To obtain the new values of the single muon energy parameters, the normalized energy distributions were fitted with Eq. 4.13 at 40 different values of $\cos\theta$ at each of the seven depths. The fitting range was set to 1 GeV <= E_μ <= 10 TeV. The value of the parameter β was fixed to $\beta = 0.420$ [km.w.e]$^{-1} = 4.2 \times 10^{-4}$ [hg $\cdot$ cm^{-2}]$^{-1}$ following the MUPAGE paper approach [161]. Hence, the two free parameters of the fit are γ and ϵ. Example of the fit of vertical muons ($0.975 \leq \cos\theta \leq 1.0$) at 2 km depth is shown in Fig. 4.12.

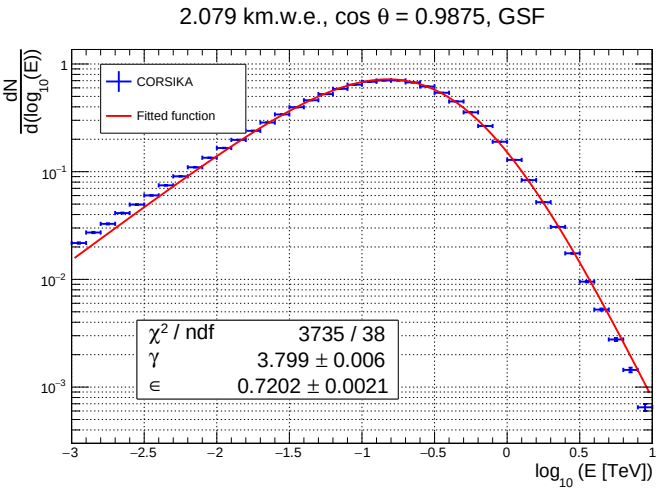

Figure 4.12: Fit of the CORSIKA simulation energy distribution of vertical muons at 2 km depth (blue points) with Eq. 4.13 (red line).

The parameter γ does not depend on the zenith angle in MUPAGE. Therefore, for every depth the γ distribution over $\cos\theta$ was fitted with a straight line, the fitting range was the same as mentioned in Sec. 4.3.2. Fig. 4.13 shows the fit results for 2 km depth. The $\gamma(\cos\theta)$ fit does not describe the energy fit result. However, this does not affect the final agreement between the tuned MUPAGE and the CORSIKA simulation results as shown below in Sec. 4.4.

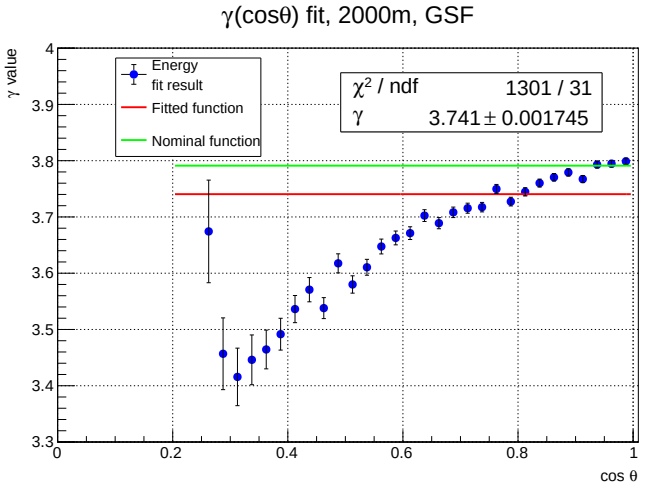

Figure 4.13: Fit of the γ parameter values as a function of $\cos\theta$ (red line) resulting from the single muon energy fit at 2 km depth (blue points). The green line was obtained with the nominal values of the parameters. The γ parameter is assumed to be independent of $\cos\theta$ so the fitting function is a straight line.

After obtaining values of the parameter γ at each depth, its depth dependence was fitted using the corresponding MUPAGE function (see Fig. 4.14 for the fit result):

$$\gamma(h) = \gamma_0 \cdot \ln(h) + \gamma_1. \tag{4.15}$$

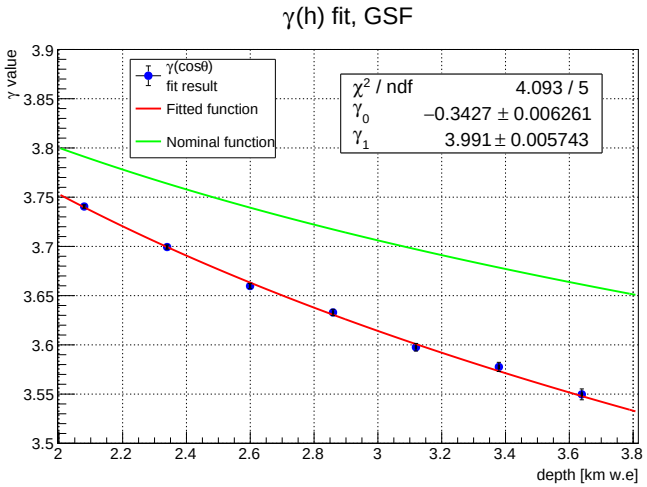

Figure 4.14: Fit of the parameter γ depth dependence (blue points) with Eq. 4.15 (red line). The green line represents the $\gamma(h)$ function with the parameter values fixed to the nominal ones.

Dependence of the parameter ϵ on $\cos\theta$ at a given depth is parametrized in MUPAGE as

$$\epsilon(h;\theta) = \epsilon_0(h) \cdot \sec\theta + \epsilon_1(h) \tag{4.16}$$

The result of the parameter $\epsilon(\cos\theta)$ fit at 2 km depth is shown on Fig. 4.15.

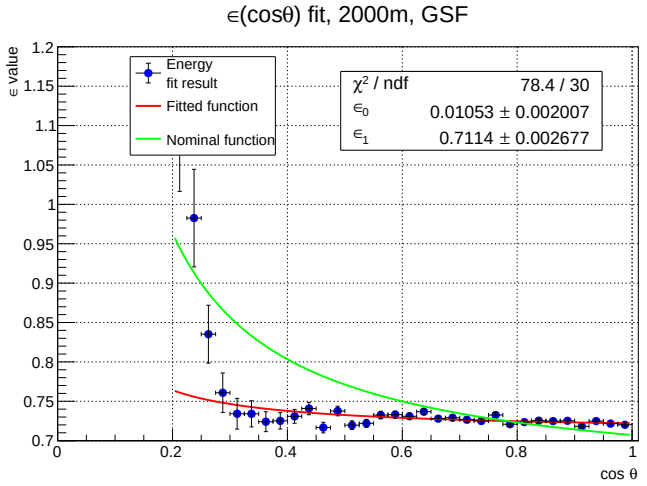

Figure 4.15: Fit of the parameter ϵ dependence on $\cos\theta$ (blue points) with Eq. 4.16 (red line) at 2 km depth. The green line is the nominal MUPAGE function shown for comparison.

The fit result of the ϵ_0 and ϵ_1 depth dependence is plotted on Fig. 4.16. The following MUPAGE equations were used in the fit:

$$\epsilon_0(h) = \epsilon_{0a} \cdot \mathrm{e}^{\epsilon_{0b} h}, \tag{4.17}$$

$$\epsilon_1(h) = \epsilon_{1a} \cdot h + \epsilon_{1b}. \tag{4.18}$$

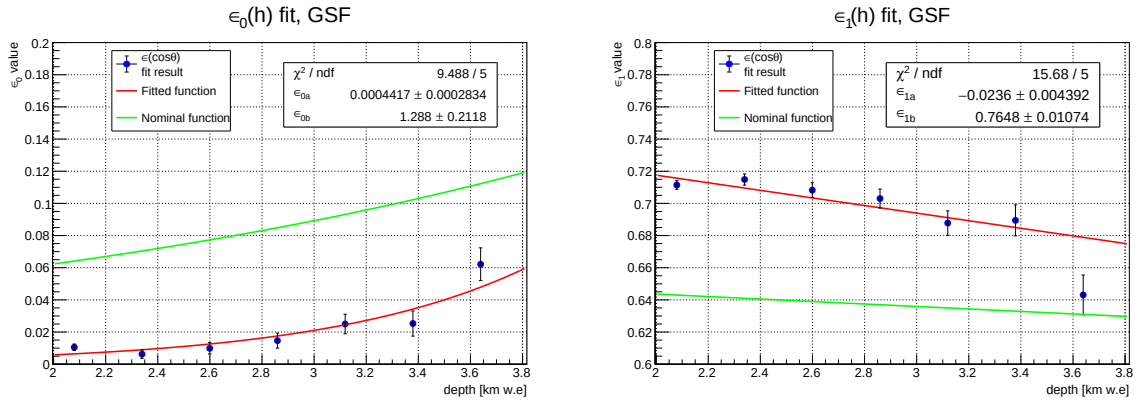

Figure 4.16: The ϵ_0 (left plot) and ϵ_1 (right plot) values obtained from the ϵ angular dependence fit at each depth (blue points). The values were fitted with Eq. 4.17 and Eq. 4.18 correspondingly, red lines. The same functions with the nominal MUPAGE parameter values are plotted in green.

A list of the parameters which describe the single muon energy distribution is reported in Table 4.3.

Name	Nominal Value	Fitted value
β (fixed)	0.420	0.420
γ_0	-0.232	-0.343
γ_1	3.961	3.991
ϵ_{0a}	0.0304	0.0004
ϵ_{0b}	0.359	1.288
ϵ_{1a}	-0.0077	-0.0236
ϵ_{1b}	0.659	0.765

Table 4.3: List of the nominal and fitted parameters that are used in the MUPAGE functions that describe the energy spectrum of single muons.

Fig. 4.17 illustrates the ratios of the normalized single muon energy distribution from the CORSIKA simulation with respect to the nominal and fitted MUPAGE functions for vertical muons at 2 and 3.5 km depths. The ratio is close to one in the energy range from 10 GeV up to 1 TeV for both the nominal and the fitted functions. The functions underestimate the CORSIKA energy distribution for $E_\mu < 10$ GeV and overestimate it for $E_\mu > 1$ TeV. The ratio is better for more vertical muons with $0.5 \leq \cos\theta \leq 0.525$, Fig. 4.18.

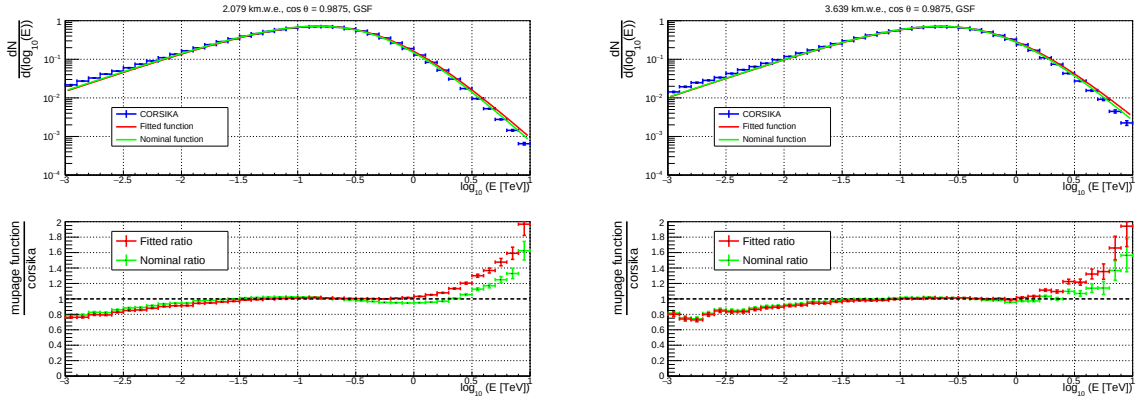

Figure 4.17: Normalized energy spectrum of vertical ($0.975 \leq \cos\theta \leq 1.0$) single muons from the CORSIKA simulation (blue points) compared to the corresponding nominal (green line) and fitted (red line) MUPAGE functions at 2 (left plot) and 3.5 km (right plot) depths.

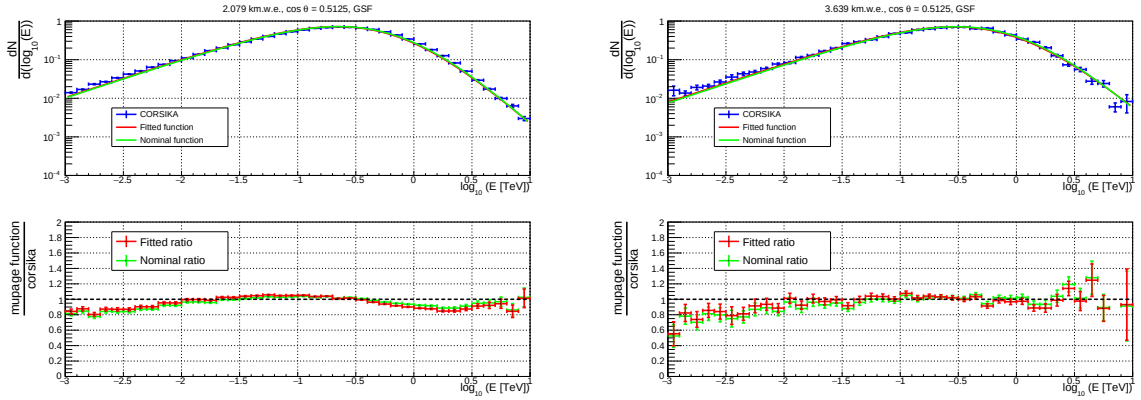

Figure 4.18: Ratios of the CORSIKA energy distribution (blue points) and the MUPAGE functions (green - nominal, red - fitted) for inclined muons with $0.5 \leq \cos\theta \leq 0.525$. The left plot shows the results for 2 km depth, the right one is for 3.5 km.

4.3.4 Lateral spread of multiple muons in the bundles

The MUPAGE function that describes the normalized muon lateral distribution in a plane perpendicular to the bundle axis is

$$\frac{dN}{dR} = C\frac{R}{(R+R_0)^{\alpha}}, \tag{4.19}$$

where dN is the number of muons in dR lateral distance interval, R_0 and α are parameters, and C is the normalization factor, $C = (\alpha-1)(\alpha-2)R_0^{\alpha-2}$. The average value of the radial distribution $< R >$ depends on R_0 and α: $< R >= 2R_0/(\alpha-3)$. Following the MUPAGE paper, the parameter $< R >$ was used in the fit. The dependence of $< R >$ on depth, zenith angle, and multiplicity is factorized into two variables, $\rho(m,h)$ and $F(\theta)$:

$$< R >= \rho(m,h) \cdot F(\theta). \tag{4.20}$$

The fit was performed for seven depths, 3 multiplicities (2, 3, and ≥ 4 muons in the bundles), and 10 values of θ, from 0 to $\pi/2$ radians. In the following formulas, the variable M is used, which is defined as

$$\begin{aligned} M &= m, \text{ if } m \leq 3, \\ M &= 4, \text{ if } m \geq 4. \end{aligned} \tag{4.21}$$

Since $< R >$ is assumed to be independent of the zenith angle up to $\sim 50°$, the lateral distribution was fitted for the vertical muon bundles first, ignoring $F(\theta)$. Thus, the fitting formula has 2 free parameters, α and ρ:

$$\frac{dN}{dR} = C\frac{R}{(R+R_0)^{\alpha}} = 0.5(\alpha-1)(\alpha-2)(\alpha-3)\rho^{\alpha-2}\frac{R}{(R+0.5(\alpha-3)\rho)^{\alpha}}. \tag{4.22}$$

The result of the lateral spread fit of the vertical ($0.0 \leq \theta \leq 0.157$ radians) bundles containing 2 muons at 2 km depth is presented in Fig. 4.19.

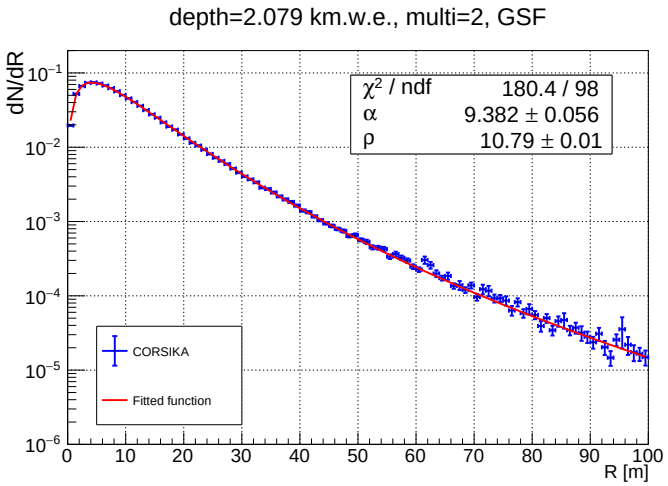

Figure 4.19: Fit of the CORSIKA lateral distribution of vertical muons from the bundles containing 2 muons at 2 km depth (blue points) with Eq. 4.22 (red line).

At a given multiplicity, the parameter α dependence on depth which is expressed in MUPAGE as

$$\alpha(M;h) = \alpha_0(M) \cdot \mathrm{e}^{\alpha_1(M)h}. \tag{4.23}$$

For each of the three multiplicities, the α depth dependence was fitted with Eq. 4.23 (see Fig. 4.20 for the fit result for $M = 2$).

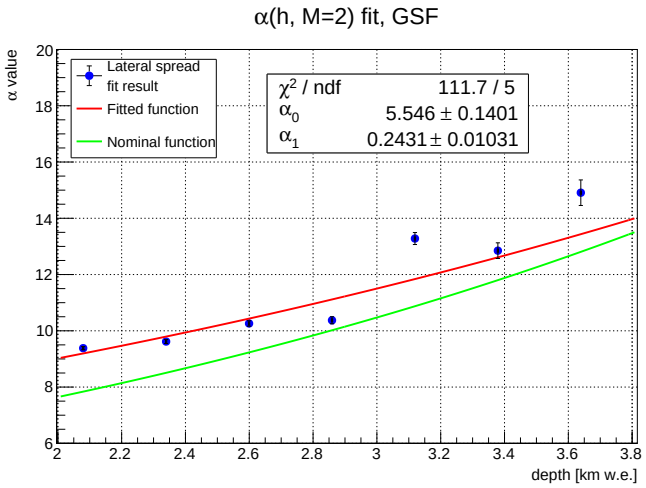

Figure 4.20: Fit of the parameter α dependence on depth for $M = 2$ (blue points) with Eq. 4.23 (red line). The green line is for the function with the nominal MUPAGE parameters.

The function that describes dependence of the parameters α_0 and α_1 on multiplicity is

$$\begin{aligned} \alpha_0(M) &= \alpha_{0a} \cdot M + \alpha_{0b}, \\ \alpha_1(M) &= \alpha_{1a} \cdot M + \alpha_{1b}. \end{aligned} \tag{4.24}$$

The $\alpha_0(M)$ and $\alpha_1(M)$ fit results are on Fig. 4.21.

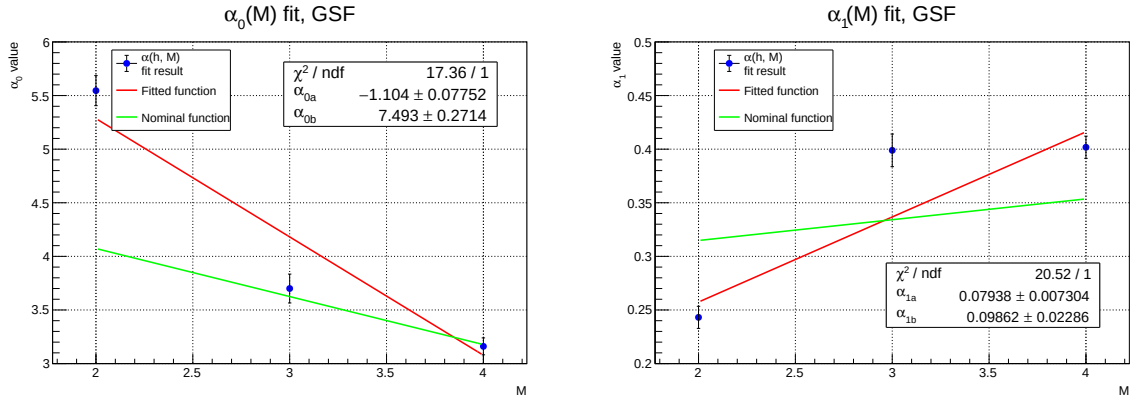

Figure 4.21: Results of the $\alpha(h)$ fit for three multiplicities, blue points. The red line is the fit of the results with Eq. 4.24. The green line is the same function but with the parameters that are kept nominal.

.

As for the parameter ρ, at a given multiplicity it depends on h as

$$\rho(M; h) = \rho_0(M) \cdot h^{\rho_1(M)}. \tag{4.25}$$

Fig. 4.22 shows the fit result for $M = 2$.

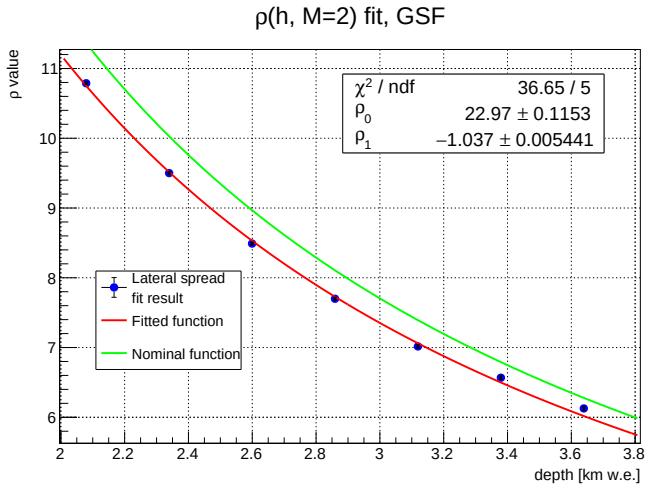

Figure 4.22: Fit of the parameter ρ dependence on depth for $M = 2$ (blue points) with Eq. 4.25 (red line). The nominal MUPAGE function is the green line.

For a given h, the parameter ρ_0 linearly depends on M (Eq. 4.26) while ρ_1 is considered to be independent of M (Eq. 4.27). Fig. 4.23 shows the $\rho_0(M)$ and $\rho_1(M)$ fit results.

$$\rho_0(M) = \rho_{0a} \cdot M + \rho_{0b}, \tag{4.26}$$

$$\rho_1(M) = \rho_1. \tag{4.27}$$

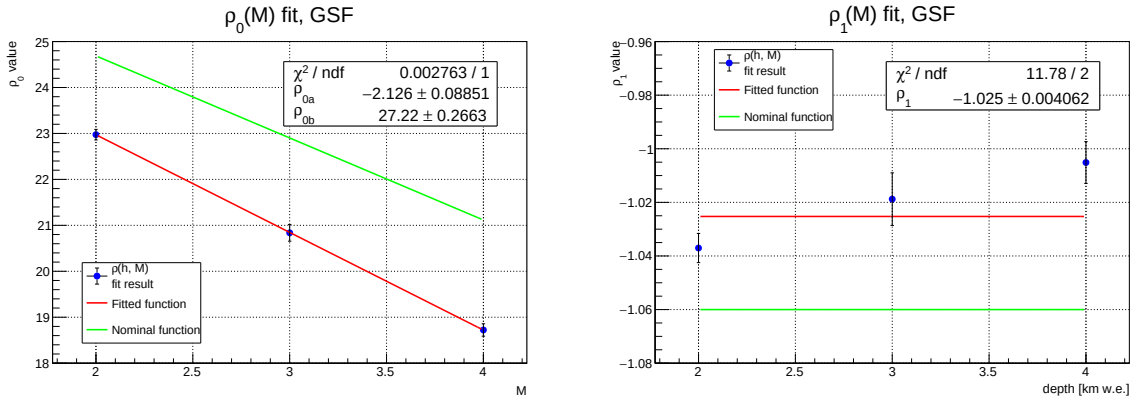

Figure 4.23: The $\rho_0(h)$ and $\rho_1(h)$ values (blue points) fitted with Eq. 4.26 and Eq. 4.27, correspondingly. The red lines are the fitted functions, the green lines are the nominal functions.

.

The parameters ρ and α that were fitted above describe the radial distribution of muons in the vertical bundles. Zenith dependence of $< R >$ is parametrized in MUPAGE as

$$F(\theta) = \frac{1}{e^{(\theta-\theta_0)f} + 1}. \tag{4.28}$$

However, the CORSIKA simulation results show that the average value of the radial distance slightly increases with θ which cannot be described with Eq. 4.28 (see Fig. 4.24 for $M = 2$ at 2 km depth). Hence, the value of the parameter θ_0 was fixed to 10 in order to have $< R >$ value independent of θ, and the parameter f was fixed to the nominal value.

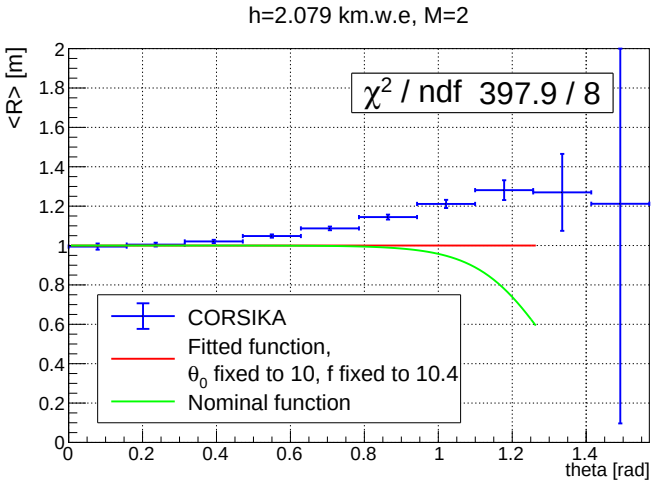

Figure 4.24: Average value of the radial distance as a function of θ for 2 km depth and for $M = 2$, blue points. The green line is the nominal MUPAGE function, the red line is the same function but with θ_0 value fixed to 10.0.

List of the parameters that describe the lateral spread distribution is available in Table 4.4.

Name	Nominal Value	Fitted value
ρ_{0a}	-1.786	-2.126
ρ_{0b}	28.26	27.22
ρ_1	-1.06	-1.03
θ_0	1.3	10.0
f	10.4	10.4
α_{0a}	-0.448	-1.104
α_{0b}	4.969	7.493
α_{1a}	0.0194	0.0794
α_{1b}	0.276	0.099

Table 4.4: The nominal and fitted MUPAGE parameters for the lateral spread of muons in the bundles.

The ratio of the CORSIKA lateral distribution and the MUPAGE functions for vertical ($0.0 \leq \theta \leq 0.157$ radians) muon bundles with $M = 2$ at 2 and 3.5 km depths is shown in Fig. 4.25. The ratio for the inclined bundles with $0.628 \leq \theta \leq 0.785$ radians is reported on Fig. 4.26. The fitted functions does not follow the CORSIKA distributions for the inclined muons since the MUPAGE function cannot describe $< R > (\theta)$ dependence. However, this discrepancy does not affect the final tuning results.

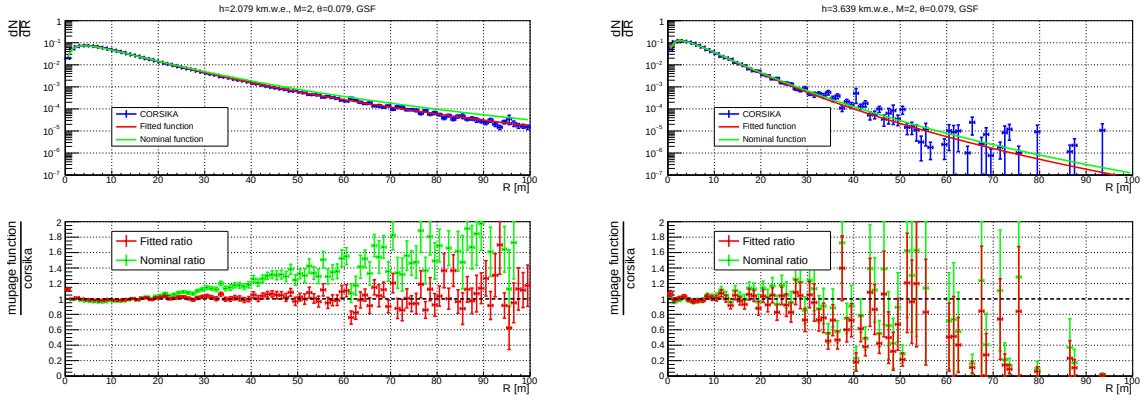

Figure 4.25: Ratio of the CORSIKA normalized lateral distribution (blue points) and the corresponding nominal (green line) and fitted (red line) MUPAGE functions for vertical muon bundles ($0.0 \leq \theta \leq 0.157$ radians) with $M = 2$ at 2 (left plot) and 3.5 (right plot) km depths.

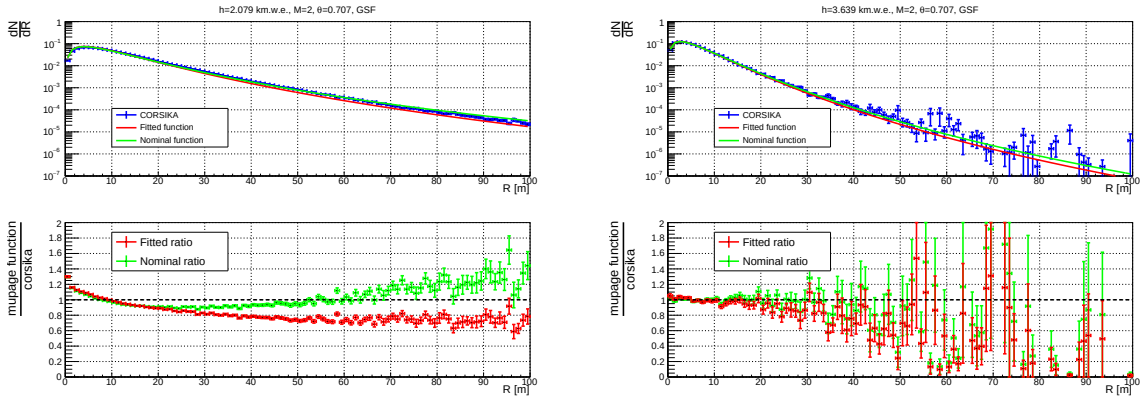

Figure 4.26: Lateral distribution ratios for the inclined muon bundles, $0.628 \leq \theta \leq 0.785$ radians. The color scheme is the same as in the ratio plot above.

4.3.5 Energy spectrum of multiple muons in the bundles

The energy spectrum of multiple muons in the bundles is described in MUPAGE by the same function as for the single muons, Eq. 4.13. The parameter β is also fixed to $\beta = 0.420$ [km.w.e]$^{-1}$ $= 4.2 \times 10^{-4}$ [hg $\cdot$ cm^{-2}]$^{-1}$. The parameters γ and ϵ depend on the vertical depth h, the zenith angle θ, the bundle multiplicity M, and the radial distance R of the muons from the bundle axis.

The fit did not converge for all the histograms, only the successful fit results were used in the following.

As a first step, the energy spectrum of muons was fitted with Eq. 4.13. The fit was performed at 7 depths, 4 intervals of the zenith angle ($0° - 20°$, $20° - 40°$, $40° - 60°$, and $60° - 80°$), 3 values of M (2, 3, and 4), and six intervals of R ($0-5$ m, $5-10$ m, $10-15$ m, $15-25$ m, $25-45$ m, ≥ 45 m). Therefore, 504 histograms were fitted. An example of the fit at 2 km depth for the bundles with $0° \leq \theta \leq 20°$, $M = 2$, and $0 \leq R \leq 5$ m, is shown in Fig. 4.27.

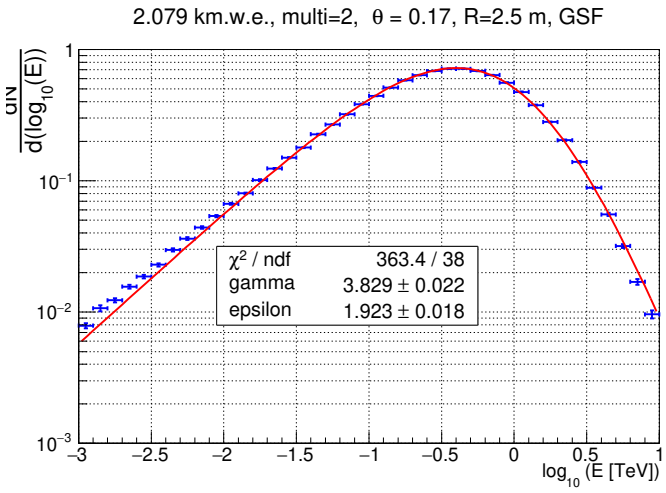

Figure 4.27: Energy spectrum of muons in the bundles with $0° \leq \theta \leq 20°$, $M = 2$, and $0 \leq R \leq$ 5m at 2 km depth (blue points) fitted with Eq. 4.13 (red line).

The parameter γ is assumed to be independent of θ, hence for each h, M, and R, the parameter γ over θ distributions were fitted with a straight line, see Fig. 4.28 for $h = 2.079$ km.w.e, $M = 2$, $0 \leq R \leq 5$ m fit result.

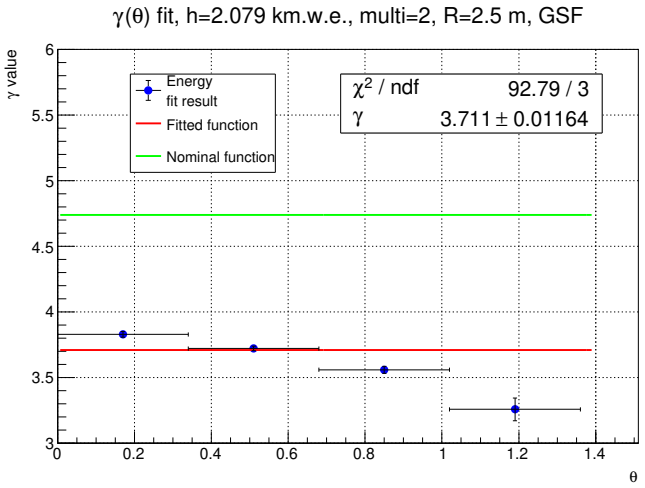

Figure 4.28: The parameter γ values obtained from the energy spectrum fit of muons in the bundles at 2 km depth with $M = 2$, $0 \leq R \leq 5$ m (blue points) fitted with a constant function (red line). The nominal function is plotted in green.

The parameter γ dependence on R is expressed as

$$\gamma(h, M; R) = a(h) \cdot R + b(h, M) \cdot (1 - 0.5e^{q(h)R}). \tag{4.29}$$

An example of the $\gamma(R)$ fit for 2 km depth and $M = 2$ is shown in Fig. 4.29. The $\gamma(R)$ fit did not converge for all the histograms.

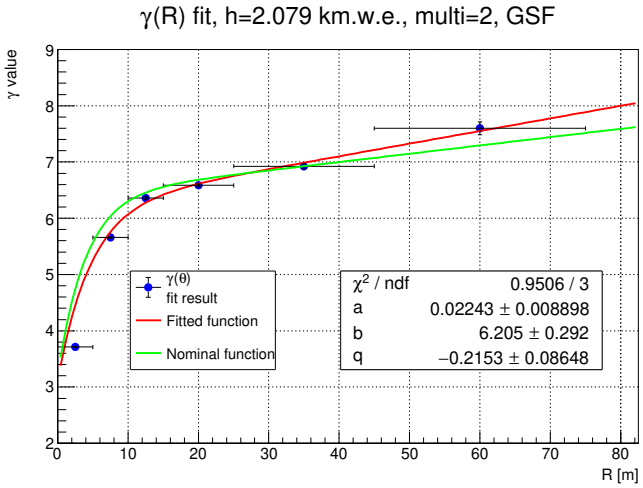

Figure 4.29: The parameter γ dependence on the distance of muons from the bundle axis (blue points) fitted with Eq. 4.29 (red line). The green line is the nominal function.

The parameter a does not depend on M in MUPAGE so its values at a given depth for different multiplicities were fitted with a straight line. The fit for 2 km depth is in Fig. 4.30.

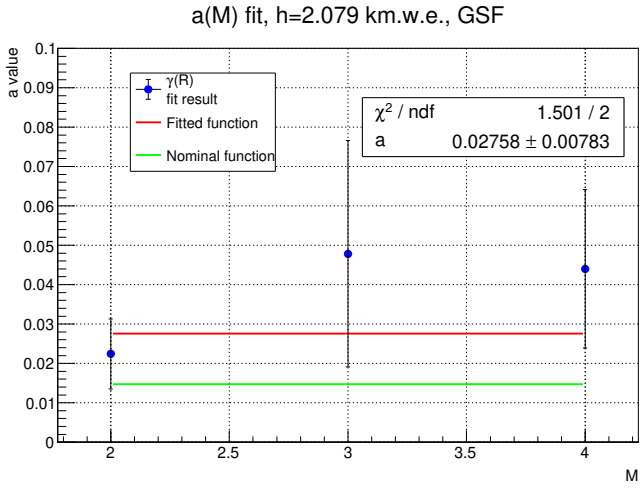

Figure 4.30: The values of the parameter a for different M at 2 km depth, blue points. The values were fitted with a straight line shown red. The green line shows the nominal function.

The dependence of the parameter a on depth is linear,

$$a(h) = a_0 \cdot h + a_1. \tag{4.30}$$

The $a(h)$ fit result is in Fig. 4.31.

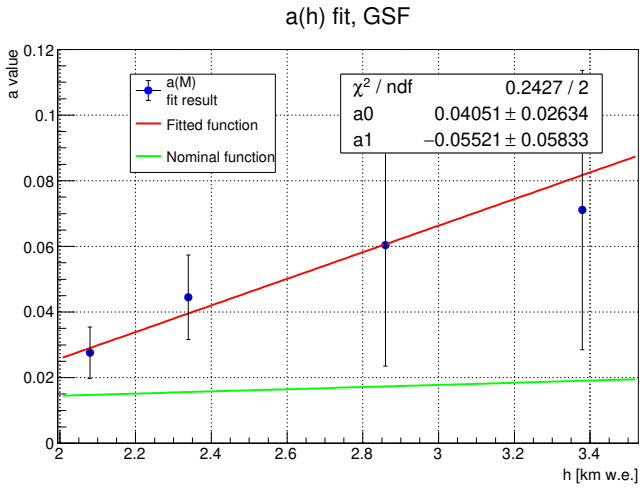

Figure 4.31: Results of the $a(M)$ fit. The fit converged only at 4 depths hence there are only 4 blue points. The points were fitted with Eq. 4.30, red line. The Eq. 4.30 with the nominal a_0 and a_1 values is shown in green.

The parameter b depends on both depth and multiplicity, its depth dependence is

$$b(M;h) = b_0(M) \cdot h + b_1(M). \tag{4.31}$$

An example of the parameter b fit over h for $M = 2$ is in Fig. 4.32.

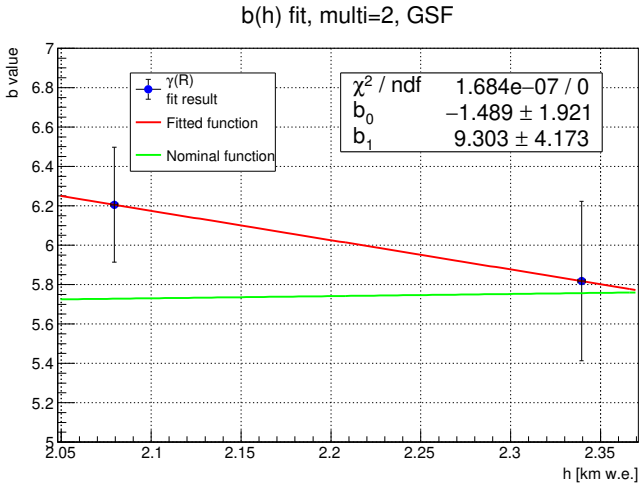

Figure 4.32: Fit of the parameter b dependence on depth (blue points) with Eq. 4.31 (red line). The green line shows the nominal MUPAGE function.

Dependencies of both b_0 and b_1 on M are linear, Eq. 4.32 and 4.33. Fig. 4.33 shows the fit results.

$$b_0(M) = b_{0a} \cdot M + b_{0b}, \tag{4.32}$$

$$b_1(M) = b_{1a} \cdot M + b_{1b}. \tag{4.33}$$

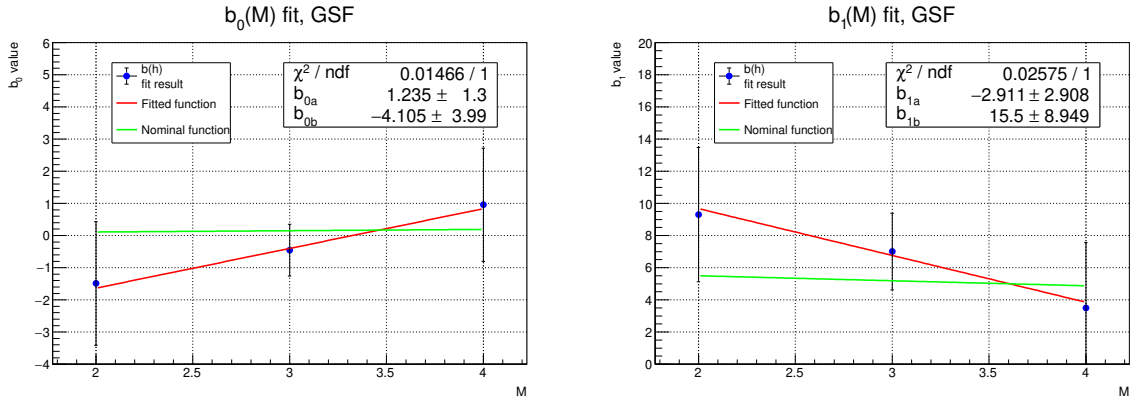

Figure 4.33: Left (right) plot illustrates the parameter b_0 (b_1) fit over multiplicity with Eq. 4.32 (Eq. 4.33). The values of the parameters are shown in blue. The red (green) line is the fitted (nominal) MUPAGE function.

The parameter q does not depend on multiplicity (see Fig. 4.34 for 2 km depth fit) and linearly depends on depth:

$$q(h) = q_0 \cdot h + q_1. \tag{4.34}$$

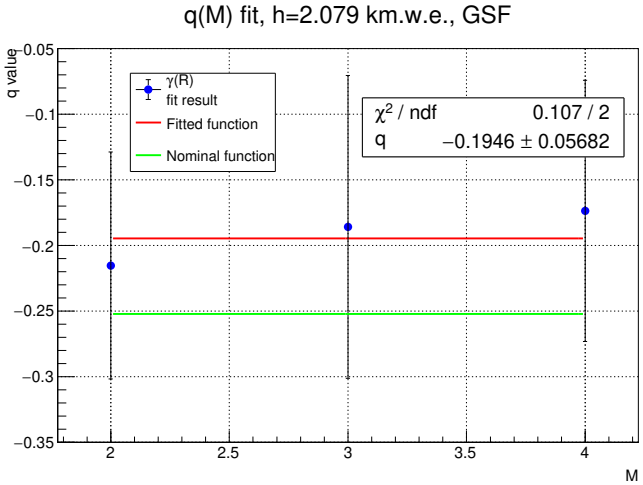

Figure 4.34: The parameter q values over M (blue points) fitted with a straight line (red) at 2 km depth. The nominal function is shown in green.

The $q(h)$ fit results are in Fig. 4.35.

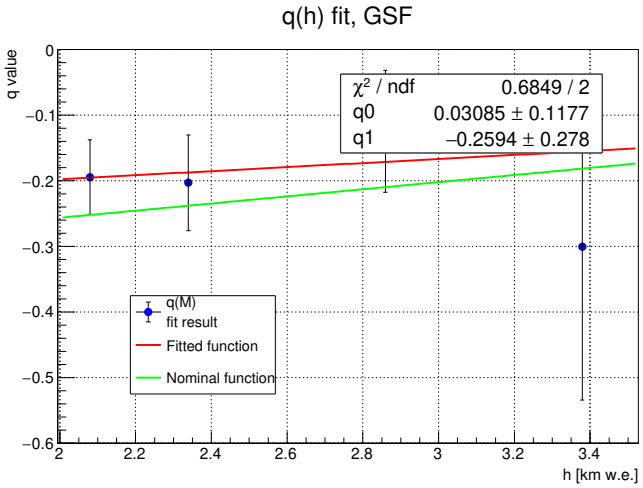

Figure 4.35: Fit of the parameter q dependence on depth (blue pints) with Eq. 4.34 (red line). The green line is for the MUPAGE function with the nominal parameters.

Regarding the parameter ϵ, it is assumed to be independent of M, hence for every h, θ, and R, the values of ϵ over M were fitted with a straight line (Fig. 4.36 illustrates one example of the fit).

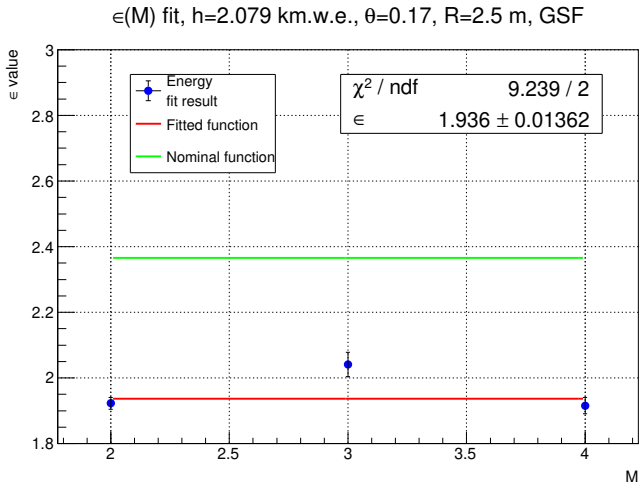

Figure 4.36: The $\epsilon(M)$ values from the energy fit of the bundles at 2km depth with $0° \leq \theta \leq 20°$ and $0 \leq R \leq 5$m, blue points. The red (green) line is the fitted (nominal) function.

The parameter ϵ depends on the zenith angle which is parametrized as

$$\epsilon(h, R; \theta) = c(R, h) \cdot \theta + d(R, h) \tag{4.35}$$

Fig. 4.37 shows the $\epsilon(\theta)$ fit result for 2 km depth and $0 \leq R \leq 5$ m. The fit did not converge due to the incorrect error estimation of the second point. The error is estimated from the $\epsilon(M)$ fit which did not correctly converge and resulted in too small error value. Hence, the $\epsilon(\theta)$ fit tends to pass through the second point which leads to the wrong fit results.

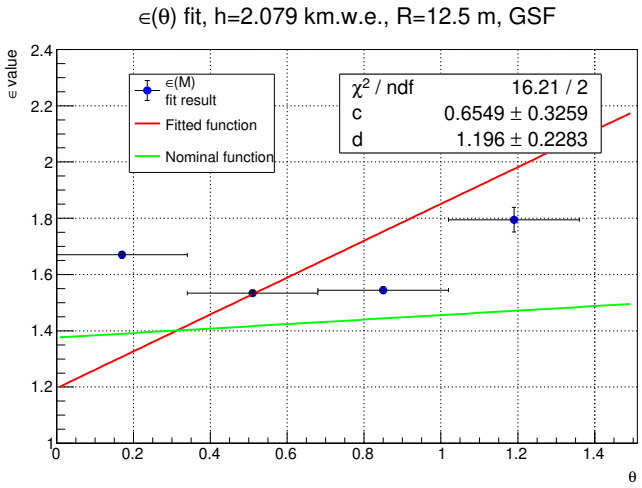

Figure 4.37: Values of the parameter ϵ from the energy spectrum fit of the bundles at 2 km depth with $M = 2$ and $0 \leq R \leq 5$ m as a function of θ (blue points) fitted with Eq. 4.35 (red line). The nominal function is shown in green.

The parameters c and d depend on h and R. For the radial distance dependence, the parametrization is the following (the fit results for 2 km depths are on Fig. 4.38 and 4.39):

$$c(h; R) = c_0(h) \cdot \mathrm{e}^{c_1 R} \tag{4.36}$$

$$d(h; R) = d_0(h) \cdot R^{d_1(h)} \tag{4.37}$$

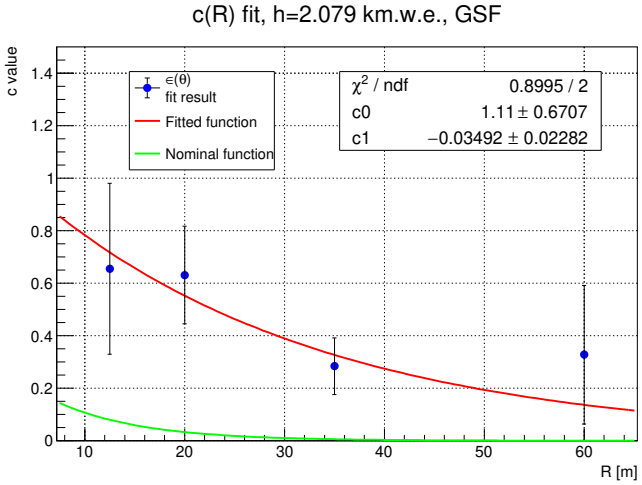

Figure 4.38: Fit of the $c(R)$ values (blue points) with Eq. 4.36 (red line) at 2 km depth. The green line shows the nominal MUPAGE function.

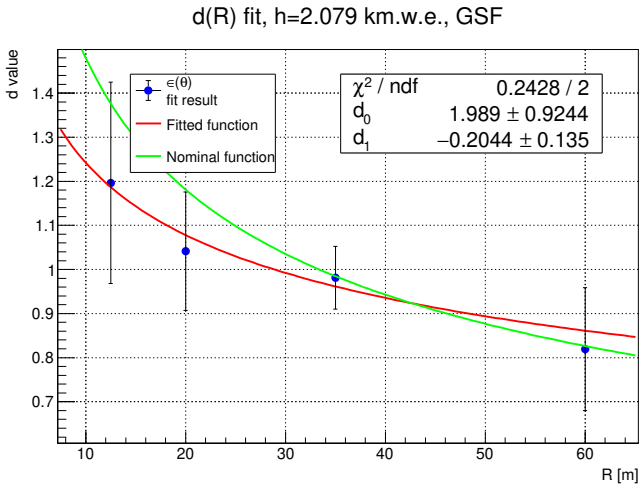

Figure 4.39: The values of the parameter d as a function of the radial distance at 2 km depth, blue points. The red line is the $d(R)$ dependence fit with Eq. 4.37. The green line is the same function but with the nominal values of the parameters.

The parameter c_0 depends on h linearly, while c_1 is independent of h:

$$c_0(h) = c_{0a} \cdot h + c_{0b} \tag{4.38}$$

$$c_1(h) = c_1 \tag{4.39}$$

The $c_0(h)$ and $c_1(h)$ fit results are on Fig. 4.40.

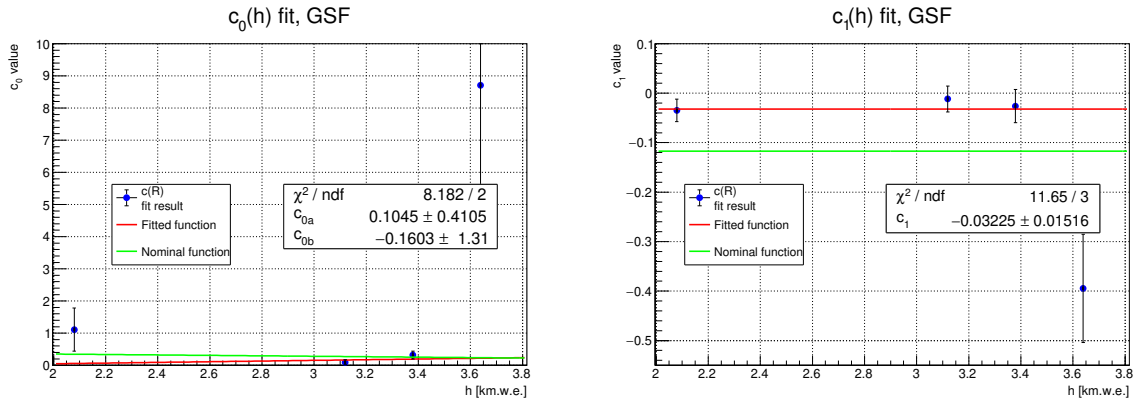

Figure 4.40: Left (right) plot shows the $c_0(h)$ ($c_1(h)$) distribution (blue points). The distributions were fitted with Eq. 4.38 and Eq. 4.39 correspondingly, red lines. The green lines are for the nominal functions.

Finally, the parameters d_0 and d_1 dependence on h is linear (the fit results are on Fig. 4.41):

$$d_0(h) = d_{0a} \cdot h + d_{0b} \tag{4.40}$$

$$d_1(h) = d_{1a} \cdot h + d_{1b} \tag{4.41}$$

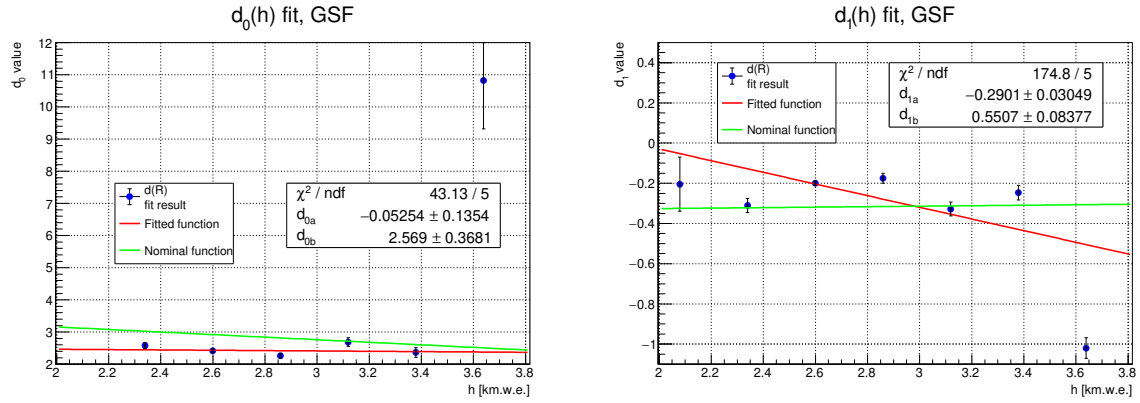

Figure 4.41: The left plot shows the parameter $d_0(h)$ dependence (blue points) fitted with Eq. 4.40 (red line). The green line is the nominal function. The right plot illustrates the fit of $d_1(h)$ dependence with Eq. 4.41, the color scheme is the same as for the left plot.

Ratios of the CORSIKA simulation energy spectrum of muons from the bundles at 2 and 3.5 km depths with $0° \leq \theta \leq 20°$, $M = 2$, and $0 \leq R \leq 5$m with respect to the nominal and fitted MUPAGE functions are presented on Fig. 4.42. Ratios for the bundles with the same properties but with $10 \leq R \leq 15$m are on Fig. 4.43.

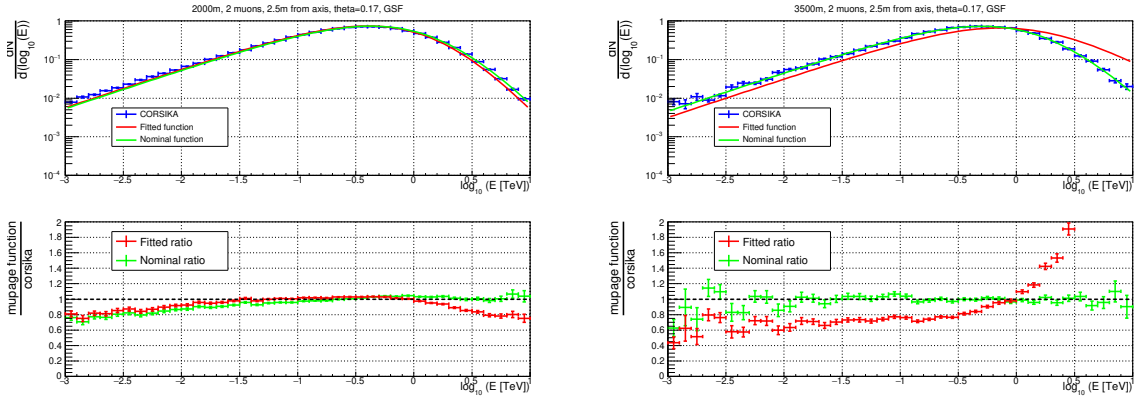

Figure 4.42: Ratio of the muon energy spectrum from the CORSIKA simulation for the bundles with $h = 2.079$ km.w.e. (left plot) and $h = 3.639$ km.w.e. (right plot), $0° \leq \theta \leq 20°$, $M = 2$, and $0 \leq R \leq 5$m (blue points) with respect to the nominal (green line) and fitted (red line) MUPAGE functions.

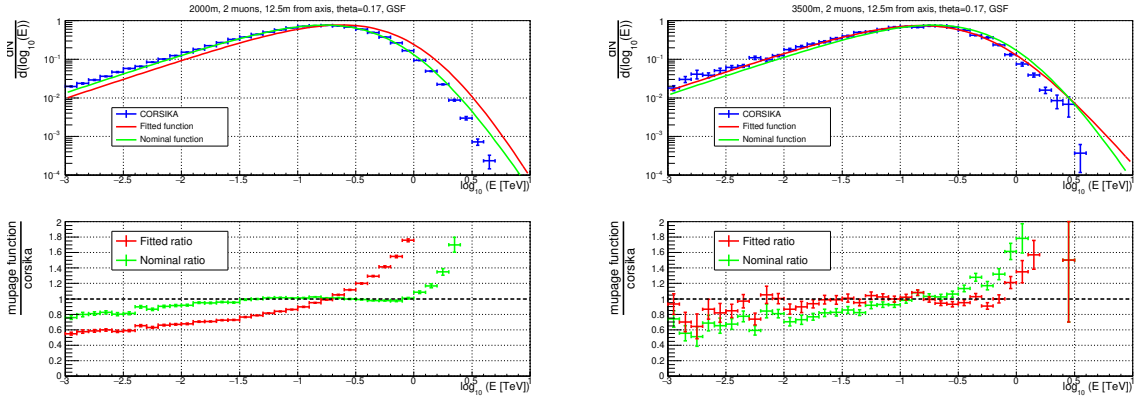

Figure 4.43: The CORSIKA energy spectrum of muons from the bundles with $h = 2.079$ km.w.e. (left plot) and $h = 3.639$ km.w.e. (right plot), $0° \leq \theta \leq 20°$, $M = 2$, and $10 \leq R \leq 15$m, blue points. The fitted MUPAGE function is shown in red, the nominal one is in green.

The ratio of the CORSIKA simulation results with respect to the MUPAGE functions is better for the nominal parameters due to the problems with the fit. Some MUPAGE functions does not describe the corresponding CORSIKA distributions which leads to the incorrect fit. Therefore, the parameters describing the energy spectrum of multiple muons in the bundles were kept nominal.

4.4 CORSIKA and MUPAGE comparison at the reconstruction level

In order to check whether the tuned MUPAGE describes the CORSIKA simulation at the reconstruction level, the reconstructed zenith angle and muon energy distributions resulting from the CORSIKA simulation and the MUPAGE one were compared. Also, two distributions containing the observables whose values are often used as the quality and anti-noise cuts were produced: the quality of the reconstruction (likelihood) and the number of photons (hits) on PMTs used in the reconstruction.

In general, the tuned MUPAGE follows the CORSIKA distribution for both the ORCA6 and ARCA6 detectors. Hence, the tuned MUPAGE can be used as a faster alternative to the CORSIKA full MC simulation. The tuned MUPAGE results can be considered as the ones obtained with CORSIKA without the need to perform the full simulation several times.

The framework developed in this work is provided to the KM3NeT Collaboration as the internally available code with all necessary documentation. This allows this work to be continued in the near future by the collaborators in order to extend the analysis for the larger and better KM3NeT detectors.

4.4.1 ORCA6

The results of the MUPAGE and CORSIKA comparisons for the ORCA6 detector at reconstruction level are presented below. The plot numbers and the χ^2/ndf values between the histograms which represent the tuned MUPAGE distributions and the CORSIKA ones for different observables are reported in Table 4.5.

Observable name	Figure	χ^2/ndf value
Reconstructed zenith	4.44	1.86
Reconstructed energy	4.45	1.99
Likelihood of the reconstruction	4.46	1.40
Number of hits	4.47	1.20

Table 4.5: The MUPAGE and CORSIKA comparison at the reconstruction level for ORCA6.

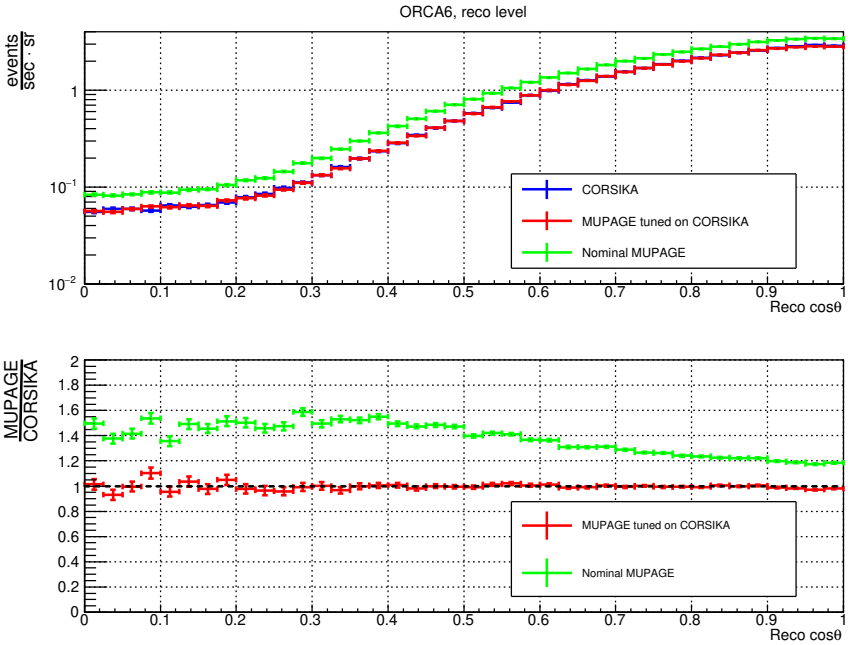

Figure 4.44: The rate of muons reconstructed with the ORCA6 detector as a function of the zenith angle. The blue (red) points represent the CORSIKA (MUPAGE tuned on CORSIKA) simulation. The nominal MUPAGE provides the distribution shown in green points. The ratios between the MUPAGE and CORSIKA are on the bottom plot.

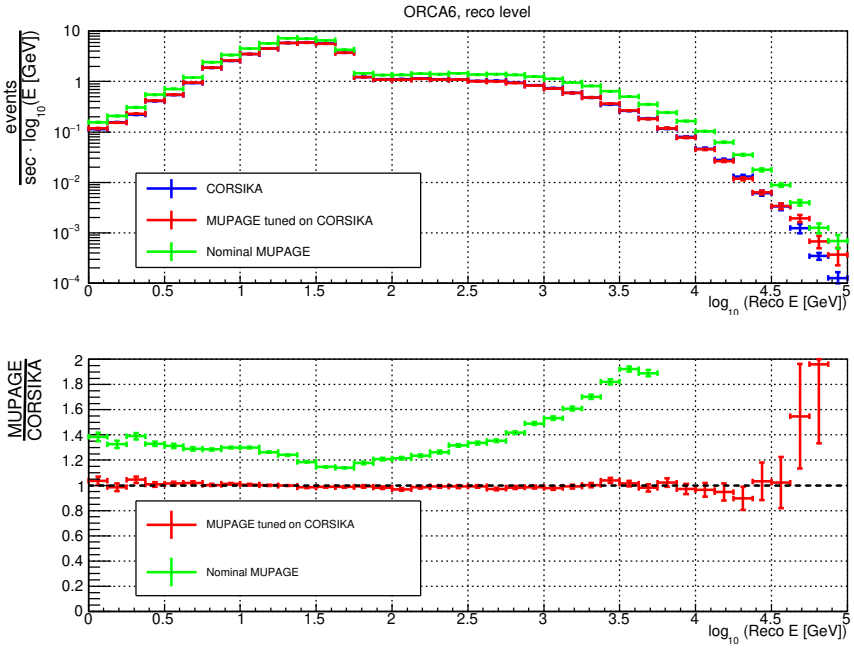

Figure 4.45: Ratio for the ORCA6 reconstructed energy distribution; blue points - CORSIKA, red points - MUPAGE tuned on CORSIKA, and green points - nominal MUPAGE. The ratios between the MUPAGE and CORSIKA are on the bottom plot.

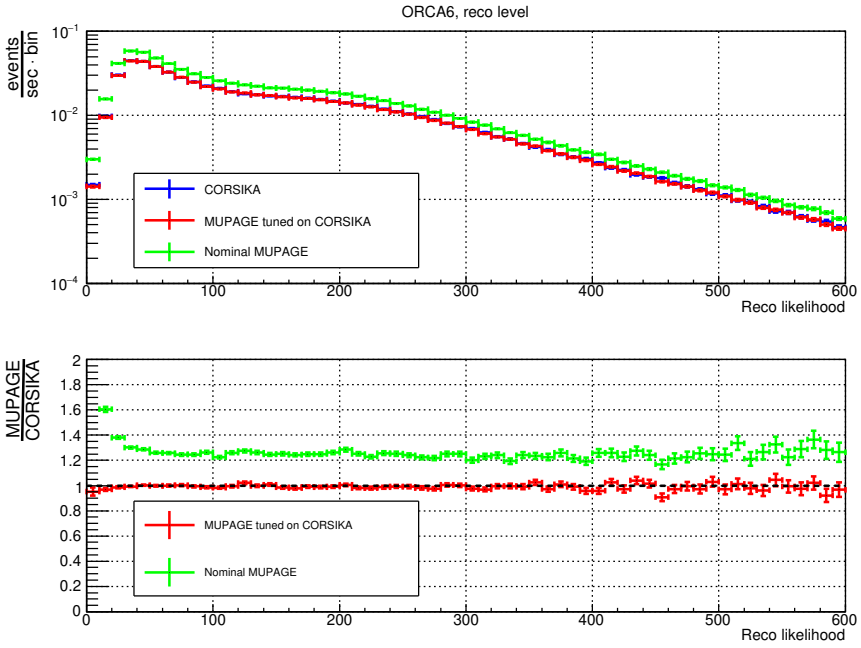

Figure 4.46: The event rate as a function of the reconstruction likelihood for the ORCA6 telescope. The red points were obtained using MUPAGE tuned on CORSIKA, the blue points are the results of the CORSIKA simulations, the green points are the nominal MUPAGE. The MUPAGE/CORSIKA ratios are on the bottom plot.

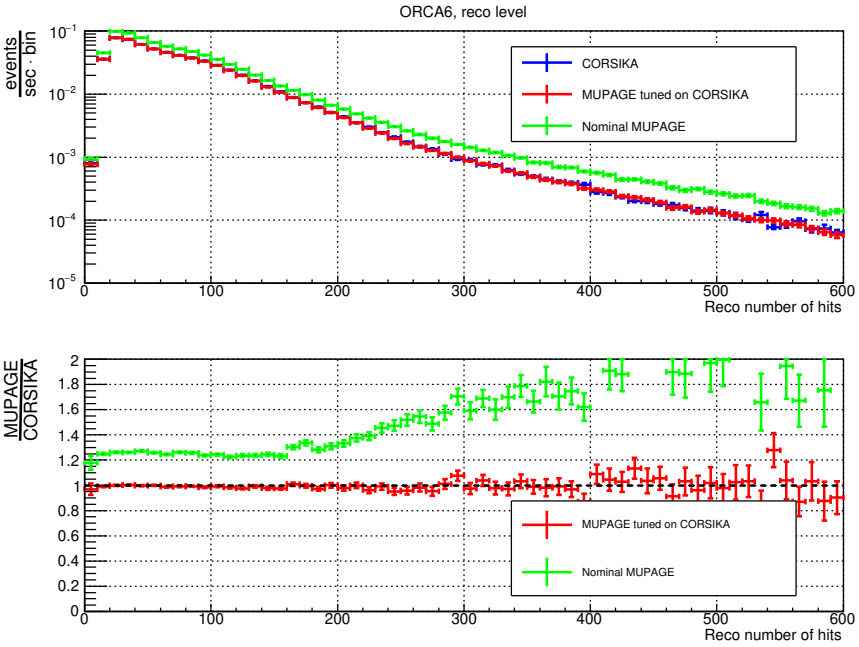

Figure 4.47: Comparison of the number of hits used in the reconstruction resulting from the CORSIKA simulation (blue points) and the tuned MUPAGE one (red points) for the ORCA6 detector. The nominal MUPAGE is shown in green for comparison. The ratios between the MUPAGE distributions and the CORSIKA one is on the bottom plot.

4.4.2 ARCA6

The results of the MUPAGE and CORSIKA comparisons for the ARCA6 detector at the reconstruction level are listed in Table 4.6.

Observable name	Figure	χ^2/ndf value
Reconstructed zenith	4.48	0.70
Reconstructed energy	4.49	1.74
Reconstructed likelihood	4.50	2.31
Reconstructed number of hits	4.51	2.74

Table 4.6: The plot numbers and the χ^2/ndf values for the corresponding MUPAGE and CORSIKA histograms for ARCA6.

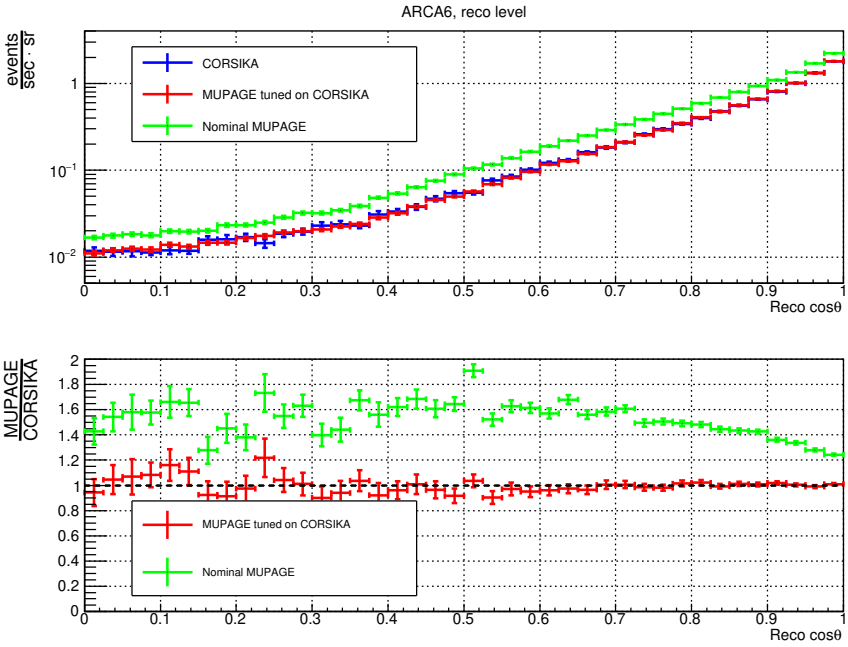

Figure 4.48: The CORSIKA (MUPAGE tuned on CORSIKA) zenith angle distribution for the ARCA6 detector, blue (red) points. The nominal MUPAGE is in green. The MUPAGE/CORSIKA ratios are on the bottom plot.

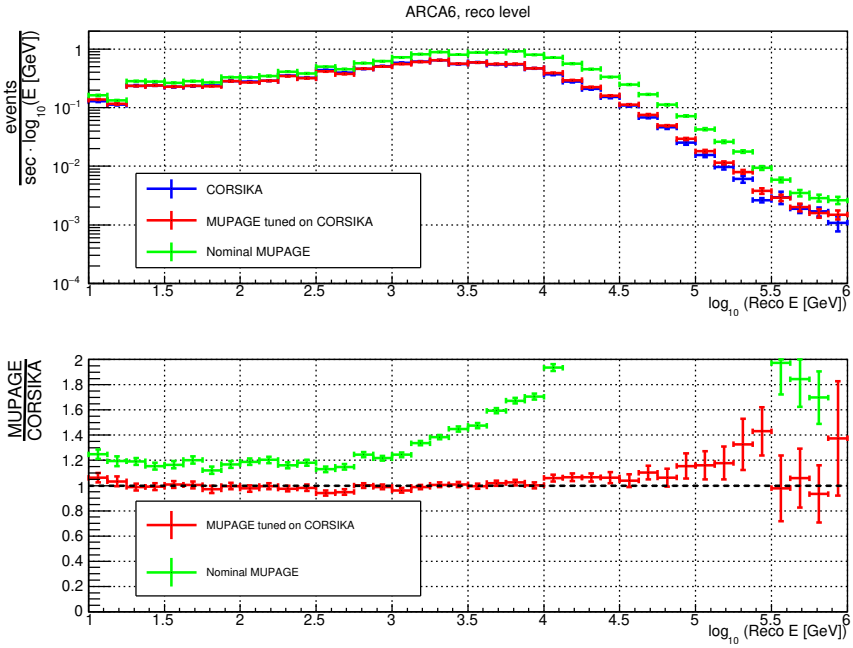

Figure 4.49: The ARCA6 event rate as a function of the reconstructed energy for the CORSIKA (blue points) and the tuned MUPAGE (red points) simulation results. The ratios between the MUAPGE and CORSIKA distributions are on the bottom plot, the green points represent the nominal MUPAGE.

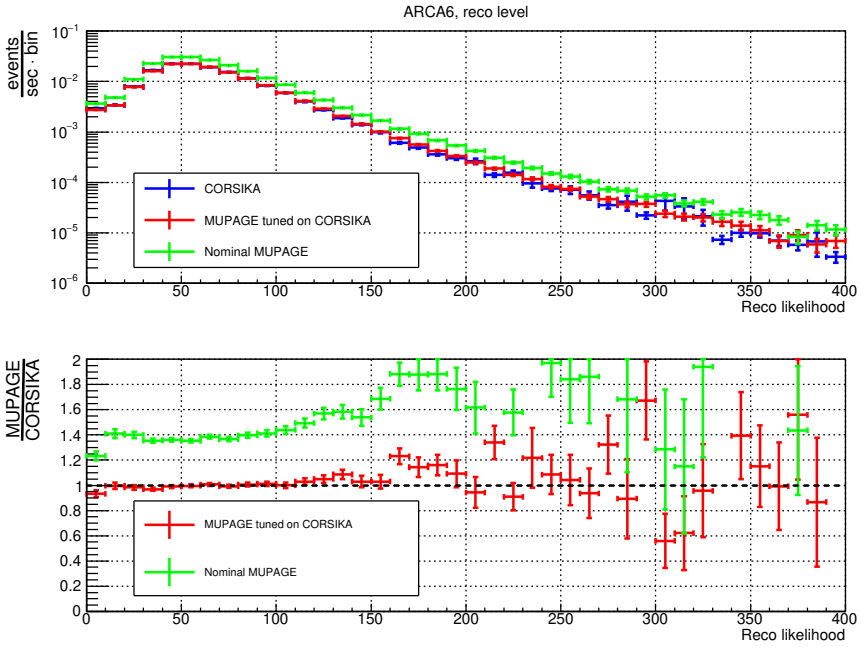

Figure 4.50: The likelihood distribution ratio for the ARCA6 telescope; blue points - CORSIKA, red points - MUPAGE tuned on CORSIKA, green points - nominal MUPAGE.

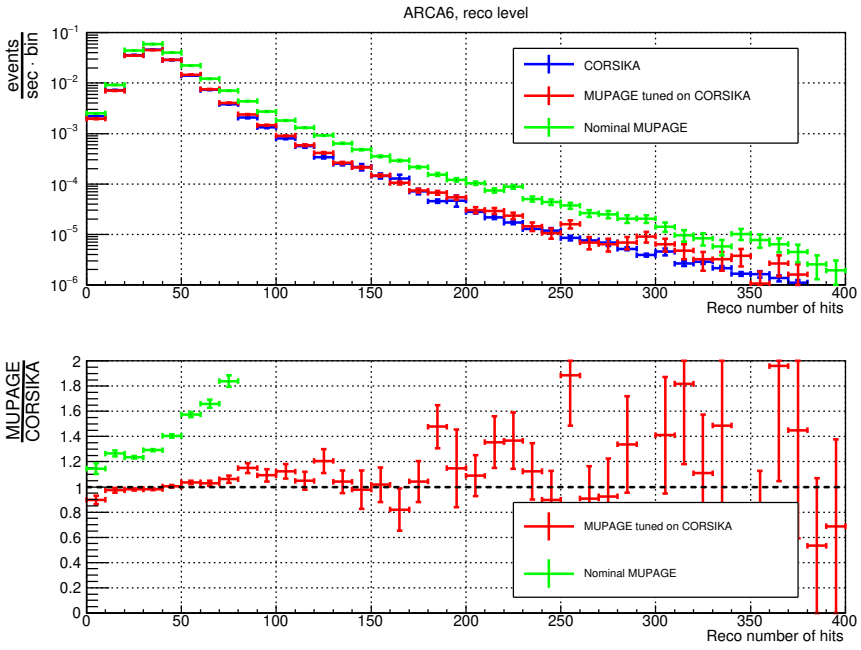

Figure 4.51: The number of hits used in the reconstruction resulted from the CORSIKA (blue points), the tuned (red points) and nominal (green points) MUPAGE simulations. The MUPAGE/CORSIKA ratios are on the bottom plot.

5 Comparison of the KM3NeT data with the MC simulations

This chapter is devoted to the comparison of the MC simulations with the KM3NeT data collected by the ORCA6 and ARCA6 telescopes. The simulations include the Sibyll 2.3d model [69] used for the description of hadronic interactions and GSF [19] used as the model for the mass composition of the CR flux. The simulations were performed with MUPAGE [161] tuned on CORSIKA [66]. The motivation to use MUPAGE instead of the full MC simulations and the tuning procedure are described in Chapter 4. The proof that the tuned MUPAGE correctly reproduces the CORSIKA results is presented in the same Chapter.

This chapter starts with a description of the sea level flux of high-energy muons, Sec. 5.1. The data detected by the KM3NeT telescopes contain also pure background events which include the decays of ^{40}K and the bioluminescent light [153]. In order to remove such events from the data sample, anti-noise cuts were applied, whose description is reported in Sec. 5.2. The muon energy and direction reconstruction performances are described in Sec. 5.3. Sec. 5.4 is devoted to the studies of systematic uncertainties considered for this analysis. Comparison of the KM3NeT data with the MC simulations is presented in Sec. 5.5. Finally, the discussion of the results is reported in Sec. 5.6.

5.1 Sea level flux of TeV muons

As it was discussed in Chapter 3, muons must have sufficient enough energy at sea level to be able to reach the depth of the KM3NeT telescopes (∼2 km for the top part of ORCA and ∼2.8 km for ARCA). Considering energy losses needed to be able to propagate to such depths, the sea level energy of muons detectable by the KM3NeT experiment lays in the TeV range. This muon energy is about 3 orders of magnitude higher than for the muons detected in EAS experiments. Thus, the KM3NeT measurement is complementary to the so-called muon puzzle, i.e. deficit of GeV muons detected on the ground as discussed in Chapter 3.

Measurements of the high-energy muon flux can be performed at sea level up to several TeV [164]. This threshold depends on the maximum detectable momentum of the spectrometer defined by the relative momentum resolution [165].

There are several experiments that were able to directly measure the TeV muon flux at sea level. A summary of the data from such experiments was provided in [166]. Fig. 5.1 shows the sea level muon flux resulting from the CORSIKA simulations used in this work for the MUPAGE tuning compared to the real data from the ground-based experiments. The data points shown in the figure are from the experiments mentioned in [166]: the Nottingham CR spectrometer [167] (Baber et al. points in the plot), the Nottingham spectrometer in its updated configuration [168] (Rastin points in the plot), the Durham CR spectrograph [169] (Hayman et al. points in the plot), and the Durgapur CR spectrograph [170] (Nandi et al. points on the plot).

Another data points that are shown in Fig. 5.1 are the results of the L3+C (also known as L3+cosmic) experiment [165]. The overview paper [166] does not include the L3+C measure-

ments since they were obtained after the paper had been published. The L3+C results are the most precise measurements of the high-energy muon flux at sea level. The experiment is discussed briefly here below.

The L3 detector was located at the LEP collider experiment at CERN [171]. The experimental points used in this work for the comparison with the CORSIKA simulations are the ones obtained with the upgraded setup of the L3 detector, known as L3+C (or L3+cosmic) [165]. The L3 muon detector is comprised of large drift chambers arranged concentrically around the LEP beam line. The chambers were located inside the 7800-ton magnet providing a 0.5 T field. On top of the detector, outside of the magnet, an array of scintillators for the measurements of the muon arrival time was placed. Above the scintillator array, the shielding of the 30 m stratified rock overburden was used for the absorption of most of the charged air-shower particles other than muons. By subtracting the muon arrival time from the arrival times of the drift electrons at the sense wires, a track position in each chamber could be reconstructed with a precision of about 60 µm in the bending plane and 1 mm in the non-bending plane. The L3+C experiment measured the vertical muon spectrum at sea level up to the momentum of 3 TeV. The average momentum value of the highest momentum bin was estimated to be at 1.6 TeV.

Fig. 5.1 includes also the comparison to two analytical models, Gaisser [1] and Bugaev [172], and to the fit of the MACRO data [60].

The Gaisser model considers the production of muons from the two-body decays of pions and kaons and assumes a primary CR flux of the form $N_0 E^{-\gamma}$, where $N_0 = 1.8$ cm^{-2} sr^{-1} s^{-1} GeV$^{\gamma-1}$ is the normalisation factor and $\gamma = -2.7$ is the spectral index of the CR flux [173]. The Gaisser calculations lead to the following formula for the differential muon spectrum at sea level (the formula is written in a form used in [22]):

$$\frac{dN_\mu}{dE_\mu} = K E_\mu^{-\gamma} \left(\frac{A_\pi}{1 + B_\pi / \epsilon_\pi E_\mu \cos\theta} + \frac{A_K}{1 + B_K / \epsilon_K E_\mu \cos\theta} \right). \tag{5.1}$$

Here, E_μ is the muon energy, K is the normalisation factor, A_π and A_K are the coefficients that depend on the ratio of muons produced by pions and kaons, θ is the muon zenith angle, $\epsilon_\pi = 115$ GeV and $\epsilon_K = 850$ GeV are the pion and kaon decay constants, correspondingly: if the particle energy is $E \gg \epsilon_\pi$ ($E \gg \epsilon_K$) then the pion (kaon) decay process is strongly suppressed with respect to the interaction. This formula is valid when muon decay is negligible ($E_\mu > 100$ GeV) and the curvature of the Earth can be neglected ($\theta < 70°$). Values of the coefficients can be derived from MC computations, numerical approximations or experimental data. Values of these coefficients reported in the original Gaisser work are $KA_\pi = 0.14$ cm^{-2} sr^{-1} s^{-1} GeV^{-1}, $A_K/A_\pi = 0.054$, and $B_\pi = B_K = 1.1$. The Gaisser formula with the aforementioned coefficient values fixed is shown as a red line in Fig. 5.1.

The same formula described above was used in the fit of the MACRO data [60]. The coefficients B_π, B_K, and the ratio A_K/A_π were fixed to the same values as in the Gaisser model. The free parameters of the fit were $A_0 = KA_\pi$ and γ. The MACRO fit result was $A_0 = (0.26 \pm 0.01)$ cm^{-2} sr^{-1} s^{-1} GeV$^{\gamma-1}$ and $\gamma = 2.78 \pm 0.01$. The MACRO fit result without the errors included is shown as a purple line in Fig. 5.1.

The Bugaev model predicts the differential muon flux at sea level as a function of muon momentum, p, for $p > 1$ GeV/c. The calculation of the muon production and propagation through the atmosphere is based on the standard continuous loss approximation [172]. The muon flux is described by the same formula but with different coefficient values for four different momentum ranges. The Bugaev formula for the vertical sea level muon flux is

$$dN_\mu/dp = Cp^{-(\gamma_0+\gamma_1 \log p+\gamma_2 \log^2 p+\gamma_3 \log^3 p)}, \tag{5.2}$$

where C and γ_i $(i = 1, 2, 3)$ are the coefficients whose values for four momentum ranges are reported in Table 5.1. The Bugaev function is plotted as a green line in Fig. 5.1.

Momentum range [GeV/c]	C [cm^{-2} sr^{-1} s^{-1} GeV^{-1}]	γ_0	γ_1	γ_2	γ_3
1 - 9.2765×10^2	2.950×10^{-3}	0.3061	1.2743	-0.2630	0.0252
9.2765×10^2 - 1.5878×10^3	1.781×10^{-2}	1.7910	0.3040	0	0
1.5878×10^3 - 4.1625×10^5	14.35	3.6720	0	0	0
$> 4.1625 \times 10^5$	10^3	4	0	0	0

Table 5.1: Values of parameters used in Eq. 5.2 for the vertical muon energy spectrum at sea level.

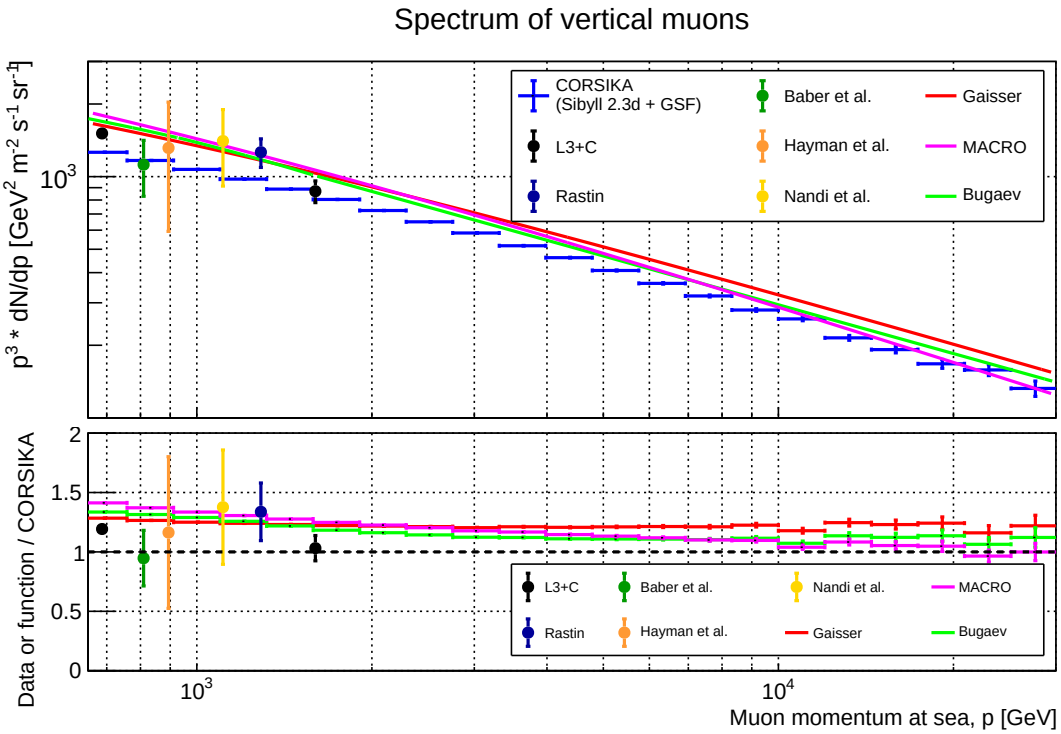

Figure 5.1: The sea level flux of muons as predicted by the CORSIKA simulations used in this work (blue points). The x-axis range covers the 99% fraction of single muon events detected by the ORCA6 and ARCA6 telescopes. The CORSIKA results are compared to two analytical models: the Gaisser model [1] (red line) and the Bugaev model [172] (green line), and to the fit of the MACRO data [60] (purple line). Results from the ground-based experiments shown on the plot are from [165] (black points), [168] (dark blue point), [167] (dark green point), [169] (orange point), and [170] (yellow point).

In general, CORSIKA underestimates the sea level muon flux with respect to both models considered and to the MACRO fit result. The discrepancy is at a level of 30%. The first L3+C

data point and the results from Rastin, Hayman et al., and Nandi et al. are also above the CORSIKA predictions by ∼20-30%. However, the Baber et al. and the second L3+C points are in agreement with the CORSIKA predictions and in disagreement with the models considered.

Given the limited muon momentum resolution, there is no data available from the ground-based experiments for the muon energies above 3 TeV. There are the experimental results of the sea level muon flux also for higher energies but they are based on the underground measurements [174]. The sea level muon flux is unfolded using the underground muon spectrum detected in these experiments. The unfolding is based on the muon survival probability which is derived from MC simulations.

The model used in this work, Sibyll 2.3d with GSF, was also compared to the data from ground-based observatories and to other MC simulations in [175] using the MCEq software [65]. In the official MCEq release, the Sibyll 2.3d and GSF models are not available, the authors of the aforementioned paper modified the MCEq code themselves (one of the authors is also the MCEq developer). The observed discrepancy between the models and the real data is ∼30% (Fig. 5.2), at the same level as the discrepancy between the CORSIKA full MC simulations and the analytical models shown in Fig. 5.1. The BESS results that are shown in Fig. 5.2 are not included in Fig. 5.1 since they lay in the energy range below that of the muons detected in the KM3NeT experiment.

One of the main goals of this chapter is to investigate whether the discrepancy holds also for high-energy muons detected underwater as predicted for muons at sea level or if there is no tension between the KM3NeT data and MC simulations. The answer to this question is provided in Sec 5.5.

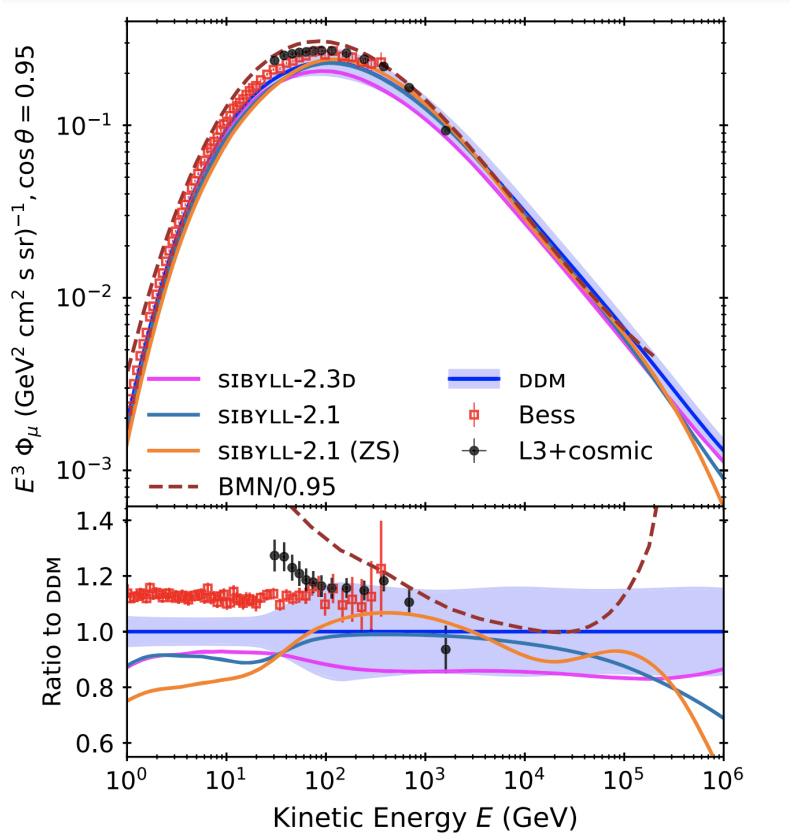

Figure 5.2: Vertical sea level muon spectrum predicted by the MCEq simulations [65] compared with the real data collected by the Bess [176] (red points) and L3+cosmic [165] (black points) experiments. GSF [19] was used as CR mass composition model for the simulations obtained with Sibyll 2.1 [68] (blue line) Sibyll 2.3d [69] (purple line), and DDM [177] (blue line). The Sibyll 2.1 predictions in combination with Zatsepin–Sokolskaya (ZS) primary spectrum [178] are shown as the orange line. Theoretical predictions obtained by Bugaev, Misaki, and Naumov (BMN) [172] are plotted as the brown-dashed line. The bottom plot shows the flux ratio with respect to the DDM model. This figure is taken from [175].

5.2 Selection of the anti-noise cuts

In the data collected by the KM3NeT telescopes, there are events that are not included in the atmospheric muon simulations. These events are pure background noise which includes the decays of ^{40}K and the light from bioluminescence [153]. They are usually characterized by a number of PMT hits that is less than the one for the atmospheric muon events. A definition of the PMT hit may be found in Chapter 2. Also, the value of reconstruction likelihood (Chapter 3) for the background noise is usually lower. Hence, in order to exclude such events from the data, cuts on the likelihood, L, and the number of PMT hits, n_{hits}, were applied. The L and n_{hits} distributions from the data and MC produced without the cuts are presented in Fig. 5.3 for ORCA6 and in Fig. 5.5 for ARCA6. The cuts were determined in a way to remove regions where visually MC lacks events, the data/MC ratio behaves differently compared to the rest of the parameter space. Based on the distributions shown in Fig. 5.3 and Fig. 5.5, the same

cuts were chosen for the ORCA6 and ARCA6 detectors: $L > 50$ and $n_{\text{hits}} > 20$. The same distributions after applying the cuts are shown in Fig. 5.4 and Fig. 5.6.

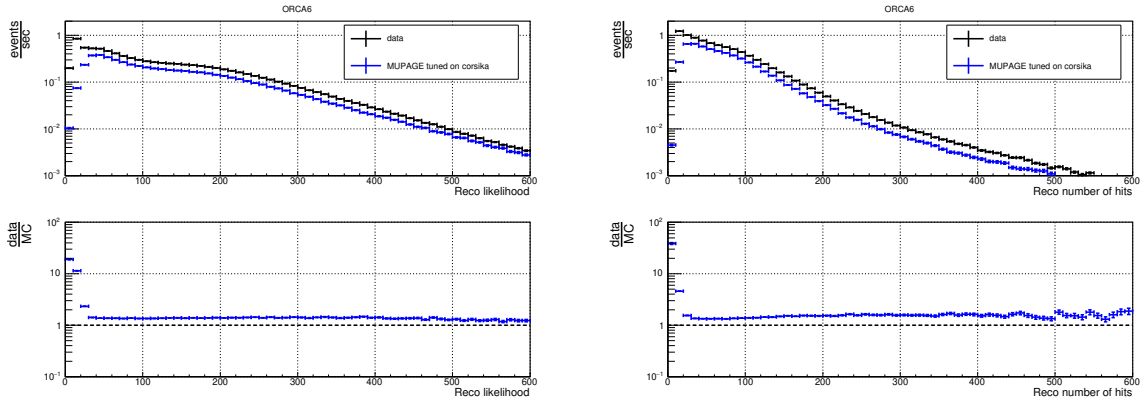

Figure 5.3: The data (black points) and MC simulation (blue points) distributions for the likelihood (left plot) and the number of hits (right plot) produced without any cuts applied for the ORCA6 detector. The bottom plot shows the data/MC ratio.

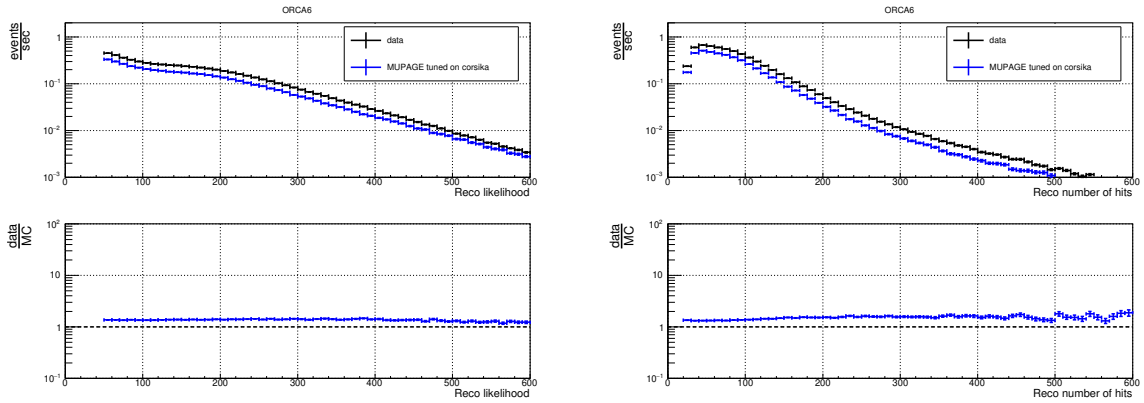

Figure 5.4: Comparison between the data (black points) and MC (blue points) in terms of the likelihood (left plot) and the number of hits (right plot) for the ORCA6 detector after applying the anti-noise cuts, $L > 50$ and $n_{\text{hits}} > 20$. The ratio between the data and simulations is presented on the bottom plot.

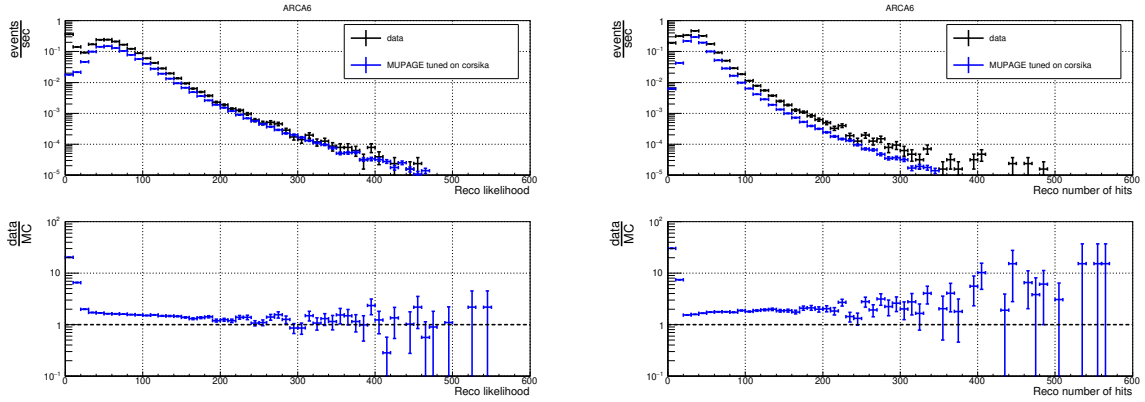

Figure 5.5: Reconstructed likelihood (left plot) and the number of hits (right plot) distributions obtained for the ARCA6 telescope. No cuts were applied here. The black points demonstrate the data while the blue ones are for the simulations. The data/MC ratio is on the bottom plot.

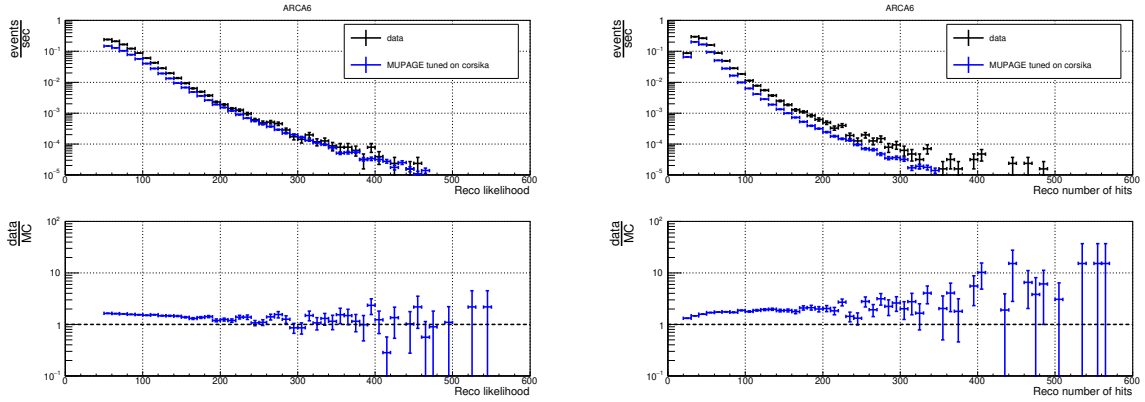

Figure 5.6: Results of the application of the cuts ($L > 50$ and $n_{\text{hits}} > 20$) on the ARCA6 data (black points) and simulations (blue points). The likelihood distribution is shown on the left and the number of hits one is on the right. The bottom plots show the data/MC ratio after applying the cuts.

In general, the cuts might introduce a discrepancy between the MUPAGE tuned on CORSIKA and the CORSIKA simulations. In order to check if the MUPAGE and CORSIKA agreement holds after applying the cuts, the same comparisons as discussed in Chapter 4 were repeated choosing only the events with $L > 50$ and $n_{\text{hits}} > 20$. The results are presented in Fig. 5.7 (ORCA6) and Fig. 5.8 (ARCA6). MUPAGE still agrees well with the CORSIKA results. The plots demonstrate the zenith distributions solely since these are the only distributions that were used for the final results as described below in Sec. 5.3.

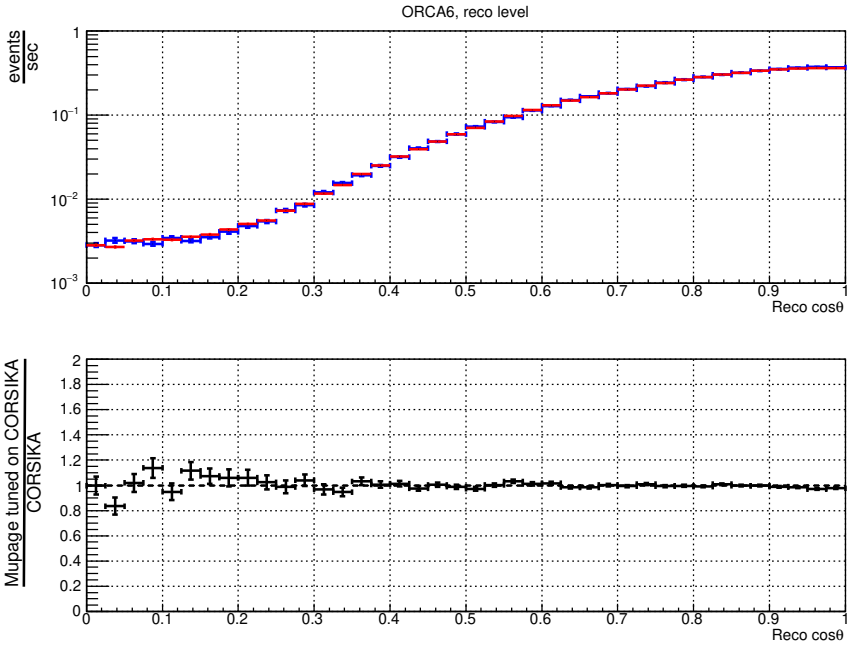

Figure 5.7: Comparison of the CORSIKA simulation results (blue points) with the MUPAGE tuned on that simulation (red points) after applying the cuts, $L > 50$ and $n_{\text{hits}} > 20$, for the ORCA6 detector. The bottom plot shows the ratio between the MUPAGE tuned on CORSIKA and the CORSIKA simulations.

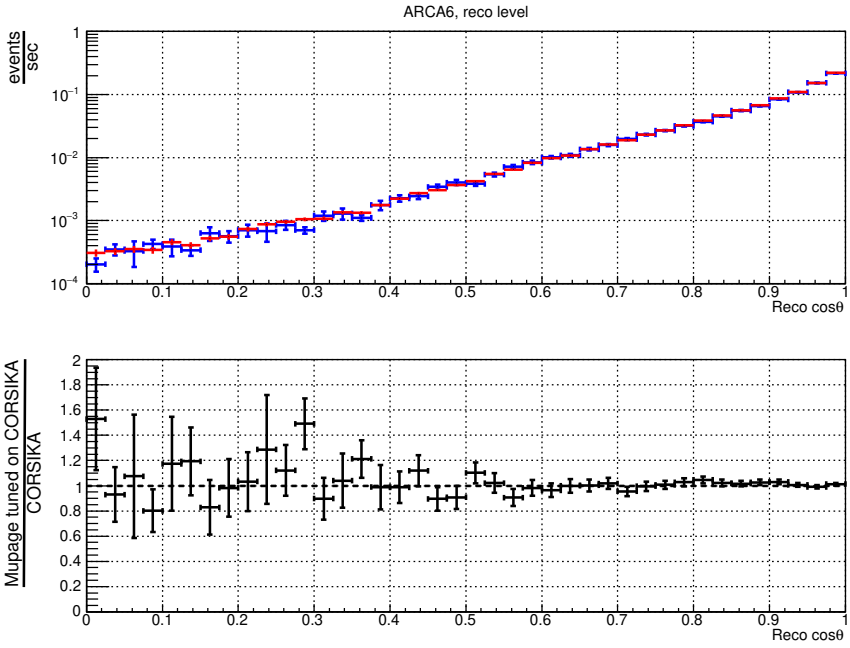

Figure 5.8: Agreement between the CORSIKA (blue points) and MUPAGE (red points) zenith distributions for ARCA6 after applying the cuts. The tuned MUPAGE over CORSIKA ratio is on the bottom plot.

5.3 Muon reconstruction performance

This section describes the performance of the reconstruction algorithms which aim to estimate the muon direction and energy. The performance estimation is needed to choose only the parameter regions with well-reconstructed muon properties. The reconstruction algorithms are described in Chapter 3.

5.3.1 Direction reconstruction

To evaluate the direction reconstruction capabilities, the true and reconstructed muon zenith angles, θ, were used. The true zenith angle is the one of the muon bundle on the detector can, all the muons are assumed to be collinear with the bundle axis in MUPAGE. The reconstructed angle is instead obtained from the JMuon algorithm described in Chapter 3. Fig. 5.9 compares the MC true $\cos\theta$ distribution (blue points) with the reconstructed one (red points) for the ORCA6 detector. The discrepancy starts to emerge for events with $\cos\theta < 0.5$. The reason for this discrepancy is that the flux dependence on the true $\cos\theta$ is very steep and few well-reconstructed events at $\cos\theta < 0.5$ are dominated by a fraction of mis-reconstructed vertical muons. The KM3NeT angular resolution is at sub-degree level, so the fraction of mis-reconstructed events is small, however the number of vertical muons is several orders of magnitude higher. Hence, it was decided to use only muons with $\cos\theta > 0.5$ for the final data/MC studies. The same plot but for the ARCA6 telescope is shown in Fig. 5.10. Well-reconstructed muons are those with $\cos\theta > 0.6$.

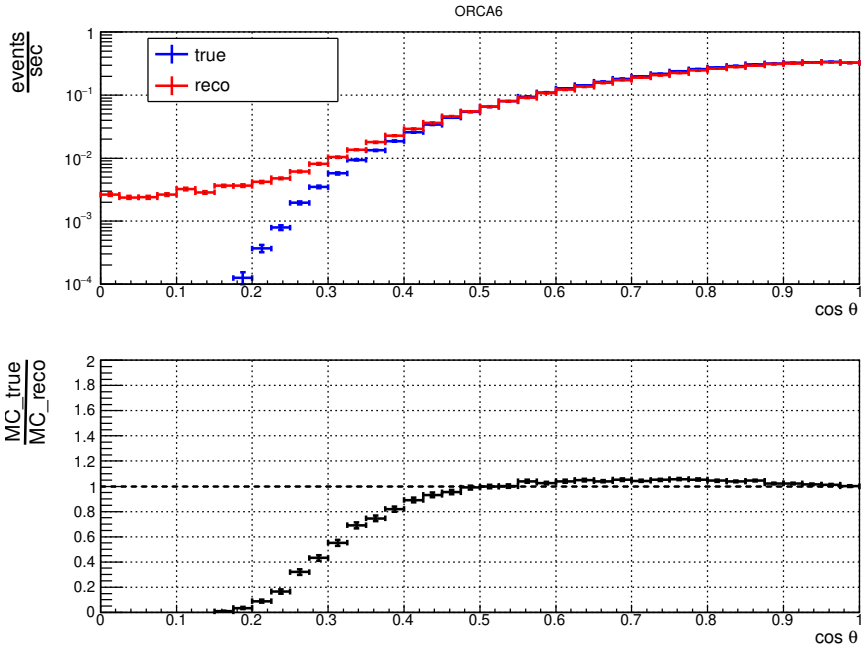

Figure 5.9: Distribution of the muon bundle zenith angle on the can ("true" in the legend, blue points) compared to the reconstructed zenith angle obtained with the JMuon algorithm ("reco" in the legend, red points) for the ORCA6 detector. The well-reconstructed muons are those with $\cos\theta > 0.5$. The bottom plot shows the ratio of the distributions.

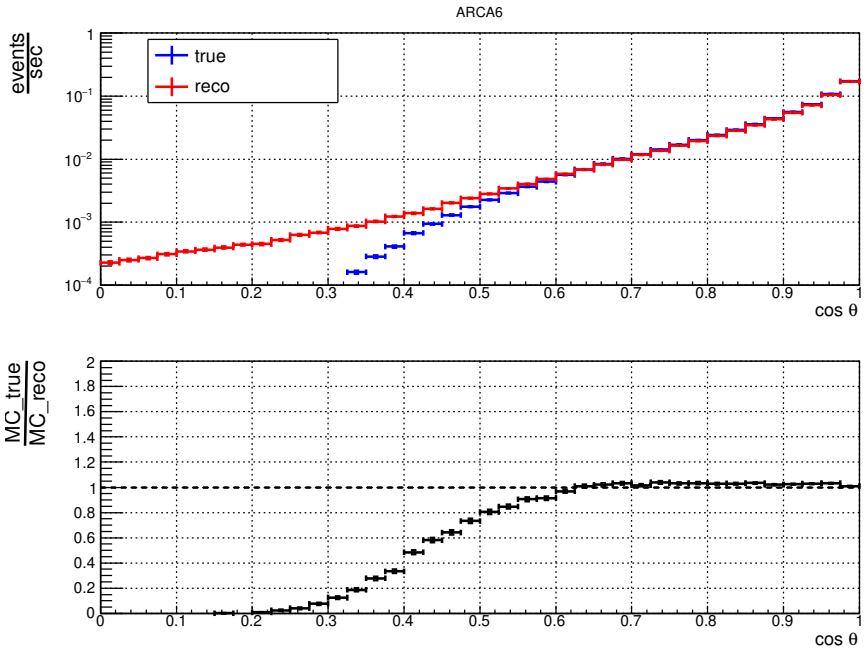

Figure 5.10: The zenith angle reconstruction performance for the ARCA6 detector. The well-reconstructed region is $0.6 < \cos\theta < 1$. The definitions of the "true" and "reco" events are reported in the text.

5.3.2 Energy reconstruction

Estimation of the energy reconstruction performance is less straightforward since there is no direct access to the true muon energy. In the MC files, there is the reconstructed energy and the true energy of muons on the can. The reconstructed energy is the one that the muon had at the position where the first light seen by PMTs was emitted. Hence, the comparison of the reconstructed energy with the true energy on the can is not appropriate since the particles have lost part of their energy while traveling in water between the point on the can and the point where the first detected light was emitted. Thus, the muon energy on the can has to be corrected (decreased) using the distance between the two aforementioned points in order to get the estimation of the true muon energy. This re-calculation was performed using the Klimushin, Bugaev, Sokalski parameterization [133] that describes the muon energy losses in water.

Results for the ORCA6 detector are presented in Fig. 5.11. Since the JMuon algorithm reconstructs the muon bundle as one particle, only muon bundles containing one muon were used in the plot. The reconstructed energy is shown in red, the muon energy on the can is in green, and the corrected (re-calculated) one is in blue. The reconstructed and corrected energy starts to agree for high-energy muons with $E > 10$ TeV, while for lower-energy particles the discrepancy is large. Fig. 5.12 demonstrates the energy reconstruction performance for the ARCA6 detector. The disagreement is substantial in the whole energy range.

Due to the disagreement of the reconstructed energy with respect to the true energy, only zenith distributions in the well-reconstructed $\cos\theta$ ranges were used for the final analysis.

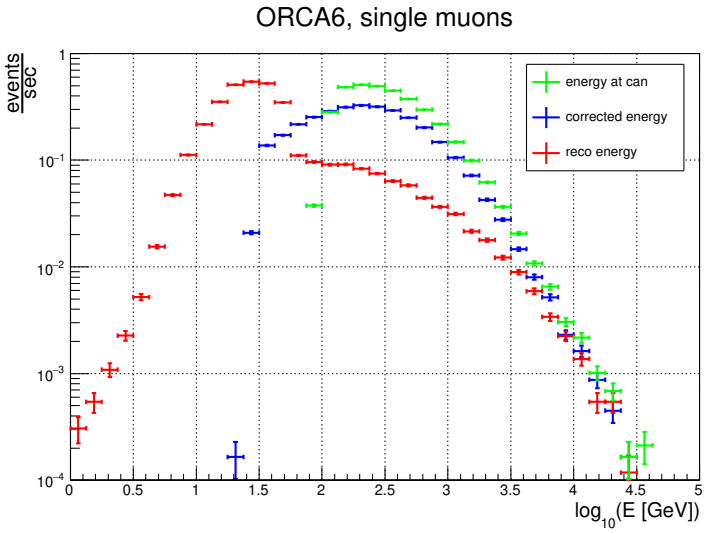

Figure 5.11: Estimation of the JMuon algorithm performance for the single muon energy reconstruction. The reconstructed energy is shown as red points, the energy of single muons on the can is in green, and the re-calculated energy is in blue.

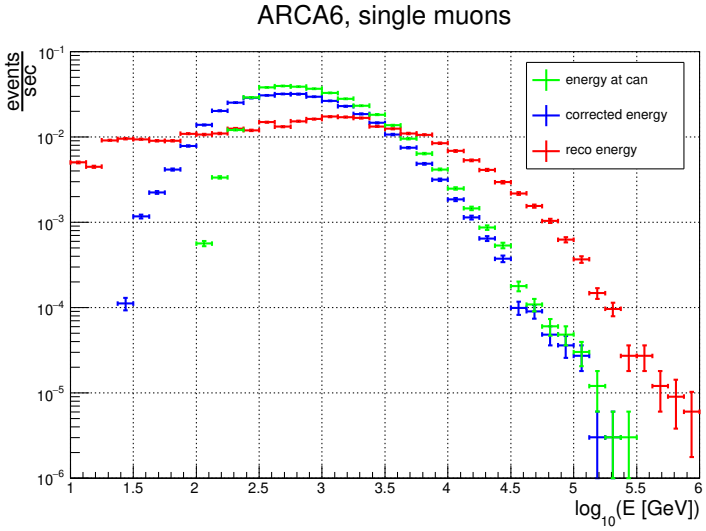

Figure 5.12: The single muon energy reconstructed with the ARCA6 detector (red points) compared with the muon energy on the can (green points) and the re-calculated muon energy (blue points).

The different shapes of the reconstructed energy distributions for the ORCA6 and ARCA6 telescopes may be explained by the different detector geometries.

For muon energies below 100 GeV, the muon energy losses are almost proportional to the travelled distance (∼0.25 GeV per meter) so muon behaves as a minimum ionizing particle [133]. For 100 GeV muon, the track length is about 400 m which is actually longer than the sensitive size of the ORCA detector especially considering slightly inclined muons that do not pass through the whole vertical length of the detector which is ∼300m. So even for perfectly working

reconstruction algorithms, muons with energies of 100 GeV are in the "gray" zone where it is not possible to properly measure their energies with ORCA.

For the ARCA6 detector, muons below 100 GeV are almost never reconstructed due to the sparser module distribution with respect to ORCA. For muons above 100 GeV, the contribution of the radiation losses becomes important and, thus, the energy reconstruction can be performed by measuring the muon energy losses per unit length (dE/dx) which becomes roughly proportional to the muon energy.

The detector configurations that were used in this work include 6 DUs (see Chapter 2 for the DU definition) for the ORCA and ARCA telescopes. The reconstruction performance is expected to improve for larger detectors.

5.4 Systematic uncertainties estimation

Systematic uncertainties considered in this work include that on the CR flux (Sec. 5.4.1), the light absorption length in seawater (Sec. 5.4.2), the PMT quantum efficiency (Sec 5.4.3), and the high-energy hadronic interaction model (Sec. 5.4.4). The CR flux uncertainties were estimated using the CORSIKA full MC simulations. All the other uncertainties mentioned were evaluated with the MUPAGE tuned on CORSIKA.

5.4.1 Cosimc Ray flux uncertainty

As it is described in Chapter 3, GSF [19] was chosen as the model for the CR flux. This model includes the uncertainty on the total flux as a function of primary energy which is used for the systematics studies described below.

Additionally, the GSF model provides the uncertainty on each of the four so-called mass groups which was also considered in this analysis. The groups are split in roughly equal ranges in logarithmic mass. The mass groups description is reported in Chapter 3.

Finally, since there are 5 primaries simulated in CORSIKA (p, He, C, O, and Fe) and 28 primaries available in the GSF model, the following approach was used to include all the nuclei available in GSF. The proton and helium flux weights, $w^{\mathrm{p}}_{\mathrm{CR}}$ and $w^{\mathrm{He}}_{\mathrm{CR}}$, are taken directly from the GSF table containing the flux values for each nucleus. The carbon $w^{\mathrm{C}}_{\mathrm{CR}}$ weight is the sum of the GSF weights of nuclei with Z from 3 to 6, $w^{\mathrm{C}}_{\mathrm{CR}} = \sum_{Z=3}^{6} w^{Z}_{\mathrm{CR}}$, the oxygen weight is $w^{\mathrm{O}}_{\mathrm{CR}} = \sum_{Z=7}^{10} w^{Z}_{\mathrm{CR}}$, and the iron weight is $w^{\mathrm{Fe}}_{\mathrm{CR}} = \sum_{Z=11}^{28} w^{Z}_{\mathrm{CR}}$. In principle, this weight assignment to C, O, and Fe is arbitrary. The uncertainty induced by the different assignments is studied in the last part of this section.

Total flux

The total flux uncertainty calculation was performed using the limits on the all-particle flux available in the GSF model and keeping the CR composition unchanged. In order to incorporate these limits into the CORSIKA simulations, the composition weights were rescaled so that the sum of the weights is equal to the corresponding flux limit, lower and upper.

Results of the total flux uncertainty estimation are presented in Fig. 5.13 (the left plot is for ORCA6, and the right plot is for ARCA6). The blue points on the plots correspond to the results obtained with the average total flux, the red points were obtained for the lower limit, and the purple ones show the results for the upper limit.

The relative uncertainties were fitted with inclined lines. The results of the fit are presented in Fig. 5.14. The relative uncertainty is at a level of 6-8%.

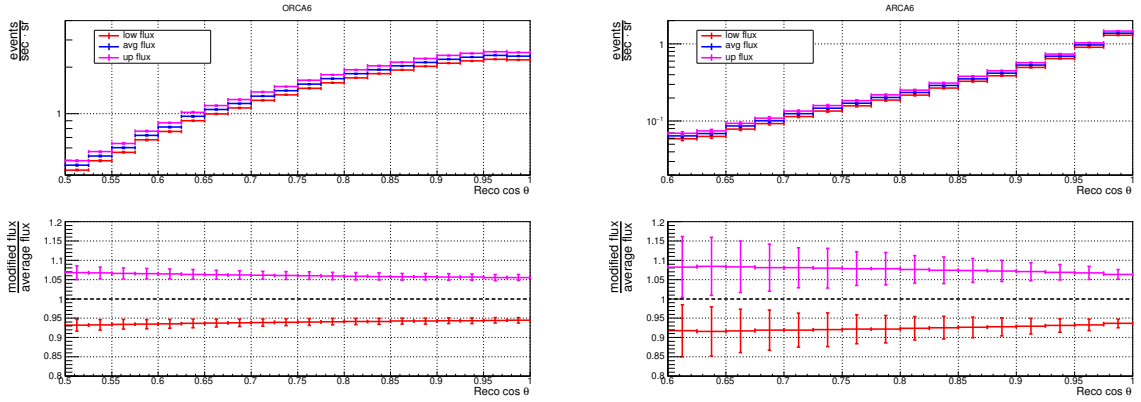

Figure 5.13: Estimation of the systematic uncertainty on the total CR flux taken from the GSF model. The results with the average flux are shown in blue, the lower (upper) flux limit is the red (purple) points.

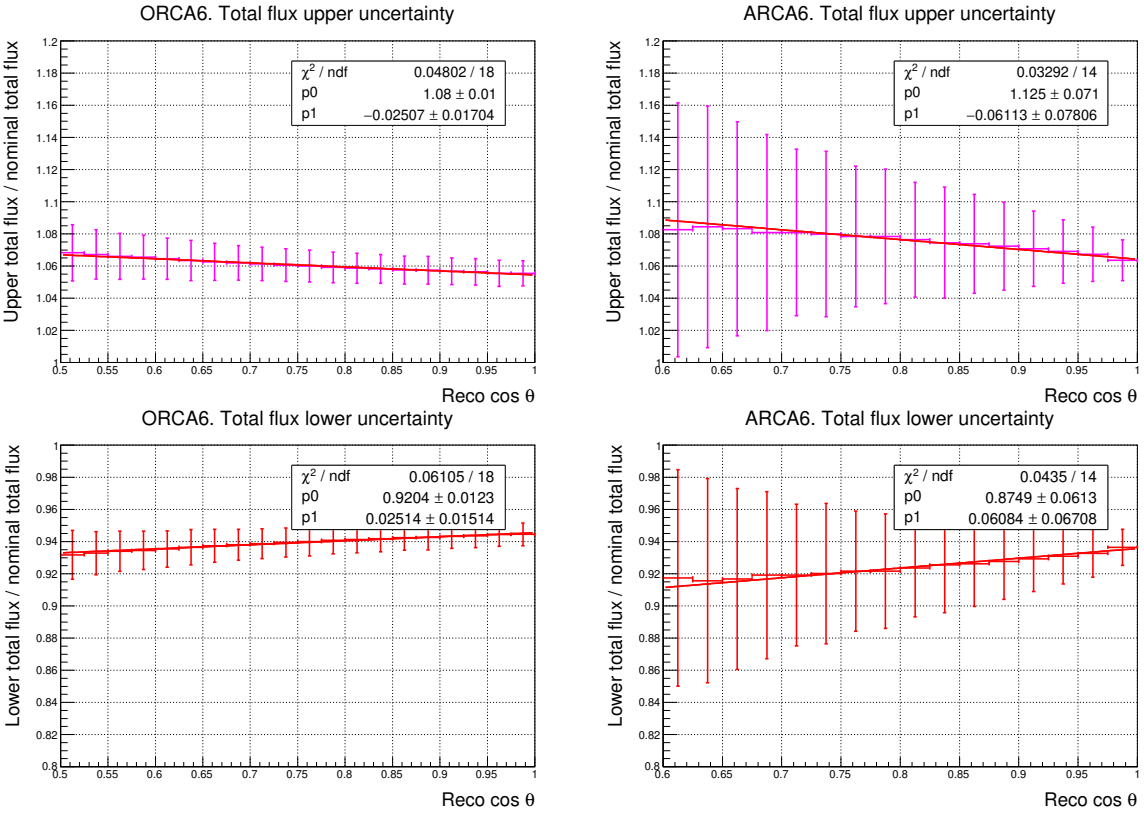

Figure 5.14: Fit of the ratio of the simulation results obtained with modified total flux with respect to the average flux. The left (right) top plot shows the fit result for the ORCA6 (ARCA6) upper uncertainty. The lower uncertainty fit results are presented on the bottom plots.

Uncertainty on the CR composition

The uncertainties on the CR composition were also calculated using the ranges on the fluxes

for each mass group in the GSF model. In practice, the light (proton) and heavy (iron) components of the flux were varied within their uncertainties while keeping the total flux value unchanged. At first, the proton flux was assigned to its maximum value within uncertainty. Fluxes of other primaries were recalculated, starting from iron, in order to have the same average value of the total flux. Then, the same procedure was repeated but with the iron flux enlarged and other primary fluxes decreased. The results of this uncertainty calculation are at a level of 6-7%, the left plot on Fig. 5.15 is for ORCA6 and the right one is for ARCA6.

In order to get the function that describes these uncertainties, the latter were fitted with inclined lines. The fit results are in Fig. 5.16.

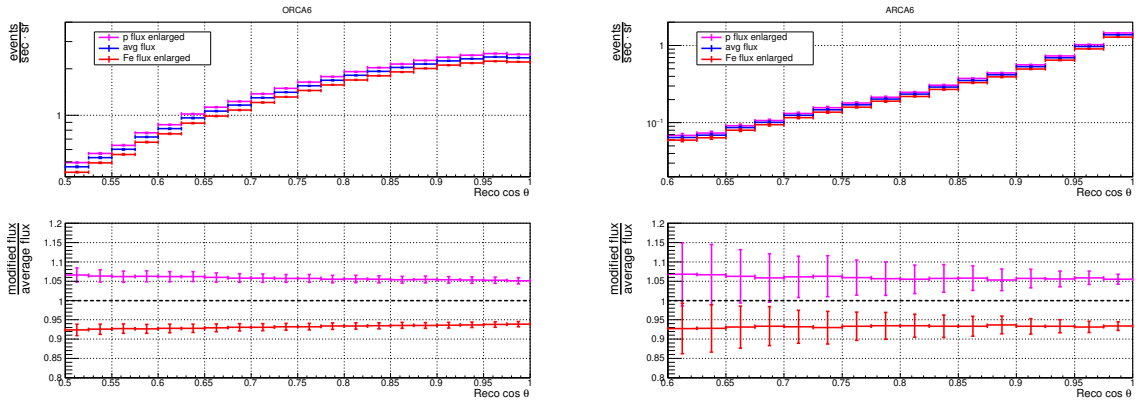

Figure 5.15: The zenith distribution obtained with the average CR flux (blue points) and the maximum proton flux (purple points) and iron flux (red points) within their uncertainties while keeping the total flux unchanged. The left plot represents the ORCA6 results, the right one is for the ARCA6 detector.

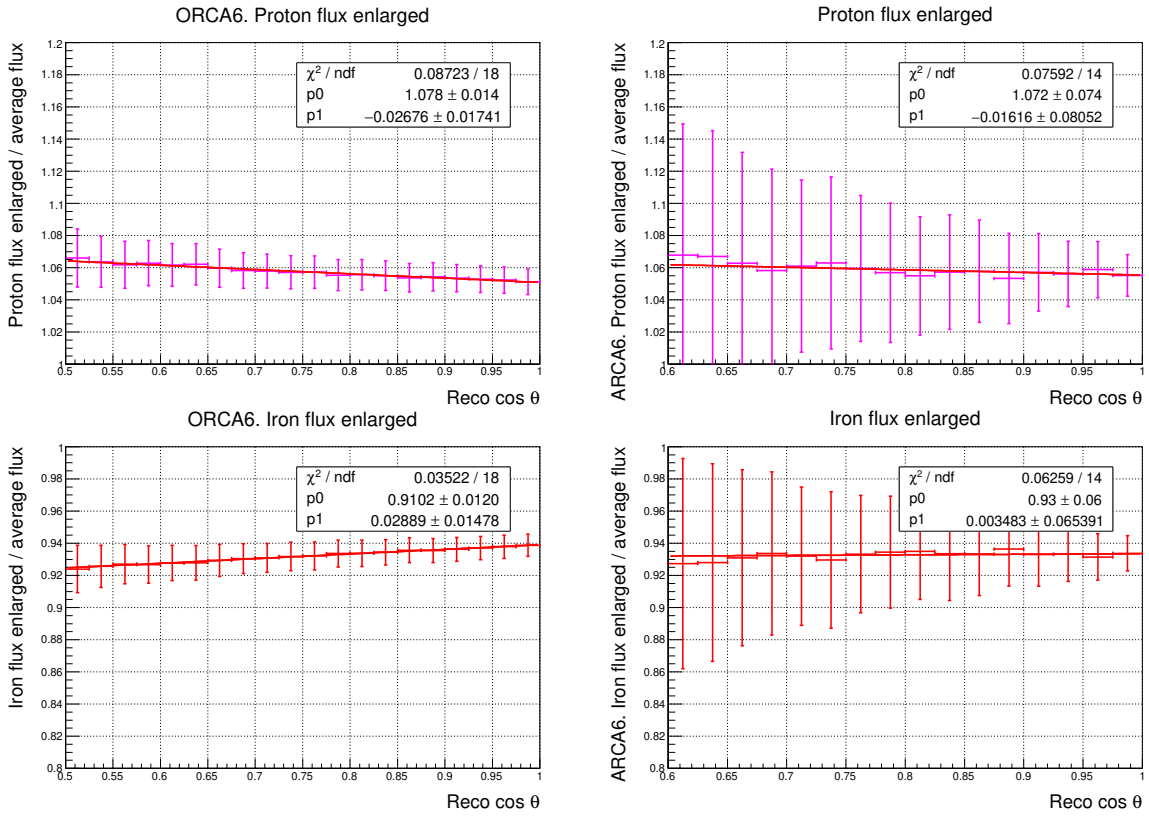

Figure 5.16: Uncertainty induced by varying the proton and iron flux weights fitted with inclined lines. The ORCA6 fit results are shown on the left part of the figure; upper uncertainty is on the top, and lower uncertainty is on the bottom. The right part demonstrates the ARCA6 fit results.

Flux weight assignment

In order to have the average CR flux, the weight assignments to C, O, and Fe were $w^{\mathrm{C}}_{\mathrm{CR}} = \sum_{Z=3}^{6} w^{Z}_{\mathrm{CR}}$, $w^{\mathrm{O}}_{\mathrm{CR}} = \sum_{Z=7}^{10} w^{Z}_{\mathrm{CR}}$, and $w^{\mathrm{Fe}}_{\mathrm{CR}} = \sum_{Z=11}^{28} w^{Z}_{\mathrm{CR}}$ correspondingly, as described above. A test was performed in order to estimate the bias introduced by that particular weight assignment. The two edge cases were considered. The first one was to assign larger weights to lighter primaries, "weights towards lighter primaries" on Fig. 5.17, and the second one was to enlarge the weights of the heavier primaries, "weights towards heavier primaries" on the same figure below. In the first case, the following weight assignment was chosen: $w^{\mathrm{p}}_{\mathrm{CR}} = w^{Z=1}_{\mathrm{CR}}$, $w^{\mathrm{He}}_{\mathrm{CR}} = \sum_{Z=2}^{5} w^{Z}_{\mathrm{CR}}$, $w^{\mathrm{C}}_{\mathrm{CR}} = \sum_{Z=6}^{7} w^{Z}_{\mathrm{CR}}$, $w^{\mathrm{O}}_{\mathrm{CR}} = \sum_{Z=8}^{25} w^{Z}_{\mathrm{CR}}$, and $w^{\mathrm{Fe}}_{\mathrm{CR}} = \sum_{Z=26}^{28} w^{Z}_{\mathrm{CR}}$. The weight towards heavier primaries scheme implies $w^{\mathrm{p}}_{\mathrm{CR}} = w^{Z=1}_{\mathrm{CR}}$, $w^{\mathrm{He}}_{\mathrm{CR}} = w^{Z=2}_{\mathrm{CR}}$, $w^{\mathrm{C}}_{\mathrm{CR}} = \sum_{Z=3}^{6} w^{Z}_{\mathrm{CR}}$, $w^{\mathrm{O}}_{\mathrm{CR}} = \sum_{Z=7}^{8} w^{Z}_{\mathrm{CR}}$, and $w^{\mathrm{Fe}}_{\mathrm{CR}} = \sum_{Z=9}^{28} w^{Z}_{\mathrm{CR}}$.

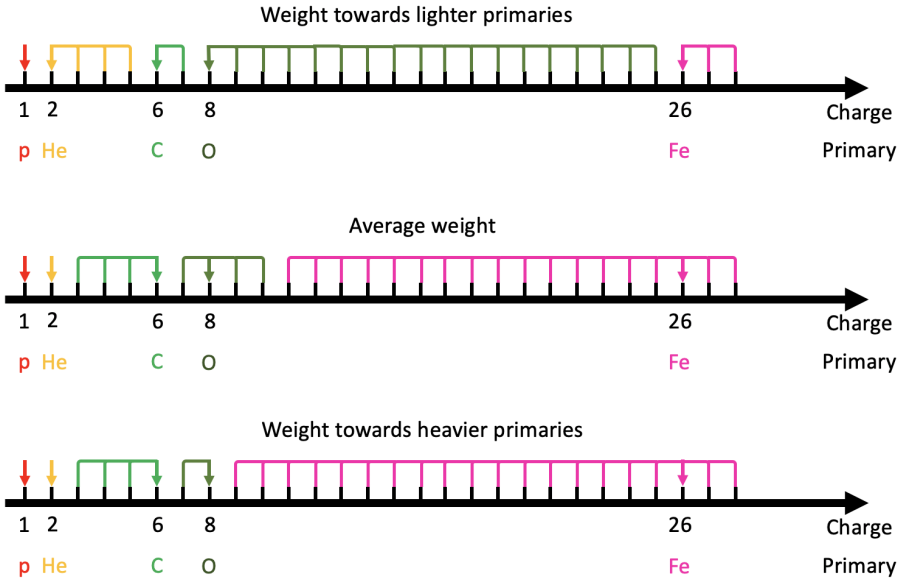

Figure 5.17: Scheme of the CR flux weight assignment.

The upper uncertainty due to the different scheme of the flux weight assignment is 3% and the lower one is 0.5% for both the ORCA6 (left part of Fig. 5.18) and the ARCA6 (right part of Fig. 5.18) detectors. The fit of the uncertainties is presented in Fig. 5.19.

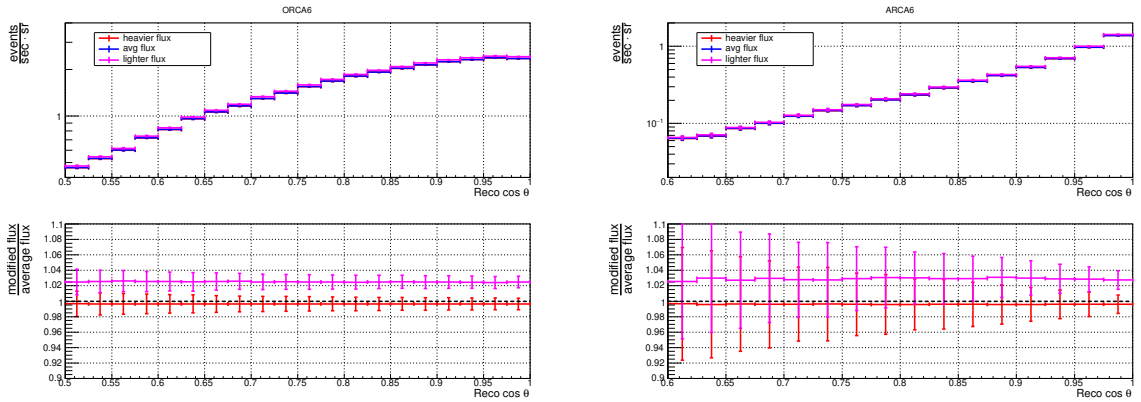

Figure 5.18: Uncertainty induced by the different primary weighting schemes. The average flux is shown in blue, the purple points represent the flux towards lighter primaries, and the red points represent the flux towards heavier primaries. The results for the ORCA6 detector are on the left plot, the ARCA6 results are on the right one.

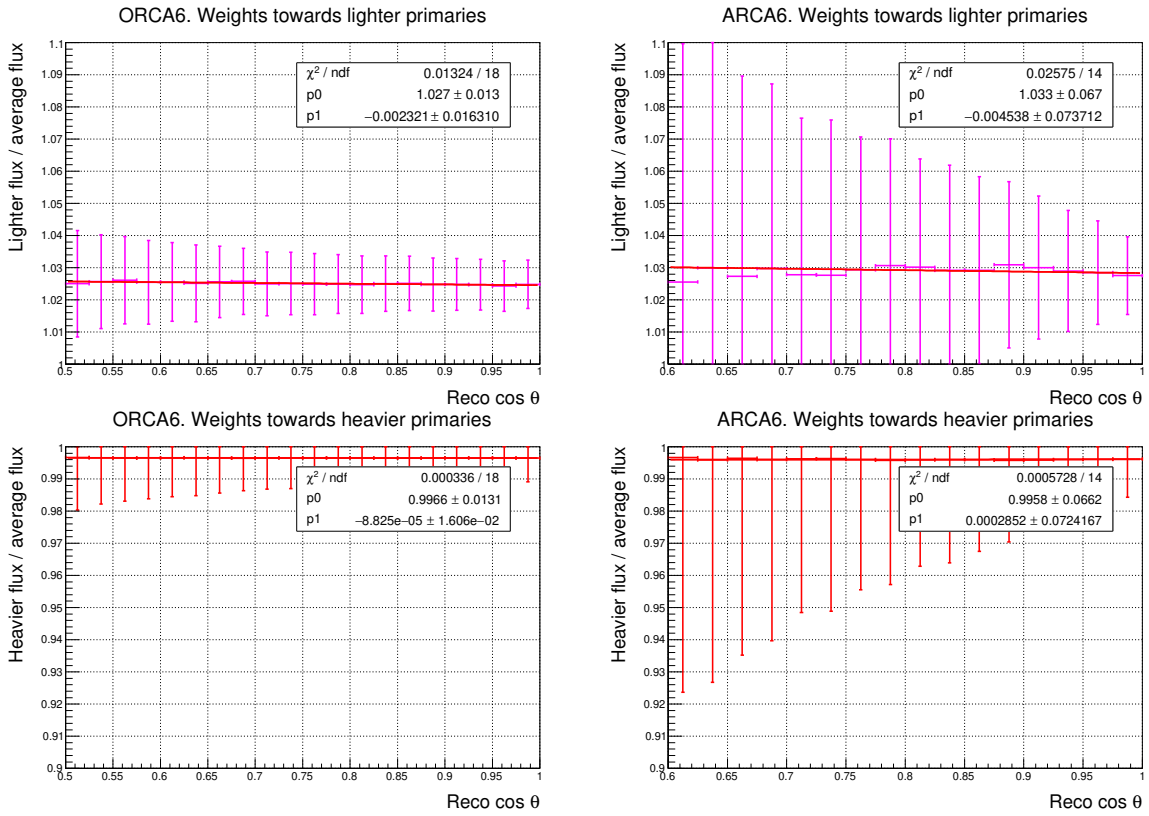

Figure 5.19: The ORCA6 (left) and the ARCA6 (right) flux assignment uncertainties fitted with inclined lines. The top part of the figure illustrates the upper uncertainties fit, the bottom part is for the fit results of the lower uncertainties.

5.4.2 Light absorption length in seawater

As discussed in Chapter 3, the light absorption length that is used in the KM3NeT simulations is the result of the measurements of the NEMO Collaboration at the "KM4" site [148]. They reported the variation of the light absorption length in time at a level of ±10% for 400-500 nm wavelength.

In order to estimate the effect of the uncertainty known from the measurements of light absorption length on the final simulation results, the MC simulations with two modified absorption lengths (increased and decreased by 10%) were performed. Then, the ratios between the MC simulations with the standard absorption length and with the modified ones were obtained.

Fig. 5.20 left (right) illustrates the result for the ORCA6 (ARCA6) telescope. The ORCA6 uncertainty is 5%, while the ARCA6 one is 10-20%. The difference in the uncertainty values is due to the different detector geometries, the ORCA6 detector layout is denser and light travels less path in water with respect to the ARCA6 telescope. Hence, the influence of different absorption length values is less pronounced in ORCA6.

To obtain the function that describes the uncertainty on the light absorption length, the ORCA6 relative uncertainties were fitted with straight lines while the ARCA6 ones, $\sigma(\cos\theta)$, were fitted with the following custom function:

$$\sigma(\cos\theta) = \frac{p_0}{e^{(\cos\theta - p_1)*p_2} + 1}, \tag{5.3}$$

where p_0, p_1, and p_2 are free parameters. The fit results are in Fig. 5.21.

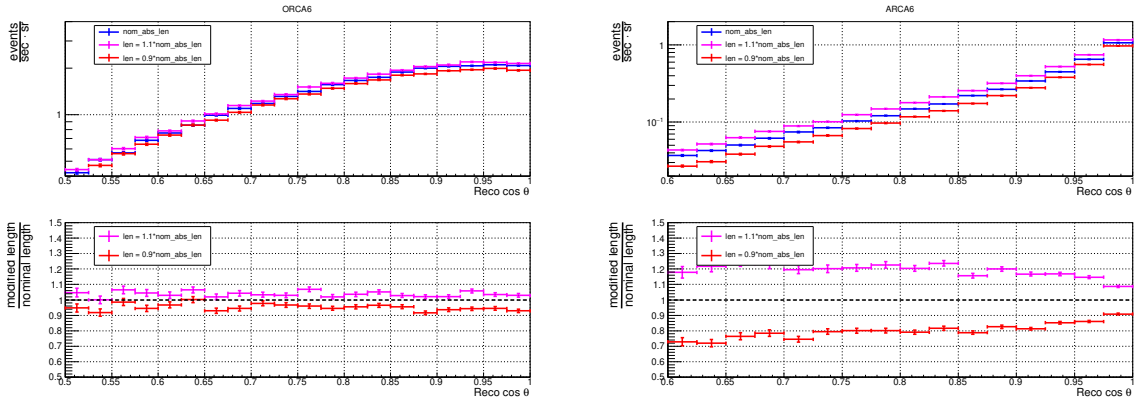

Figure 5.20: Systematic uncertainty due to the measurements of the light absorption length in seawater for the ORCA6 (left) and ARCA6 (right) detectors. The blue points demonstrate the MC simulation results obtained with the nominal value of the absorption length. The red (purple) points represent the results obtained with the absorption length decreased (increased) by 10%.

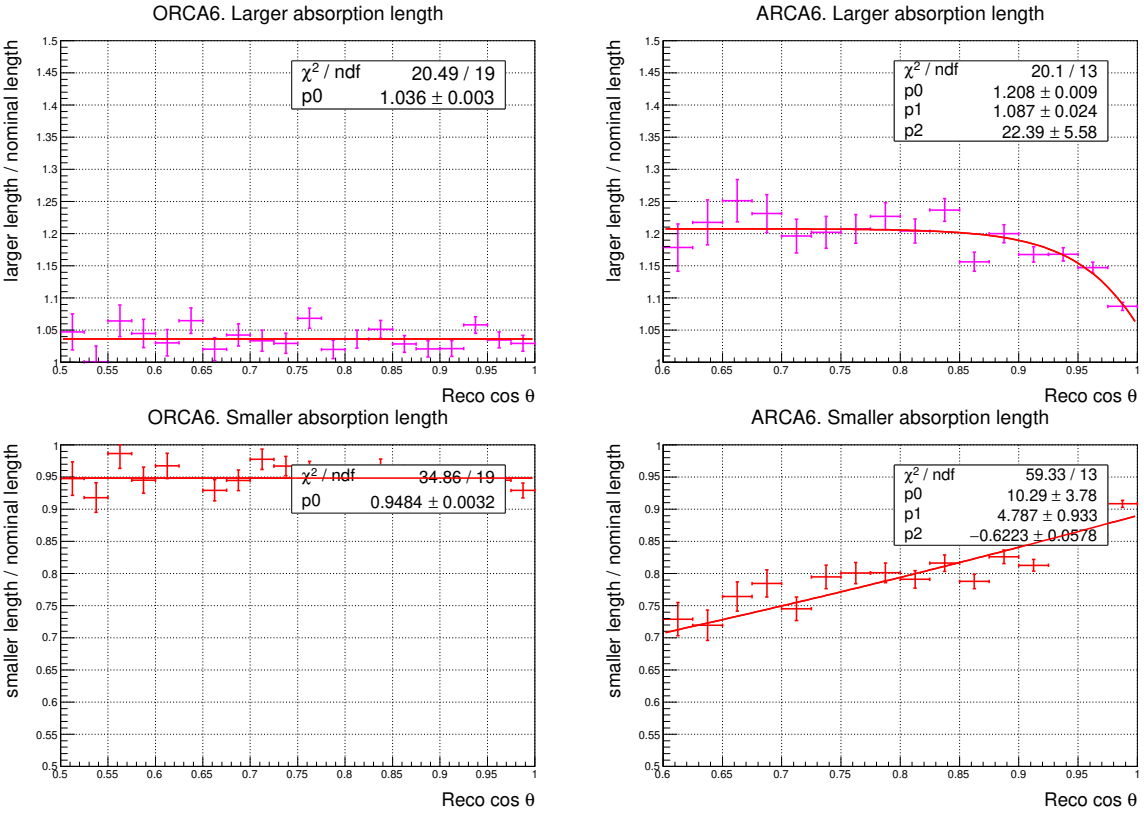

Figure 5.21: The ratio between the MC simulation results with the modified absorption length and with the nominal one. The left (right) top part of the figure shows the fit of the ratio that evaluates the upper uncertainty for the ORCA6 (ARCA6) telescope. The left (right) bottom part corresponds to the ORCA6 (ARCA6) lower uncertainty fit.

5.4.3 PMT efficiency values

Values of the quantum efficiencies of the KM3NeT PMTs are believed to be known with 10% precision. The MC simulations were repeated with the PMT efficiency values increased and decreased by 10% for the evaluation of the corresponding systematics. The simulation results with the modified values of PMT efficiencies together with the nominal simulations are presented in Fig. 5.22. The discrepancy is 5% for ORCA6 and 10-30% for ARCA6. Also in this case, the larger uncertainties for the ARCA6 telescope can be explained by its geometry, i.e. spatial distribution of DOMs in ARCA is less dense than in ORCA.

The uncertainties were fitted with the same functions as described above in the systematics evaluation induced by the light absorption length, see Fig. 5.23 for the results.

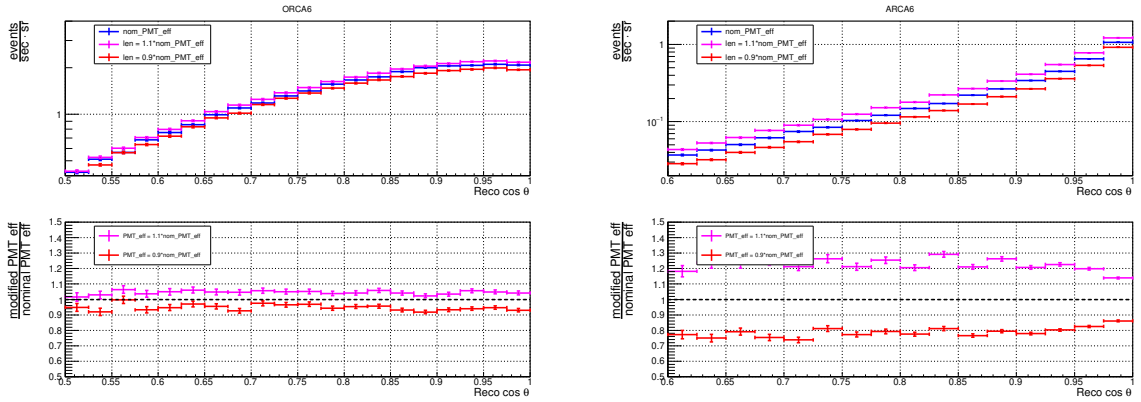

Figure 5.22: The zenith angle distribution of muons obtained with the MC simulations using the modified values of PMT efficiency (the red points - efficiency decreased by 10%, the purple points - increased by 10%) and with the nominal simulations (blue points). The left plot is for ORCA6, and the right one is for ARCA6.

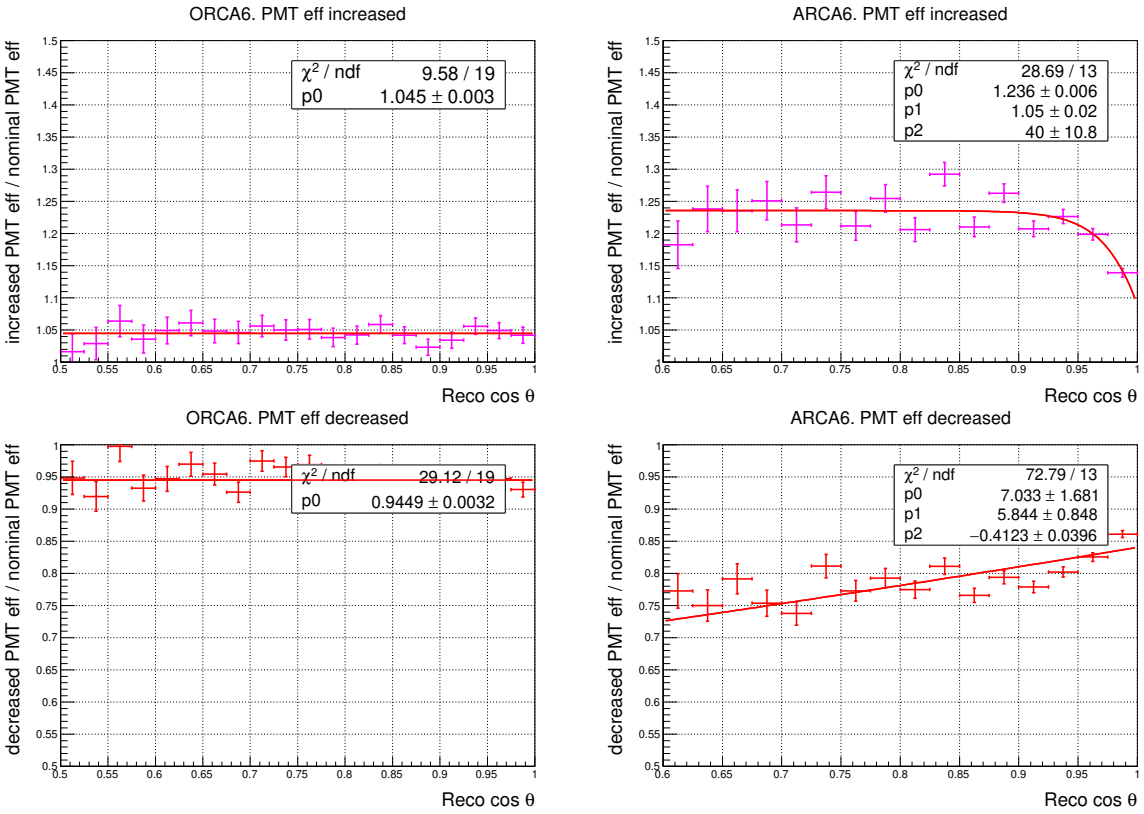

Figure 5.23: Fit results of the ORCA6 and ARCA6 relative uncertainties on the PMT efficiency values, the left and right parts of the figure correspondingly. The top (bottom) part is for the upper (lower) uncertainty.

5.4.4 Hadronic interaction model

The uncertainty induced by the differences in the high-energy hadronic interaction models was estimated using the MCEq software [65]. The program provides the flux of muons at sea level given the hadronic interaction model. Three post-LHC models were used for the muon flux calculation, namely EPOS-LHC [71], QGSJETII-04 [70], and Sibyll 2.3c [179]. The CORSIKA simulation results were obtained with the Sibyll 2.3d [69] model for the interactions. This model is not present in the MCEq, the latest Sibyll version available is 2.3c. Hence, Sibyll 2.3c was used for the uncertainty estimation.

The relative lower and upper uncertainties as a function of the muon energy at the sea level are plotted in Fig. 5.24. The lower (upper) uncertainty was calculated as the ratio between the hadronic interaction model that provides the maximum (minimum) flux value for the certain muon energy with respect to the flux value averaged over the results obtained with the three models considered.

To evaluate the uncertainty for the KM3NeT simulation results, the flux of muons that reach the ORCA6 and ARCA6 detector cans as a function of their energy at sea level was used. Fig. 5.25 demonstrates such fluxes for the ORCA6 (left plot) and the ARCA6 (right plot) detectors. The uncertainty value was obtained by convolution of the results in Fig. 5.24 with the muon fluxes plotted in Fig. 5.25. The lower and upper uncertainties for the ORCA6 (ARCA6) detector are at a level of 3% (4%).

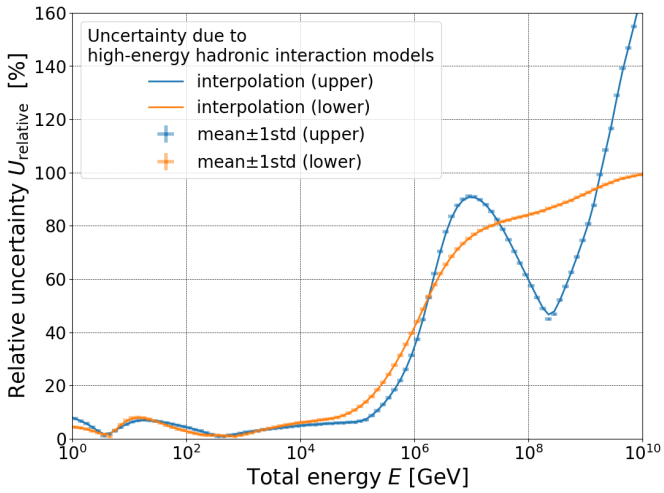

Figure 5.24: Estimation of the systematic uncertainty on the hadronic interaction models. The plot demonstrates the relative lower and upper uncertainties as a function of muon energy at sea level.

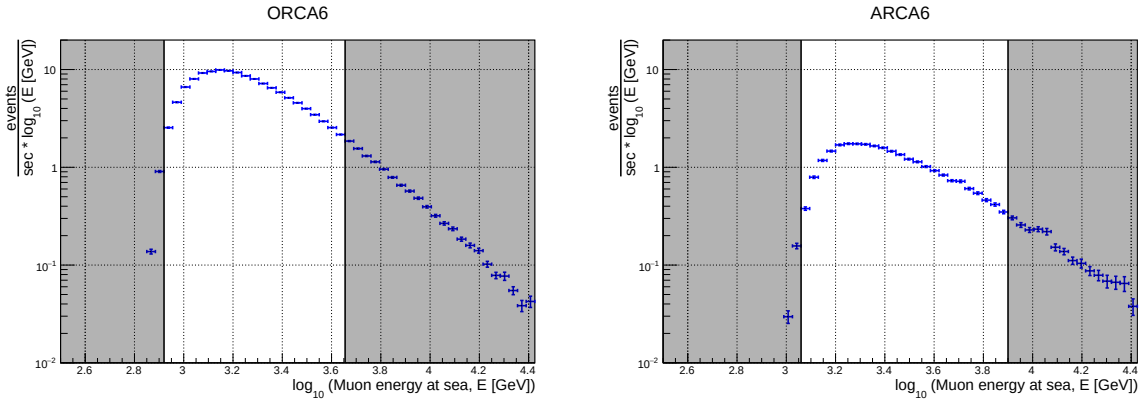

Figure 5.25: Flux of the atmospheric muons that reach the ORCA6 (left plot) and the ARCA6 (right plot) detector cans as a function of their energy at sea level. The highlighted area indicates the 90% fraction of events counting from the maximum of the distribution, 0.8-4.5 TeV for ORCA6 and 1.1-7.9 TeV for ARCA6.

5.5 Muon flux detected by the KM3NeT telescopes and the CORSIKA simulations

The final result of this analysis is the comparison of the KM3NeT data with the MC simulations including all the systematic uncertainties described above. The statistical and systematic uncertainties were added in quadrature. The uncertainties from different systematic effects were summed up linearly. The relative systematic error in each bin was estimated by evaluating the corresponding uncertainty fit function in the center of the bin.

The data and MC comparisons together with the uncertainties are plotted in Fig. 5.26 for the ORCA6 detector and in Fig. 5.27 for the ARCA6 one. Uncertainty bands for the ratio between

data and MC (bottom plots in Fig. 5.26 and Fig. 5.27) were calculated using the estimated MC uncertainties described above. The lower (upper) limit of the band that is shown on the data/MC ratio plot is obtained using the upper (lower) limit of the corresponding uncertainty band for the MC muon flux. For instance, the relative upper uncertainty on the CR flux applied to vertical muons simulated for ORCA6 is 13%. This corresponds to the relative lower limit of the CR flux uncertainty band of the data/MC ratio of $1/1.13 \approx 0.88$. The value of the data/MC ratio for vertical muons in ORCA6 is 1.40. Hence, the lower limit of the CR flux uncertainty band for the ratio is 1.23. The same procedure is applied to all the uncertainty bands on the ratio plots.

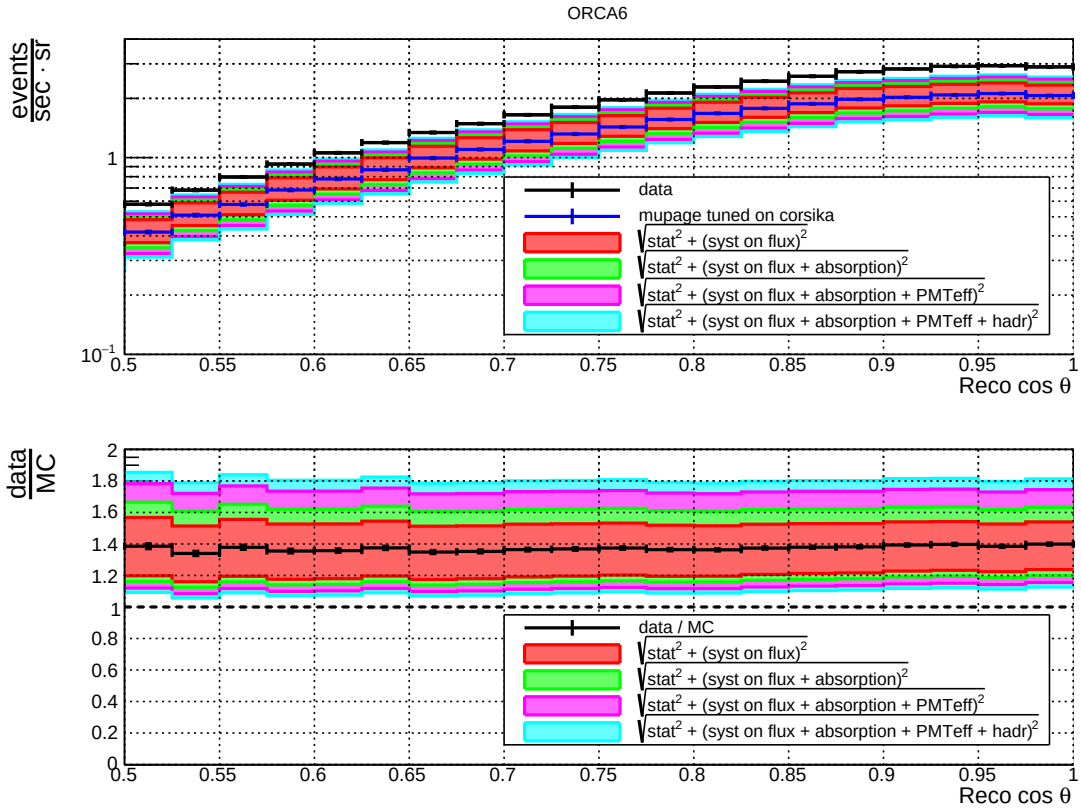

Figure 5.26: Comparison of the data (black points) and MC simulation results (blue points) for the atmospheric muons in terms of the zenith angle distribution for the ORCA6 telescope. The simulations include statistical uncertainties that are shown as black vertical lines. The systematic uncertainties are shown as cumulative bands that include uncertainty on the CR flux (red band), the light absorption length (green band), the PMT efficiency (purple band), and the hadronic interaction models (light blue band). The discrepancy is at a level of 40% and cannot be compensated by including all the uncertainties considered.

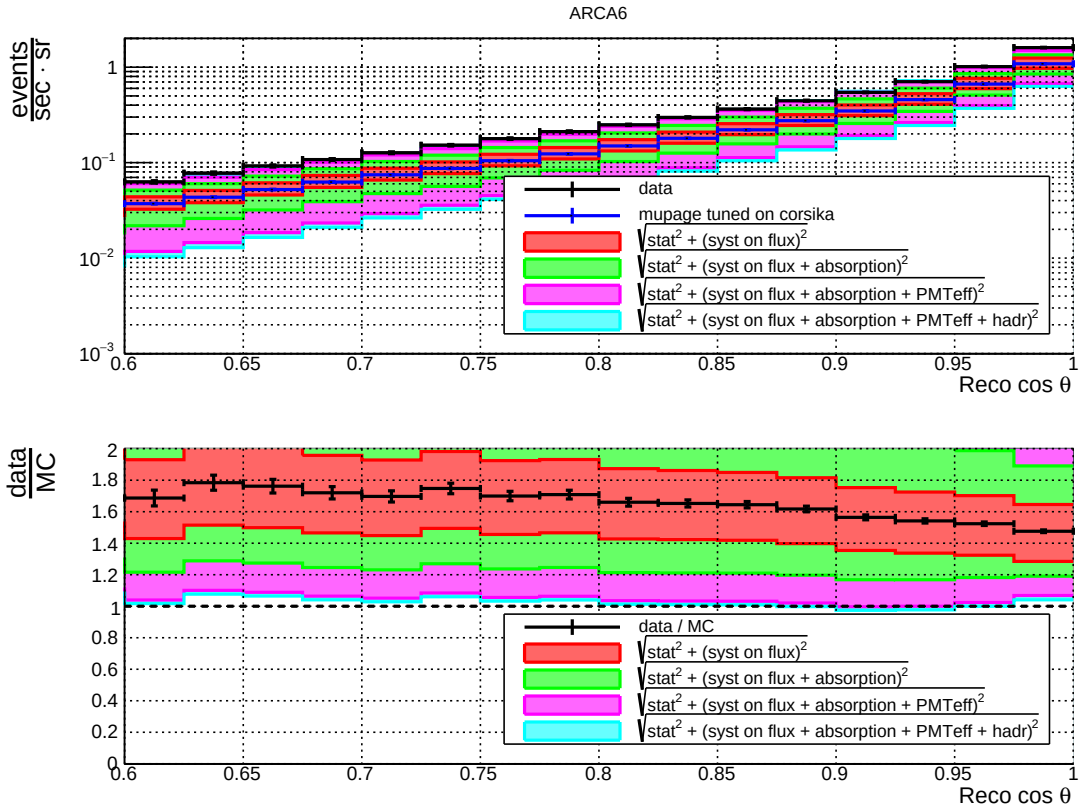

Figure 5.27: The atmospheric muon flux as a function of the cosine of the zenith angle resulting from the MC simulations (blue points) and the ARCA6 data (black points). The colored bands indicate the uncertainties that are described in the text.

5.6 Discussion of the results

5.6.1 Ratio between the data and simulations

The MC simulations underestimate the data for both the ORCA6 and ARCA6 detectors. The discrepancy for the ORCA6 telescope goes beyond the uncertainties considered in this work. The ratio between the data and simulations is flat in the considered zenith angle range. There are 40% more muons in the data with respect to the simulations.

The ARCA6 comparison plot illustrates that there is also tension between the data and MC even though the uncertainties are larger than for ORCA6. The shape of the ARCA6 data/MC ratio is not flat in contrast to the ORCA6 result. One would expect similar results for both detectors for the same slant depths. Depth of the top part of the ORCA6 detector is $d^{\text{top}}_{\text{ORCA}} = 2.25$ km, while the ARCA6 detector is located deeper with the top part being at $d^{\text{top}}_{\text{ARCA}} = 2.8$ km. Hence, the similar results are expected for the ARCA6 $\cos\theta$ value, $\cos\theta_{\text{ARCA}}$, corresponding to the lower ORCA6 $\cos\theta$ value, $\cos\theta_{\text{ORCA}} = \cos\theta_{\text{ARCA}} \cdot (d^{\text{top}}_{\text{ORCA}}/d^{\text{top}}_{\text{ARCA}})$. For example, the ARCA slant depth at $\cos\theta_{\text{ARCA}} = 1$ corresponds to the same slant depth for ORCA at $\cos\theta_{\text{ORCA}} = 0.8$, and the ratios for this $\cos\theta$ values are 1.45 and 1.40, correspondingly. This is in rough agreement if one considers the fact the energy threshold is higher in ARCA. However for lower values of $\cos\theta$, e.g. $\cos\theta_{\text{ARCA}} = 0.9$ and $\cos\theta_{\text{ORCA}} = 0.72$, the ratio becomes 1.6 and 1.4, correspondingly, so the difference is growing.

One of the possible explanations for the non-flat ARCA ratio opposite to the flat ORCA ratio and the mismatch in the ratio values between the detectors could be related to the detector response simulation uncertainties, and in particular, water properties. If one increases the length by 10% and repeats the comparison for the ARCA6 detector, Fig. 5.28, then the ratio becomes flat and at a level of 40%, the same as for the ORCA6 telescope. The same change of the water properties for the ORCA detector modifies the result by ∼5% as shown in Fig. 5.20 left and does not change the shape of the ratio. It is quite realistic, however, that the water properties are not the same at both detector sites.

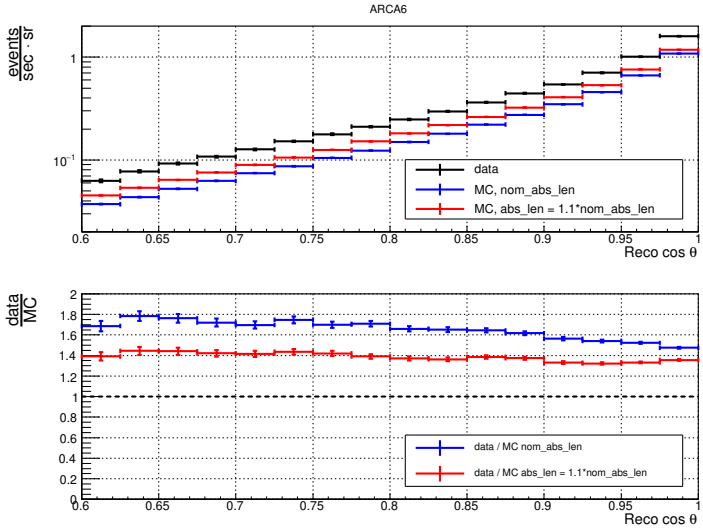

Figure 5.28: The muon zenith angle distribution obtained from the simulations with the nominal absorption length (blue points) and with the one increased by 10% (red points). The results are compared to the ARCA6 data (black points). The data/MC ratio with the modified length has a trend and value similar to the ORCA6 ratio.

5.6.2 Spectral index of the CR flux

As it can be seen from Fig. 5.26, the ratio between the data and simulations is flat in the considered region of the $\cos\theta$ space for ORCA6. Since the $\cos\theta$ distribution represents the overburden that muons have to travel in water to reach the detector, the flat ratio indicates that the shape of the simulated muon energy distribution at sea level is correct even if there is a discrepancy in the normalisation. And since the shape of the sea level muon energy spectrum depends on the primary CR flux, it may be stated that the GSF model predictions are in agreement with the KM3NeT data.

The 90% interval of events reconstructed in ORCA6 originate from primaries with energies laying in 3-350 TeV region as discussed in Chapter 3. In that energy range, the GSF approximation for the flux may be considered as a power-law spectrum and can be fitted with the corresponding function. Fig. 5.29 shows the result of the fit. The flux was multiplied by the squared value of the primary energy for a better visual representation. The considered uncertainties (vertical error bars) are taken from the GSF model. The fitting function was $A \cdot E^{-\alpha}$, where A is the flux normalisation and α corresponds to the spectral index: $\gamma = -2 + \alpha$. Therefore, the fitted value of the spectral index is -2.607 ± 0.006.

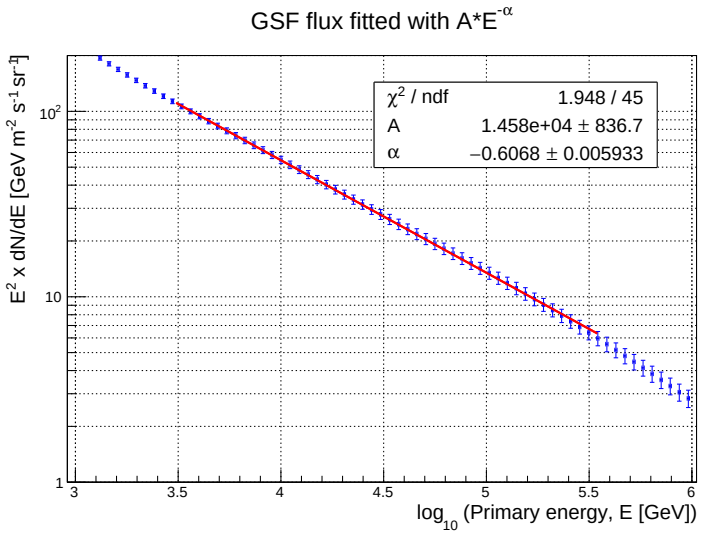

Figure 5.29: The GSF approximation for the all-particle CR flux. The flux is multiplied by the primary energy squared for a better visual representation. The GSF prediction is fitted with a power-law function in the energy range of the ORCA6 telescope.

The IceCube Collaboration has also published the results on the characterization of the muon flux properties deep under ice [62]. One of the results is the comparison of the data with the simulations in terms of the muon zenith distribution. Fig. 5.30 illustrates the ratio of the data with respect to the simulations for two different data samples. The left plot on this figure is for the trigger level data and the right one is for the high-quality data sample. The simulations were performed with CORSIKA using Sibyll 2.1 (pre-LHC) hadronic interaction model [68] and two CR flux models, H3a [120] (green points on the figure below) and GST [119] (grey points). The two aforementioned flux models provide very similar results as can be seen in Fig. 5.30.

Even though the models are different with respect to the ones used in this work, there is also an underestimation of the muon flux in the simulations with respect to the data. As reported by IceCube, the absolute value of the ratio is not a relevant quantity for the evaluation in their work due to the systematic uncertainties on the photon yield and on the CR flux. On the other hand, the shape of the ratio may serve as an estimation of the CR flux spectral index as discussed above. In order to obtain the index which corresponds to the flat data/MC ratio, they performed a fit of the toy model simulations to the data in each of the two data samples. The fitted spectral indices are 2.715 for the trigger level data and 2.855 for the high-quality sample. The ratio of the IceCube data to the MC simulations with the fitted spectral indices is also shown in Fig. 5.30.

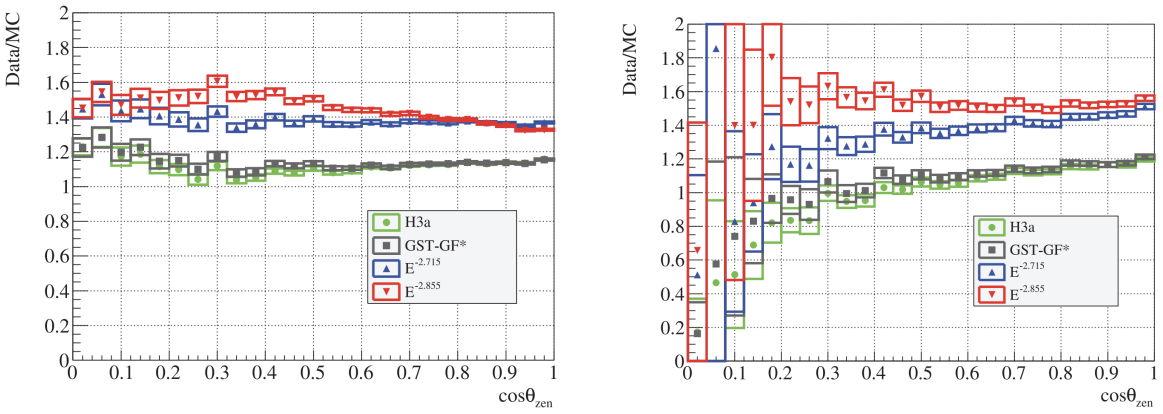

Figure 5.30: The ratio between the IceCube data and simulations for two different data samples. The left plot shows the ratio for the trigger level data, and the right one is for the high-quality data sample. The figure legend is described in the text. This figure is taken from [62].

The IceCube fit result disagrees with the spectral index of the GSF model ($\gamma = -2.607$) which gives the flat data/MC ratio for the ORCA6 telescope (Sec. 5.6.2). The H3a model that was used in the IceCube work does not provide the constant ratio between their data and simulations. But this model is, in fact, very similar to the GSF one. Fig. 5.31 illustrates the comparison of the GSF and H3a models for the primary CR energy range which is of interest in the KM3NeT and IceCube experiments. The two bottom plots on the same figure are the comparison of the model predictions for the proton (left plot) and helium (right plot) fluxes, which are the most dominant primaries for both the KM3NeT and IceCube detectors [62]. The H3a and GSF predictions agree also for these fluxes.

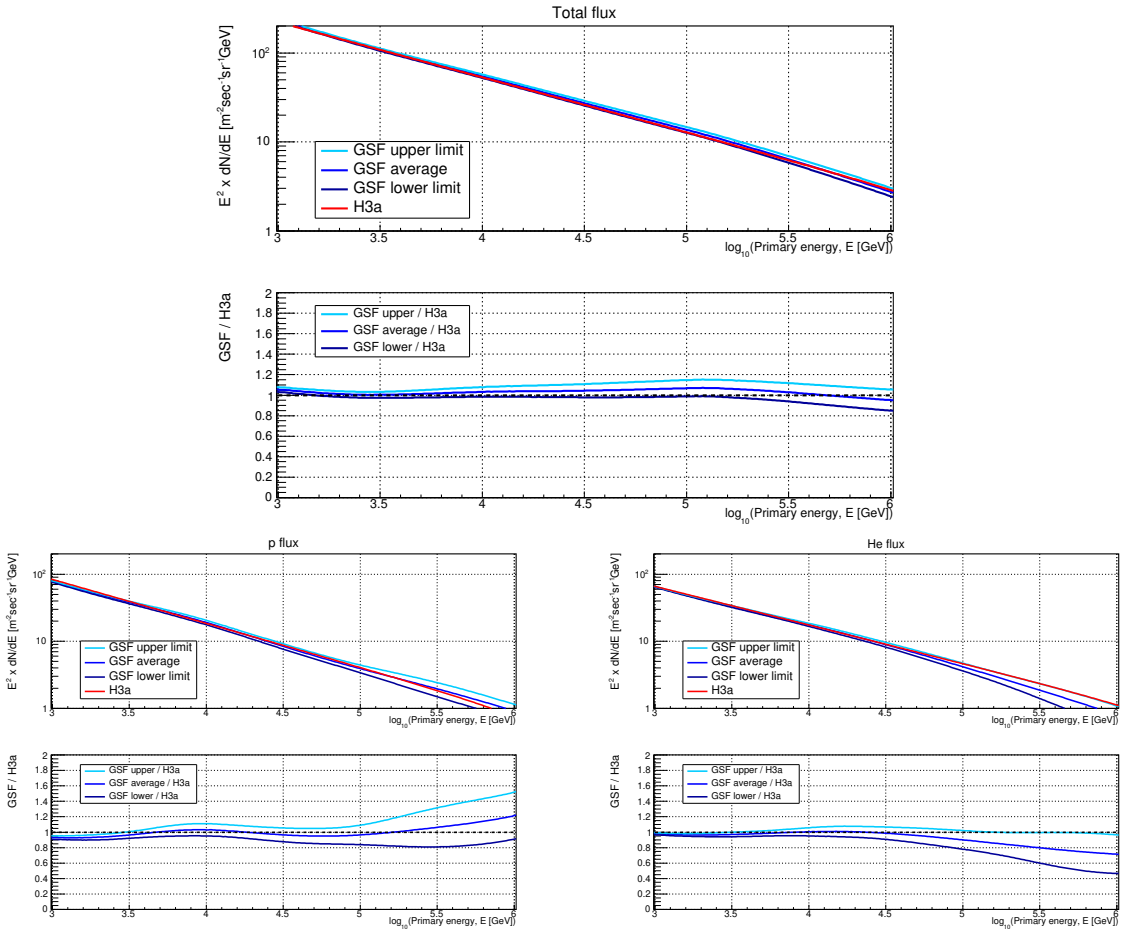

Figure 5.31: The GSF model of the CR flux compared to the H3a flux. The top plot shows the total flux predictions of these models and their ratio. The left (right) bottom plot is for the proton (helium) flux. The H3a fluxes are shown as red lines, the GSF average fluxes are in blue. The GSF lower and upper limits on the fluxes are also included in the plots and shown as the light blue and dark blue lines, correspondingly.

Differences in the results obtained by the KM3NeT and IceCube Collaborations may be explained by the systematics of two detectors and by the different hadronic interaction models used, Sibyll 2.1 [68] in the case of IceCube and Sibyll 2.3d [69] for KM3NeT. Fig. 5.32 shows the vertical atmospheric muon flux at sea level for high-energy muons obtained with the MCEq software. Since there is no Sibyll 2.3d model available in the public MCEq release, Sibyll 2.3c was used instead. In fact, the flux obtained with Sibyll 2.3c is ∼10-15% lower with respect to the Sibyll 2.1 one. Therefore, the larger data/MC discrepancy obtained in this work for the KM3NeT data is partially caused by the different hadronic model used.

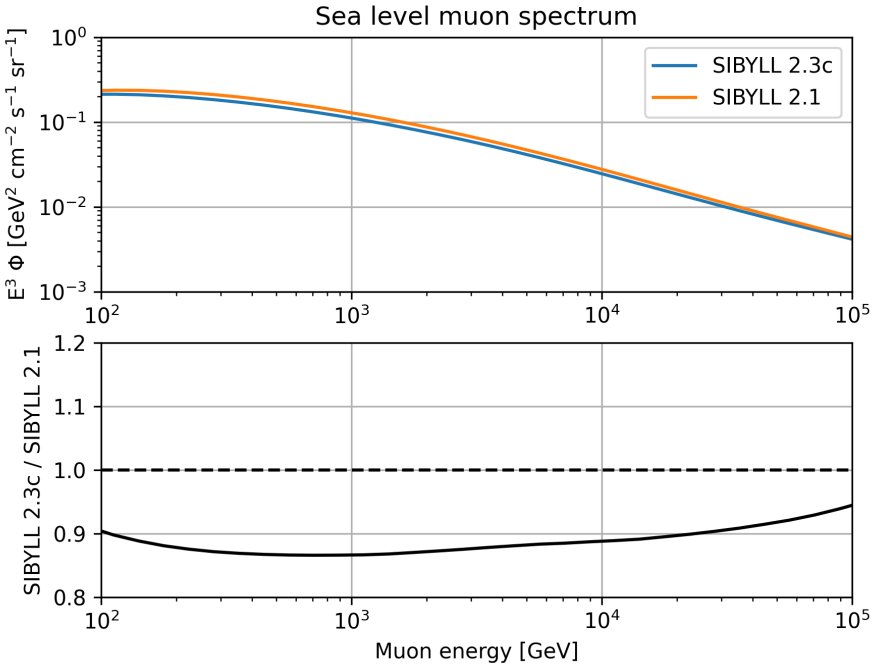

Figure 5.32: Vertical sea level muon flux produced with the MCEq software. Two hadronic interaction models were used: Sibyll 2.3c (blue line) and Sibyll 2.1 (orange line). The bottom plot shows the ratio between the two models. Sibyll 2.1 predicts a larger flux of muons with respect to Sibyll 2.3c.

5.6.3 Discrepancy between the data and simulation at sea level and underwater

As discussed in Sec. 5.1, CORSIKA with Sibyll 2.3d and GSF underestimates the sea level muon flux predicted by the analytical models and measured by several the ground-based experiments. The disagreement is at a level of ∼30%. The discrepancy between the data and simulations for the underwater muon flux seen by the ORCA6 telescope is around 40%, Sec. 5.5. That indirectly confirms that the KM3NeT simulations describe the muon propagation in water, the light generation, the detector response, and the muon reconstruction with a precision better than 10%. The 10% disagreement may be explained by the uncertainties on the light absorption length in seawater and the detector response simulation, green and purple bands on Fig. 5.26 and Fig. 5.27. The sum of the two aforementioned upper uncertainties is around 10% for the ORCA6 telescope and 20-40% for the ARCA6 detector.

5.6.4 Fluctuations in the number of muons in EAS

The Pierre Auger Observatory (PAO) has reported the measurements of the fluctuations in the number of muons in EAS produced by Ultra-High Energy (UHE) CRs ($E > 10^{18}$ eV) [180]. This measurement was found to be in agreement with the MC simulations using the recent high-energy hadronic interactions models: EPOS-LHC [71], QGSJetII-04 [70], and Sibyll 2.3d [69]. Fig. 5.33 shows the PAO result together with the predictions of the three models mentioned above. The simulations were performed assuming the pure proton (red lines) and pure iron

(blue lines) composition of the CR flux. The data points fall within the range of the proton and iron limits.

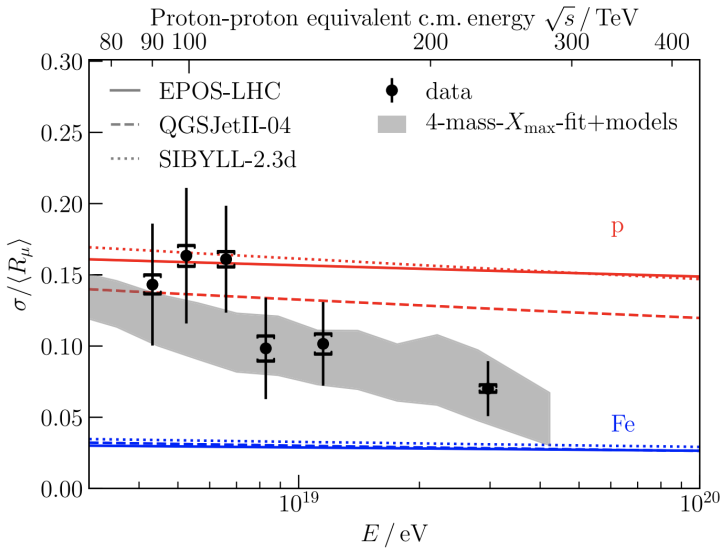

Figure 5.33: Relative fluctuations in the number of muons as a function of the CR primary energy measured by the PAO experiment (black points). Statistical errors are shown as the vertical lines, systematic uncertainties are represented by the square brackets. The red (blue) lines illustrate the predictions of the three hadronic models mentioned in the text assuming the pure proton (iron) composition of the CR flux. The gray band is also the prediction from the three hadronic models but given the mass composition measured using the depth of the shower maximum ($X_{\max}$). This figure is taken from [180].

The fluctuations in the muon number are believed to be mainly determined by the first interaction of the CR primaries with the atmosphere [181]. Hence, the possible cause of the mismatch between the simulation and data for the number of GeV muons detected on the ground (the muon puzzle) might be a small accumulative effect over many generations of EAS, or it is a very particular modification of the first interaction that may change the muon number without the impact on the fluctuations [180].

Muons detected by the KM3NeT telescopes originate from the first interactions of particles in EAS so these detectors provide direct probe of such interactions. But, as it was demonstrated in this work, there is a discrepancy between the KM3NeT data and the Sibyll 2.3d hadronic model. Therefore, it is important to notice that even though the hadronic models are able to describe the fluctuations of the muon number for UHE CRs (EeV range), they fail to describe the absolute number of TeV muons originating from the first interactions for the lower CR energies (TeV - few PeV range) as measured by the KM3NeT detectors.

Conclusions

The KM3NeT neutrino telescopes are valuable instruments to study CR properties. The telescopes are under construction at the bottom of the Mediterranean Sea near the coast of France (KM3NeT/ORCA) and Italy (KM3NeT/ARCA) at the depths of ∼2.5 km and ∼3.5 km, correspondingly. Having several kilometers of water overburden, only the high-energy (TeV) atmospheric muons are able to reach the depths of the KM3NeT detectors. Therefore, the KM3NeT measurement of the underwater muon flux is an additional input to the results from the ground-based EAS experiments which detect the lower energy (GeV) muons. The pseudorapidity of muons detected with the KM3NeT telescopes lays in the very forward region. This region is not fully covered by the existing accelerator experiments which makes the KM3NeT results useful also for the hadronic interaction studies.

In this work, the simulation of atmospheric muons for the KM3NeT experiment was performed. This simulation was compared with KM3NeT data from the partially deployed detectors already taking data underwater. The simulation included the most recent models available: Sibyll 2.3d for the high-energy hadronic interaction and GSF for CR flux. During my PhD, I contributed to the development of atmospheric muon simulation software for the Cherenkov neutrino telescopes. In particular, I developed an alternative code for the muon propagation in water that allowed to cross-check the standard KM3NeT software and resolve the issues it was affected by.

I developed a framework to tune the parameters of the fast muon generator MUPAGE on the CORSIKA full MC simulations that includes the recent models mentioned above. The framework results demonstrated that the tuned MUPAGE represents the CORSIKA results and can be used as a fast alternative to the full MC simulations. The fast generation allows the simulation of muons with the same statistics as in the real data. This goal is not achievable with the full simulations and the CPU resources available.

Then, I performed studies on systematic uncertainties. The uncertainties include that on CR flux and its composition, high-energy hadronic interaction model, light attenuation length in seawater, and detector response simulation.

Finally, I compared the KM3NeT data with the MC simulations including all systematic uncertainties mentioned above. The comparison revealed the discrepancy between the real data and the MC predictions for the underwater muon flux. There are ∼40% more muons in the data with respect to MC. Hence, the mismatch is of the same order as for the GeV muons at sea level (the muon puzzle). Muons detected with KM3NeT originate from the very first interactions of CRs in the atmosphere, while GeV muons at sea level are mostly originate in the lower parts of the atmosphere after several steps of the EAS cascade development. Thus, the measurement performed in this work provides new insights and the test-bench for possible solutions to the muon puzzle.

The KM3NeT detectors are rapidly growing. The detector performance for the atmospheric muon detection grows both in terms of statistics, but also, what is more important for this study, it improves in the quality of the muon track reconstruction. More energy is absorbed in the detector volume and more light is emitted, which allows better direction and energy reconstruction. The framework developed during my thesis is provided to the Collaboration as the internally available code with all necessary documentation. This allows this work to be

continued in the near future by the collaborators in order to extend the analysis for the larger and better KM3NeT detectors.

The main KM3NeT goals are related to the neutrinos detection and, in this aspect, the atmospheric muons are only background. Its precise knowledge improves, however, the systematics of the main physics analysis. Also atmospheric muons are the most copious events and, thus, they provide a facility for the reconstruction code tests and the detector response studies. Therefore, better knowledge about true flux of these events allows to tune the other detector properties.

Acknowledgments

First, I would like to sincerely thank my supervisors Vladimir Kulikovskiy and Matteo Sanguineti for their endless support during this work. All the discussions we had were always very useful and, as I believe, it helped a lot to improve the quality of this analysis and, in general, my understanding of the research work.

I would like to express my deep gratitude to Marco Anghinolfi. He was supporting me with all his kindness since my first days in Genova back in 2018. Marco is now retired but he was a mentor to me during all these years. In my view, the very nice KM3NeT group in Genova that we have now is his great merit.

I really appreciate all the meetings, discussions, and fun that we had with the members of the KM3NeT Collaboration. All the collaborators are always friendly and respectful to each other which I find really great. I would like to specially thank Bruny Baret, Ronald Bruijn, Rosa Coniglione, Carla Distefano, Thijs Juan van Eeden, Sergio Alves Garre, Juan Palacios González, Aart Heijboer, Piotr Kalaczynski, Valentin Pestel, Maurizio Spurio, Mauro Taiuti, Hichem Tedjditi, and Godefroy Vannoye.

Also, I appreciated a lot the careful thesis evaluation by the Referees, Dr. Hans Dembinski and Dr. Anatoli Fedynitch. Their comments and suggestions were very useful and helped to improve the clearness of this thesis.

Finally, I would like to thank my wife Julia and my family for their never ending support.

In general, I really enjoyed the time I spent in Genova with all the lovely people I met. The PhD life has its ups and downs but I never regret my choice to work here in Genova and I hope we all will meet again to have more fun and, of course, to perform new great studies.

Bibliography

[1] Thomas K Gaisser, Ralph Engel, and Elisa Resconi. *Cosmic rays and particle physics*. Cambridge University Press, 2016.

[2] Carl David Anderson and Seth Henry Neddermeyer. *The Production and Properties of Positrons*, volume 46. PA Norstedt & söner, 1937.

[3] Seth H Neddermeyer and Carl D Anderson. Note on the nature of cosmic-ray particles. *Physical Review*, 51(10):884, 1937.

[4] Viktor F Hess. Uber beobachtungen der durchdringenden strahlung bei sieben freiballonfahrten. *Phys. Zeits.*, 13:1084–1091, 1912.

[5] Theodor Wulf et al. Observations on the radiation of high penetration power on the Eiffel tower. *Physikalische Zeitschrift*, 11(811):2155–304, 1910.

[6] Werner KOLHORSTER. Messungen der durchdringenden Strahlung im Freiballon in grosseren Hohen. *Phys. Zeits.*, 14:1153–1156, 1913.

[7] Brigitte Falkenburg and Wolfgang Rhode. *From Ultra Rays to Astroparticles*. Springer, 2012.

[8] R Alfaro, C Alvarez, JD Álvarez, R Arceo, JC Arteaga-Velázquez, D Avila Rojas, HA Ayala Solares, AS Barber, A Becerril, E Belmont-Moreno, et al. All-particle cosmic ray energy spectrum measured by the HAWC experiment from 10 to 500 TeV. *Physical Review D*, 96(12):122001, 2017.

[9] Katherine Rawlins, Tom Feusels, Sam De Ridder, and Serap Tilav. Latest results on cosmic ray spectrum and composition from three years of IceTop and IceCube. In *Proceedings of ICRC*, 2015.

[10] WD Apel, JC Arteaga-Velázquez, K Bekk, M Bertaina, J Blümer, H Bozdog, IM Brancus, P Buchholz, E Cantoni, A Chiavassa, et al. The spectrum of high-energy cosmic rays measured with KASCADE-grande. *Astroparticle Physics*, 36(1):183–194, 2012.

[11] Sven Schoo, WD Apel, JC Arteaga-Velázquez, K Bekk, M Bertaina, J Blümer, H Bozdog, IM Brancus, E Cantoni, A Chiavassa, et al. The energy spectrum of cosmic rays in the range from 10^{14} to 10^{18} ev. In *34th International Cosmic Ray Conference (ICRC2015)*, volume 34, page 263, 2015.

[12] Ines Valino. The flux of ultra-high energy cosmic rays after ten years of operation of the Pierre Auger Observatory. In *The 34th International Cosmic Ray Conference*, volume 236, page 271. SISSA Medialab, 2016.

[13] Alexander Aab, Pedro Abreu, Marco Aglietta, Justin M Albury, Ingomar Allekotte, Alejandro Almela, J Alvarez Castillo, Jaime Alvarez-Muñiz, R Alves Batista, Gioacchino Alex Anastasi, et al. Depth of maximum of air-shower profiles at the Pierre Auger Observatory. II. composition implications. *Physical Review D*, 90(12):122006, 2014.

[14] M Aguilar, D Aisa, B Alpat, A Alvino, G Ambrosi, K Andeen, L Arruda, N Attig, P Azzarello, A Bachlechner, et al. Precision measurement of the proton flux in primary cosmic rays from rigidity 1 GV to 1.8 TV with the alpha magnetic spectrometer on the international space station. *Physical review letters*, 114(17):171103, 2015.

[15] Mea Aguilar, D Aisa, B Alpat, A Alvino, G Ambrosi, K Andeen, L Arruda, N Attig, P Azzarello, A Bachlechner, et al. Precision measurement of the helium flux in primary cosmic rays of rigidities 1.9 GV to 3 TV with the alpha magnetic spectrometer on the international space station. *Physical review letters*, 115(21):211101, 2015.

[16] HS Ahn, P Allison, MG Bagliesi, L Barbier, JJ Beatty, G Bigongiari, TJ Brandt, JT Childers, NB Conklin, S Coutu, et al. Energy spectra of cosmic-ray nuclei at high energies. *The Astrophysical Journal*, 707(1):593, 2009.

[17] YS Yoon, HS Ahn, PS Allison, MG Bagliesi, JJ Beatty, G Bigongiari, PJ Boyle, JT Childers, NB Conklin, Stephane Coutu, et al. Cosmic-ray proton and helium spectra from the first CREAM flight. *The Astrophysical Journal*, 728(2):122, 2011.

[18] JJ Engelmann, P Ferrando, A Soutoul, Ph Goret, E Juliusson, L Koch-Miramond, N Lund, P Masse, B Peters, N Petrou, et al. Charge composition and energy spectra of cosmic-ray nuclei for elements from Be to NI - results from HEAO-3-C2. *Astronomy and Astrophysics*, 233:96–111, 1990.

[19] Hans Dembinski, Ralph Engel, Anatoli Fedynitch, Thomas Gaisser, Felix Riehn, and Todor Stanev. Data-driven model of the cosmic-ray flux and mass composition from 10 GeV to 10^{11} GeV. *arXiv preprint arXiv:1711.11432*, 2017.

[20] Johannes Albrecht, Lorenzo Cazon, Hans Dembinski, Anatoli Fedynitch, Karl-Heinz Kampert, Tanguy Pierog, Wolfgang Rhode, Dennis Soldin, Bernhard Spaan, Ralf Ulrich, et al. The Muon Puzzle in cosmic-ray induced air showers and its connection to the Large Hadron Collider. *Astrophysics and Space Science*, 367(3):27, 2022.

[21] Alessandro De Angelis and Mário Pimenta. *Introduction to particle and astroparticle physics*. Springer, 2018.

[22] Maurizio Spurio, Spurio, and Bellantone. *Probes of Multimessenger Astrophysics*. Springer, 2018.

[23] AM Hillas. Can diffusive shock acceleration in supernova remnants account for high-energy galactic cosmic rays? *Journal of Physics G: Nuclear and Particle Physics*, 31(5):R95, 2005.

[24] Tadeusz Wibig and Arnold W Wolfendale. At what particle energy do extragalactic cosmic rays start to predominate? *Journal of Physics G: Nuclear and Particle Physics*, 31(3):255, 2005.

[25] Kenneth Greisen. End to the cosmic-ray spectrum? *Physical Review Letters*, 16(17):748, 1966.

[26] Georgi T Zatsepin and Vadem A Kuz'min. Upper limit of the spectrum of cosmic rays. *Soviet Journal of Experimental and Theoretical Physics Letters*, 4:78, 1966.

[27] Alexander Aab, Pedro Abreu, Marco Aglietta, Justin M Albury, Ingomar Allekotte, Alejandro Almela, J Alvarez Castillo, Jaime Alvarez-Muñiz, R Alves Batista, Gioacchino Alex Anastasi, et al. Features of the energy spectrum of cosmic rays above 2.5×10^{18} eV using the Pierre Auger Observatory. *Physical review letters*, 125(12):121106, 2020.

[28] Alexey Yushkov, Pierre Auger Collaboration, et al. Mass composition of cosmic rays with energies above $10^{17.2}$ eV from the Hybrid Data of the Pierre Auger Observatory. 358:482, 2021.

[29] Rasha U Abbasi, M Abe, T Abu-Zayyad, M Allen, R Anderson, R Azuma, E Barcikowski, JW Belz, DR Bergman, SA Blake, et al. Indications of intermediate-scale anisotropy of cosmic rays with energy greater than 57 eev in the northern sky measured with the surface detector of the telescope array experiment. *The Astrophysical Journal Letters*, 790(2):L21, 2014.

[30] Alexander Aab, Pedro Abreu, Marco Aglietta, Ivone Freire Mota Albuquerque, Justin M Albury, Ingomar Allekotte, Alejandro Almela, J Alvarez Castillo, Jaime Alvarez-Muñiz, Gioacchino Alex Anastasi, et al. Large-scale cosmic-ray anisotropies above 4 eev measured by the Pierre Auger Observatory. *The Astrophysical Journal*, 868(1):4, 2018.

[31] Anthony M Hillas. The origin of ultra-high-energy cosmic rays. *Annual review of astronomy and astrophysics*, 22(1):425–444, 1984.

[32] Ke Fang, Kumiko Kotera, and Angela V Olinto. Newly born pulsars as sources of ultrahigh energy cosmic rays. *The Astrophysical Journal*, 750(2):118, 2012.

[33] Chris Fryer, Willy Benz, Marc Herant, and Stirling A Colgate. What can the accretion-induced collapse of white dwarfs really explain? *The Astrophysical Journal*, 516(2):892, 1999.

[34] GA Bazilevskaya. Observations of variability in cosmic rays. *Space Science Reviews*, 94(1-2):25–38, 2000.

[35] Sebastian Heinz and Rashid Sunyaev. Cosmic rays from microquasars: A narrow component to the CR spectrum? *Astronomy & Astrophysics*, 390(2):751–766, 2002.

[36] LJ Gleeson and WI Axford. Cosmic rays in the interplanetary medium. *The Astrophysical Journal*, 149:L115, 1967.

[37] Julia Becker Tjus and Lukas Merten. Closing in on the origin of Galactic cosmic rays using multimessenger information. *Physics Reports*, 872:1–98, 2020.

[38] M Amenomori, YW Bao, XJ Bi, D Chen, TL Chen, WY Chen, Xu Chen, Y Chen, SW Cui, LK Ding, et al. First detection of sub-pev diffuse gamma rays from the galactic disk: Evidence for ubiquitous galactic cosmic rays beyond pev energies. *Physical Review Letters*, 126(14):141101, 2021.

[39] Marcus C Beck, Alexander M Beck, Rainer Beck, Klaus Dolag, Andrew W Strong, and Peter Nielaba. New constraints on modelling the random magnetic field of the MW. *Journal of Cosmology and Astroparticle Physics*, 2016(05):056, 2016.

[40] EG Berezhko. Cosmic rays from active galactic nuclei. *The Astrophysical Journal*, 684(2):L69, 2008.

[41] Noemie Globus, Denis Allard, Robert Mochkovitch, and Etienne Parizot. UHECR acceleration at GRB internal shocks. *Monthly Notices of the Royal Astronomical Society*, 451(1):751–790, 2015.

[42] Kohta Murase, Charles D Dermer, Hajime Takami, and Giulia Migliori. Blazars as ultra-high-energy cosmic-ray sources: implications for TeV gamma-ray observations. *The Astrophysical Journal*, 749(1):63, 2012.

[43] Björn Eichmann, Jörg P Rachen, Lukas Merten, Arjen van Vliet, and J Becker Tjus. Ultra-high-energy cosmic rays from radio galaxies. *Journal of Cosmology and Astroparticle Physics*, 2018(02):036, 2018.

[44] Gianfranco Brunetti and Thomas W Jones. Cosmic rays in galaxy clusters and their nonthermal emission. *International Journal of Modern Physics D*, 23(04):1430007, 2014.

[45] Nicholas Senno, Peter Mészáros, Kohta Murase, Philipp Baerwald, and Martin J Rees. Extragalactic star-forming galaxies with hypernovae and supernovae as high-energy neutrino and gamma-ray sources: the case of the 10 TeV neutrino data. *The Astrophysical Journal*, 806(1):24, 2015.

[46] Abraham Achterberg, Yves A Gallant, Colin A Norman, and Donald B Melrose. Intergalactic propagation of UHE cosmic rays. *arXiv preprint astro-ph/9907060*, 1999.

[47] MG Aartsen, M Ackermann, J Adams, Juan A Aguilar, M Ahlers, M Ahrens, D Altmann, K Andeen, T Anderson, I Ansseau, et al. Astrophysical neutrinos and cosmic rays observed by IceCube. *Advances in Space Research*, 62(10):2902–2930, 2018.

[48] Enrico Fermi. On the origin of the cosmic radiation. *Physical review*, 75(8):1169, 1949.

[49] David Bohm. *The special theory of relativity*. Routledge, 2015.

[50] Lev Davidovich Landau and Evgenii Mikhailovich Lifshitz. *Fluid Mechanics: Landau and Lifshitz: Course of Theoretical Physics, Volume 6*, volume 6. Elsevier, 2013.

[51] Oea Adriani, GC Barbarino, GA Bazilevskaya, R Bellotti, M Boezio, EA Bogomolov, L Bonechi, M Bongi, V Bonvicini, S Borisov, et al. PAMELA measurements of cosmic-ray proton and helium spectra. *Science*, 332(6025):69–72, 2011.

[52] AD Panov, Jr H Adams, HS Ahn, GL Bashinzhagyan, JW Watts, JP Wefel, J Wu, O Ganel, TG Guzik, VI Zatsepin, et al. Energy spectra of abundant nuclei of primary cosmic rays from the data of ATIC-2 experiment: Final results. *Bulletin of the Russian Academy of Sciences: Physics*, 73:564–567, 2009.

[53] Koh Abe, Hideyuki Fuke, Sadakazu Haino, T Hams, M Hasegawa, A Horikoshi, A Itazaki, KC Kim, Teruyuki Kumazawa, A Kusumoto, et al. Measurements of cosmic-ray proton and helium spectra from the BESS-Polar long-duration balloon flights over Antarctica. *The Astrophysical Journal*, 822(2):65, 2016.

[54] Dietrich Mueller, Simon P Swordy, Peter Meyer, Jacques L'Heureux, and John M Grunsfeld. Energy spectra and composition of primary cosmic rays. *Astrophysical Journal, Part 1 (ISSN 0004-637X), vol. 374, June 10, 1991, p. 356-365.*, 374:356–365, 1991.

[55] F Aharonian, AG Akhperjanian, AR Bazer-Bachi, M Beilicke, W Benbow, D Berge, K Bernlöhr, C Boisson, O Bolz, V Borrel, et al. First ground-based measurement of atmospheric Cherenkov light from cosmic rays. *Physical Review D*, 75(4):042004, 2007.

[56] K Asakimori, TH Burnett, ML Cherry, K Chevli, MJ Christ, S Dake, JH Derrickson, WF Fountain, M Fuki, JC Gregory, et al. Cosmic-ray proton and helium spectra: results from the JACEE experiment. *The Astrophysical Journal*, 502(1):278, 1998.

[57] VA Derbina, VI Galkin, M Hareyama, Y Hirakawa, Y Horiuchi, M Ichimura, N Inoue, E Kamioka, T Kobayashi, VV Kopenkin, et al. Cosmic-ray spectra and composition in the energy range of 10-1000 TeV per particle obtained by the RUNJOB experiment. *The Astrophysical Journal*, 628(1):L41, 2005.

[58] M Ave, PJ Boyle, F Gahbauer, C Höppner, JR Hörandel, M Ichimura, D Müller, and A Romero-Wolf. Composition of primary cosmic-ray nuclei at high energies. *The Astrophysical Journal*, 678(1):262, 2008.

[59] Particle Data Group, RL Workman, VD Burkert, V Crede, E Klempt, U Thoma, L Tiator, K Agashe, G Aielli, BC Allanach, et al. Review of particle physics. *Progress of theoretical and experimental physics*, 2022(8):083C01, 2022.

[60] Michelangelo Ambrosio, R Antolini, G Auriemma, R Baker, A Baldini, GC Barbarino, BC Barish, G Battistoni, R Bellotti, C Bemporad, et al. Vertical muon intensity measured with MACRO at the Gran Sasso laboratory. *Physical Review D*, 52(7):3793, 1995.

[61] JA Aguilar, A Albert, G Anton, S Anvar, M Ardid, AC Assis Jesus, T Astraatmadja, J-J Aubert, R Auer, B Baret, et al. Zenith distribution and flux of atmospheric muons measured with the 5-line ANTARES detector. *Astroparticle Physics*, 34(3):179–184, 2010.

[62] MG Aartsen, K Abraham, M Ackermann, J Adams, JA Aguilar, M Ahlers, M Ahrens, D Altmann, T Anderson, M Archinger, et al. Characterization of the atmospheric muon flux in IceCube. *Astroparticle physics*, 78:1–27, 2016.

[63] M Ageron, Sebastiano Aiello, F Ameli, Michel Andre, Giorgos Androulakis, Marco Anghinolfi, Gisela Anton, Miguel Ardid, Julien Aublin, Christos Bagatelas, et al. Dependence of atmospheric muon flux on seawater depth measured with the first KM3NeT detection units. *The European Physical Journal C*, 80(2):1–11, 2020.

[64] RU Abbasi, M Abe, T Abu-Zayyad, M Allen, R Azuma, E Barcikowski, JW Belz, DR Bergman, SA Blake, R Cady, et al. Study of muons from ultrahigh energy cosmic ray air showers measured with the Telescope Array experiment. *Physical Review D*, 98(2):022002, 2018.

[65] Anatoli Fedynitch, Ralph Engel, Thomas K Gaisser, Felix Riehn, and Todorov Stanev. MCE_Q - numerical code for inclusive lepton flux calculations. *PoS*, page 1129, 2016.

[66] Dieter Heck, Johannes Knapp, JN Capdevielle, G Schatz, T Thouw, et al. CORSIKA: A Monte Carlo code to simulate extensive air showers. *Report fzka*, 6019(11), 1998.

[67] James Matthews. A Heitler model of extensive air showers. *Astroparticle Physics*, 22(5-6):387–397, 2005.

[68] Eun-Joo Ahn, Ralph Engel, Thomas K Gaisser, Paolo Lipari, and Todor Stanev. Cosmic ray interaction event generator SIBYLL 2.1. *Physical Review D*, 80(9):094003, 2009.

[69] Felix Riehn, Ralph Engel, Anatoli Fedynitch, Thomas K Gaisser, and Todor Stanev. Hadronic interaction model Sibyll 2.3 d and extensive air showers. *Physical Review D*, 102(6):063002, 2020.

[70] Sergey Ostapchenko. Monte Carlo treatment of hadronic interactions in enhanced Pomeron scheme: QGSJET-II model. *Physical Review D*, 83(1):014018, 2011.

[71] T Pierog, Iu Karpenko, JM Katzy, E Yatsenko, and Klaus Werner. EPOS LHC: Test of collective hadronization with data measured at the CERN large hadron collider. *Physical Review C*, 92(3):034906, 2015.

[72] Alexander Aab, P Abreu, MARCO Aglietta, EJ Ahn, I Al Samarai, IFM Albuquerque, I Allekotte, J Allen, P Allison, A Almela, et al. Muons in air showers at the Pierre Auger Observatory: Mean number in highly inclined events. *Physical Review D*, 91(3):032003, 2015.

[73] T Abu-Zayyad, K Belov, DJ Bird, J Boyer, Z Cao, M Catanese, GF Chen, RW Clay, CE Covault, JW Cronin, et al. Evidence for changing of cosmic ray composition between 10^{17} and 10^{18} eV from multicomponent measurements. *Physical Review Letters*, 84(19):4276, 2000.

[74] AG Bogdanov, DM Gromushkin, RP Kokoulin, G Mannocchi, AA Petrukhin, O Saavedra, G Trinchero, DV Chernov, VV Shutenko, and II Yashin. Investigation of the properties of the flux and interaction of ultrahigh-energy cosmic rays by the method of local-muon-density spectra. *Physics of Atomic Nuclei*, 73:1852–1869, 2010.

[75] Hans Dembinski. Investigating cosmic rays and air shower physics with icecube/icetop. In *EPJ Web of Conferences*, volume 145, page 01003. EDP Sciences, 2017.

[76] WD Apel, JC Arteaga-Velázquez, K Bekk, M Bertaina, J Blümer, H Bozdog, IM Brancus, E Cantoni, A Chiavassa, F Cossavella, et al. Probing the evolution of the eas muon content in the atmosphere with KASCADE-Grande. *Astroparticle Physics*, 95:25–43, 2017.

[77] AG Bogdanov, RP Kokoulin, G Mannocchi, AA Petrukhin, O Saavedra, VV Shutenko, G Trinchero, and II Yashin. Investigation of very high energy cosmic rays by means of inclined muon bundles. *Astroparticle Physics*, 98:13–20, 2018.

[78] HP Dembinski, JC Arteaga-Velázquez, L Cazon, R Conceição, J Gonzalez, Y Itow, D Ivanov, NN Kalmykov, I Karpikov, S Müller, et al. Report on tests and measurements of hadronic interaction properties with air showers. In *EPJ Web of Conferences*, volume 210, page 02004. EDP Sciences, 2019.

[79] Silvia Adrian-Martinez, M Ageron, F Aharonian, S Aiello, A Albert, F Ameli, E Anassontzis, M Andre, G Androulakis, M Anghinolfi, et al. Letter of intent for KM3NeT 2.0. *Journal of Physics G: Nuclear and Particle Physics*, 43(8):084001, 2016.

[80] Matteo Sanguineti. Status and physics results of the km3net experiment. *Il nuovo cimento C*, 46(1):1–8, 2023.

[81] Pavel Alekseevič Čerenkov. Visible radiation produced by electrons moving in a medium with velocities exceeding that of light. *Physical Review*, 52(4):378, 1937.

[82] S Aiello, Arnauld Albert, Mohammed Alshamsi, S Alves Garre, Zineb Aly, Antonio Ambrosone, Fabrizio Ameli, Michel Andre, Giorgos Androulakis, Marco Anghinolfi, et al. Nanobeacon: A time calibration device for the KM3NeT neutrino telescope. *Nuclear Instruments and Methods in Physics Research Section A: Accelerators, Spectrometers, Detectors and Associated Equipment*, 1040:167132, 2022.

[83] Joseph A Formaggio and Geralyn P Zeller. From eV to EeV: Neutrino cross sections across energy scales. *Reviews of Modern Physics*, 84(3):1307, 2012.

[84] Dieter Rein and Lalit M Sehgal. Neutrino-excitation of baryon resonances and single pion production. *Annals of Physics*, 133(1):79–153, 1981.

[85] I Schienbein, JY Yu, K Kovařík, C Keppel, JG Morfin, FI Olness, and JF Owens. Parton distribution function nuclear corrections for charged lepton and neutrino deep inelastic scattering processes. *Physical Review D*, 80(9):094004, 2009.

[86] S Aiello, Arthur Albert, Mohammed Alshamsi, S Alves Garre, Zineb Aly, Antonio Ambrosone, Fabrizio Ameli, Michel Andre, Giorgos Androulakis, Marco Anghinolfi, et al. The KM3NeT multi-PMT optical module. *Journal of Instrumentation*, 17(07):P07038, 2022.

[87] S Aiello, SE Akrame, F Ameli, EG Anassontzis, M Andre, G Androulakis, M Anghinolfi, G Anton, M Ardid, J Aublin, et al. Characterisation of the Hamamatsu photomultipliers for the KM3NeT Neutrino Telescope. *Journal of Instrumentation*, 13(05):P05035, 2018.

[88] Karel Willem Melis. *Studying the Universe from -3000m N.A.P.* PhD thesis, Amsterdam U., 2021.

[89] Sebastiano Aiello, Fabrizio Ameli, Michel Andre, Giorgos Androulakis, Marco Anghinolfi, Gisela Anton, Miquel Ardid, Julien Aublin, Christos Bagatelas, Giancarlo Barbarino, et al. KM3NeT front-end and readout electronics system: hardware, firmware, and software. *Journal of Astronomical Telescopes, Instruments, and Systems*, 5(4):046001–046001, 2019.

[90] Michel Ageron, JA Aguilar, Imen Al Samarai, A Albert, F Ameli, M André, M Anghinolfi, G Anton, S Anvar, M Ardid, et al. ANTARES: the first undersea neutrino telescope. *Nuclear Instruments and Methods in Physics Research Section A: Accelerators, Spectrometers, Detectors and Associated Equipment*, 656(1):11–38, 2011.

[91] Rasha Abbasi, Markus Ackermann, John Adams, Markus Ahlers, J Ahrens, K Andeen, Jan Auffenberg, Xinhua Bai, Michael Baker, SW Barwick, et al. The IceCube data acquisition system: Signal capture, digitization, and timestamping. *Nuclear Instruments and Methods in Physics Research Section A: Accelerators, Spectrometers, Detectors and Associated Equipment*, 601(3):294–316, 2009.

[92] Sebastiano Aiello, SE Akrame, F Ameli, EG Anassontzis, Michel Andre, G Androulakis, Marco Anghinolfi, G Anton, Miguel Ardid, Julien Aublin, et al. Sensitivity of the KM3NeT/ARCA neutrino telescope to point-like neutrino sources. *Astroparticle Physics*, 111:100–110, 2019.

[93] S Aiello, Arthur Albert, Sergio Alves Garre, Z Aly, A Ambrosone, F Ameli, M Andre, G Androulakis, M Anghinolfi, M Anguita, et al. Determining the neutrino mass ordering and oscillation parameters with KM3NeT/ORCA. *The European Physical Journal C*, 82(1):26, 2022.

[94] John G Learned and Sandip Pakvasa. Detecting ν_τ oscillations at PeV energies. *Astroparticle Physics*, 3(3):267–274, 1995.

[95] The Global Neutrino Network website. https://www.globalneutrinonetwork.org/.

[96] AV Avrorin, AD Avrorin, VM Aynutdinov, R Bannasch, Z Bardacova, IA Belolaptikov, VB Brudanin, NM Budnev, AR Gafarov, KV Golubkov, et al. Baikal-GVD experiment. *Physics of Atomic Nuclei*, 83:916–921, 2020.

[97] Mark G Aartsen, M Ackermann, J Adams, JA Aguilar, M Ahlers, M Ahrens, D Altmann, K Andeen, T Anderson, I Ansseau, et al. The IceCube Neutrino Observatory: instrumentation and online systems. *Journal of Instrumentation*, 12(03):P03012, 2017.

[98] Rasha Abbasi, Yasser Abdou, T Abu-Zayyad, M Ackermann, J Adams, JA Aguilar, M Ahlers, MM Allen, D Altmann, K Andeen, et al. The design and performance of IceCube DeepCore. *Astroparticle physics*, 35(10):615–624, 2012.

[99] Rasha Abbasi, Yasser Abdou, M Ackermann, J Adams, JA Aguilar, M Ahlers, D Altmann, K Andeen, J Auffenberg, X Bai, et al. IceTop: The surface component of IceCube. *Nuclear Instruments and Methods in Physics Research Section A: Accelerators, Spectrometers, Detectors and Associated Equipment*, 700:188–220, 2013.

[100] Paul Doll, J Engler, HJ Gils, D Heck, N Heide, H Keim, HO Klages, J Knapp, HJ Mayer, H Mueller, et al. The karlsruhe cosmic ray project KASCADE. *Verhandlungen der Deutschen Physikalischen Gesellschaft;(Germany, FR)*, 25(1), 1990.

[101] Alexander Aab, Pedro Abreu, Marco Aglietta, Justin M Albury, Ingomar Allekotte, Alejandro Almela, J Alvarez Castillo, Jaime Alvarez-Muñiz, R Alves Batista, Gioacchino Alex Anastasi, et al. Muons in air showers at the Pierre Auger Observatory: Measurement of atmospheric production depth. *Physical Review D*, 90(1):012012, 2014.

[102] S Aiello, Arthur Albert, Sergio Alves Garre, Zineb Aly, Antonio Ambrosone, F Ameli, Michel Andre, Marco Anghinolfi, M Anguita, M Ardid, et al. First observation of the cosmic ray shadow of the Moon and the Sun with KM3NeT/ORCA. *The European Physical Journal C*, 83(4):344, 2023.

[103] Marcus Bleicher, E Zabrodin, Christian Spieles, Steffen A Bass, Christoph Ernst, Sven Soff, L Bravina, Mohamed Belkacem, Henning Weber, Horst Stöcker, et al. Relativistic hadron-hadron collisions in the ultra-relativistic quantum molecular dynamics model. *Journal of Physics G: Nuclear and Particle Physics*, 25(9):1859, 1999.

[104] Alice Collaboration. Performance of the ALICE experiment at the CERN LHC. *International Journal of Modern Physics A*, 29(24):1430044, 2014.

[105] Georges Aad, P Eerola, ATLAS collaboration, et al. Expected performance of the ATLAS experiment-detector, trigger and physics. 2008.

[106] Oscar Adriani, L Bonechi, M Bongi, G Castellini, R D'Alessandro, DA Faus, K Fukui, M Grandi, M Haguenauer, Y Itow, et al. The LHCf detector at the CERN large hadron collider. *Journal of Instrumentation*, 3(08):S08006, 2008.

[107] O Surányi, A Al-Bataineh, J Bowen, S Cooper, M Csanád, V Hagopian, D Ingram, C Ferraioli, T Grassi, R Kellogg, et al. Performance of the CMS Zero Degree Calorimeters in pPb collisions at the LHC. *Journal of Instrumentation*, 16(05):P05008, 2021.

[108] Giovanni Anelli, G Antchev, P Aspell, V Avati, MG Bagliesi, V Berardi, M Berretti, V Boccone, U Bottigli, M Bozzo, et al. The TOTEM experiment at the CERN large hadron collider. *Journal of Instrumentation*, 3(08):S08007, 2008.

[109] LHCb Collaboration. LHCb detector performance. *International Journal of Modern Physics A*, 30(07):1530022, 2015.

[110] K Carvalho Akiba, F Alessio, N Bondar, W Byczynski, V Coco, P Collins, R Dumps, R Dzhelyadin, P Gandini, BR Gruberg Cazon, et al. The HeRSCheL detector: high-rapidity shower counters for LHCb. *Journal of Instrumentation*, 13(04):P04017, 2018.

[111] R Bruce, MA Jebramcik, JM Jowett, T Mertens, and M Schaumann. Performance and luminosity models for heavy-ion operation at the CERN large hadron collider. *The European Physical Journal Plus*, 136(7):745, 2021.

[112] A Fedynitch and R Engel. Revision of the high energy hadronic interaction models PHOJET/DPMJET-III. 2015.

[113] Piotr Kalaczyński, KM3NeT Collaboration, et al. Comparison of the measured atmospheric muon rate with Monte Carlo simulations and sensitivity study for detection of prompt atmospheric muons with KM3NeT. *Journal of Instrumentation*, 16(09):C09035, 2021.

[114] A Capella, U Sukhatme, C-I Tan, and J Tran Thanh Van. Dual parton model. *Physics Reports*, 236(4-5):225–329, 1994.

[115] Loyal Durand and Pi Hong. QCD and rising cross sections. *Physical Review Letters*, 58(4):303, 1987.

[116] John T Emmert, Douglas Patrick Drob, J Michael Picone, David E Siskind, M Jones Jr, MG Mlynczak, PF Bernath, X Chu, E Doornbos, Bernd Funke, et al. NRLMSIS 2.0: A whole-atmosphere empirical model of temperature and neutral species densities. *Earth and Space Science*, 8(3):e2020EA001321, 2021.

[117] Piotr Kalaczynski. The Measurement and Modelling of Cosmic Ray Muons at KM3NeT Detectors. *National Centre for Nuclear Research*, PhD thesis, 2023.

[118] Carl De Boor and Carl De Boor. *A practical guide to splines*, volume 27. springer-verlag New York, 1978.

[119] Thomas K Gaisser, Todor Stanev, and Serap Tilav. Cosmic ray energy spectrum from measurements of air showers. *Frontiers of Physics*, 8:748–758, 2013.

[120] Thomas K Gaisser. Spectrum of cosmic-ray nucleons, kaon production, and the atmospheric muon charge ratio. *Astroparticle Physics*, 35(12):801–806, 2012.

[121] O Adriani, GC Barbarino, GA Bazilevskaya, R Bellotti, M Boezio, EA Bogomolov, M Bongi, V Bonvicini, S Borisov, S Bottai, et al. Time dependence of the proton flux measured by PAMELA during the 2006 july–2009 december solar minimum. *The Astrophysical Journal*, 765(2):91, 2013.

[122] P Montini and SM Mari. The bending of the proton plus helium flux in primary cosmic rays measured by the ARGO-YBJ experiment in the energy range from 20 TeV to 5 PeV. *arXiv preprint arXiv:1608.01389*, 2016.

[123] VV Prosin, SF Berezhnev, NM Budnev, A Chiavassa, OA Chvalaev, OA Gress, AN Dyachok, SN Epimakhov, NI Karpov, NN Kalmykov, et al. Tunka-133: Results of 3 year operation. *Nuclear Instruments and Methods in Physics Research Section A: Accelerators, Spectrometers, Detectors and Associated Equipment*, 756:94–101, 2014.

[124] EE Korosteleva, VV Prosin, LA Kuzmichev, and G Navarra. Measurement of cosmic ray primary energy with the atmospheric cherenkov light technique in extensive air showers. *Nuclear Physics B-Proceedings Supplements*, 165:74–80, 2007.

[125] Charles Jui. Summary of results from the telescope array experiment. In *The 34th International Cosmic Ray Conference*, volume 236, page 035. SISSA Medialab, 2016.

[126] Sebastiano Aiello, Arnauld Albert, S Alves Garre, Zineb Aly, Fabrizio Ameli, Michel Andre, Giorgos Androulakis, Marco Anghinolfi, Mancia Anguita, Gisela Anton, et al. gSeaGen: the KM3NeT GENIE-based code for neutrino telescopes. *Computer Physics Communications*, 256:107477, 2020.

[127] J-H Koehne, Katharina Frantzen, Martin Schmitz, Tomasz Fuchs, Wolfgang Rhode, Dmitry Chirkin, and J Becker Tjus. PROPOSAL: A tool for propagation of charged leptons. *Computer Physics Communications*, 184(9):2070–2090, 2013.

[128] Costas Andreopoulos, A Bell, D Bhattacharya, F Cavanna, J Dobson, S Dytman, H Gallagher, P Guzowski, R Hatcher, P Kehayias, et al. The GENIE neutrino monte carlo generator. *Nuclear Instruments and Methods in Physics Research Section A: Accelerators, Spectrometers, Detectors and Associated Equipment*, 614(1):87–104, 2010.

[129] Stanislav R Kelner, Rostislav Pavlovich Kokoulin, and Anatoly Afanasievich Petrukhin. About cross section for high-energy muon bremsstrahlung. Technical report, 1995.

[130] A.A. Petrukhin R.P. Kokoulin. Proceedings of 12th international conference on cosmic rays. 1971.

[131] Halina Abramowicz and Aharon Levy. The ALLM parameterization of $\sigma_{tot}(\gamma^* p)$. *arXiv preprint hep-ph/9712415*, 1997.

[132] Lev Davidovich Landau and II Pomeranchuk. The limits of applicability of the theory of bremsstrahlung by electrons and of the creation of pairs at large energies. In *Dokl. Akad. Nauk SSSR*, volume 92, page 535, 1953.

[133] SI Klimushin, EV Bugaev, and Igor A Sokalski. Precise parametrizations of muon energy losses in water. *arXiv preprint hep-ph/0106010*, 2001.

[134] Donald E Groom, Nikolai V Mokhov, and Sergei I Striganov. Muon stopping power and range tables 10 MeV–100 TeV. *Atomic Data and Nuclear Data Tables*, 78(2):183–356, 2001.

[135] Rudolph M Sternheimer. The density effect for the ionization loss in various materials. *Physical Review*, 88(4):851, 1952.

[136] Hans Bethe and Walter Heitler. On the stopping of fast particles and on the creation of positive electrons. *Proceedings of the Royal Society of London. Series A, Containing Papers of a Mathematical and Physical Character*, 146(856):83–112, 1934.

[137] A. A. Petrukhin and V. V. Shestakov. The influence of the nuclear and atomic form factors on the muon bremsstrahlung cross section. *Canadian Journal of Physics*, 46(10):S377–S380, 1968.

[138] Spencer Klein. Suppression of bremsstrahlung and pair production due to environmental factors. *Reviews of Modern Physics*, 71(5):1501, 1999.

[139] Arkady B Migdal. Bremsstrahlung and pair production in condensed media at high energies. *Physical Review*, 103(6):1811, 1956.

[140] Paolo Lipari and Todor Stanev. Propagation of multi-TeV muons. *Phys. Rev. D*, 44:3543–3554, Dec 1991.

[141] Atsushi Okada. On the atmospheric muon energy spectrum in the deep ocean and its parameterization. *Astroparticle Physics*, 2(4):393–400, 1994.

[142] Jürguen Brunner. The refraction index at ANTARES site. *ANTARES internal note*, 2000.

[143] Stefania Sparnocchia, Gian Pietro Gasparini, Katrin Schroeder, and Mireno Borghini. Oceanographic conditions in the NEMO region during the KM3NeT project (april 2006–may 2009). *Nuclear Instruments and Methods in Physics Research Section A: Accelerators, Spectrometers, Detectors and Associated Equipment*, 626:S87–S90, 2011.

[144] Silvia Adrián-Martínez, Imen Al Samarai, A Albert, M André, M Anghinolfi, G Anton, S Anvar, M Ardid, AC Assis Jesus, T Astraatmadja, et al. Measurement of the group velocity of light in sea water at the ANTARES site. *Astroparticle Physics*, 35(9):552–557, 2012.

[145] John Price Riley and Roy Chester. *Chemical oceanography*. Elsevier, 2016.

[146] Sea Agostinelli, John Allison, K al Amako, John Apostolakis, H Araujo, Pedro Arce, Makoto Asai, D Axen, Swagato Banerjee, GJNI Barrand, et al. GEANT4—a simulation toolkit. *Nuclear instruments and methods in physics research section A: Accelerators, Spectrometers, Detectors and Associated Equipment*, 506(3):250–303, 2003.

[147] Maarten de Jong. Multi-dimensional interpolations in c++. *arXiv preprint arXiv:1907.02597*, 2019.

[148] Giorgio Riccobene, Antonio Capone, Sebastiano Aiello, M Ambriola, Fabrizio Ameli, I Amore, Marco Anghinolfi, A Anzalone, C Avanzini, G Barbarino, et al. Deep seawater inherent optical properties in the southern ionian sea. *Astroparticle Physics*, 27(1):1–9, 2007.

[149] G Riccobene. Overview over Mediterranean Optical Properties. In *VLVnT Workshop, NIKHEF Amsterdam*, 2003.

[150] Raymond C Smith and Karen S Baker. Optical properties of the clearest natural waters (200–800 nm). *Applied optics*, 20(2):177–184, 1981.

[151] Craig F Bohren and Donald R Huffman. *Absorption and scattering of light by small particles*. John Wiley & Sons, 2008.

[152] Curtis D Mobley. Light and water: radiative transfer in natural waters. *(No Title)*, 1994.

[153] Steven HD Haddock, Mark A Moline, and James F Case. Bioluminescence in the sea. *Annual review of marine science*, 2:443–493, 2010.

[154] Karel Melis, Aart Heijboer, and Maarten de Jong. KM3NeT/ARCA event reconstruction algorithms. In *Proceedings, 35th International Cosmic Ray Conference (ICRC2017)*, pages 76–78, 2017.

[155] The Jpp framework, https://sftp.km3net.de/documentation/jpp/v17.3.2/.

[156] Michael James David Powell. Restart procedures for the conjugate gradient method. *Mathematical programming*, 12:241–254, 1977.

[157] Samuel S Wilks. The large-sample distribution of the likelihood ratio for testing composite hypotheses. *The annals of mathematical statistics*, 9(1):60–62, 1938.

[158] MG Aartsen, M Ackermann, J Adams, JA Aguilar, M Ahlers, M Ahrens, C Alispach, K Andeen, T Anderson, I Ansseau, et al. Time-integrated neutrino source searches with 10 years of IceCube data. *Physical review letters*, 124(5):051103, 2020.

[159] Thijs van Eeden, Jordan Seneca, and Aart Heijboer. High-energy reconstruction for single and double cascades using the KM3NeT detector. *arXiv preprint arXiv:2205.02641*, 2022.

[160] B Caiffi, A Garcia Soto, A Heijboer, V Kulikovskiy, RS Muller, M Sanguineti, KM3NeT Collaboration, et al. Sensitivity estimates for diffuse, point-like, and extended neutrino sources with KM3NeT/ARCA. *Journal of Instrumentation*, 16(09):C09030, 2021.

[161] G Carminati, M Bazzotti, A Margiotta, and Maurizio Spurio. Atmospheric MUons from PArametric formulas: a fast GEnerator for neutrino telescopes (MUPAGE). *Computer Physics Communications*, 179(12):915–923, 2008.

[162] C Forti, H Bilokon, B d'Ettorre Piazzoli, TK Gaisser, L Satta, and Todor Stanev. Simulation of atmospheric cascades and deep-underground muons. *Physical Review D*, 42(11):3668, 1990.

[163] Serge Belongie et al. Rodrigues' rotation formula. *From MathWorld–A Wolfram Web Resource, created by Eric W. Weisstein. http://mathworld. wolfram. com/RodriguesRotationFormula. html*, 1999.

[164] M Schmelling, NO Hashim, C Grupen, S Luitz, F Maciuc, A Mailov, A-S Müller, H-G Sander, S Schmeling, R Tcaciuc, et al. Spectrum and charge ratio of vertical cosmic ray muons up to momenta of 2.5 tev/c. *Astroparticle Physics*, 49:1–5, 2013.

[165] Pablo Achard, O Adriani, M Aguilar-Benitez, M Van Den Akker, J Alcaraz, G Alemanni, J Allaby, A Aloisio, MG Alviggi, H Anderhub, et al. Measurement of the atmospheric muon spectrum from 20 to 3000 gev. *Physics Letters B*, 598(1-2):15–32, 2004.

[166] Thomas Hebbeker and Charles Timmermans. A compilation of high energy atmospheric muon data at sea level. *Astroparticle Physics*, 18(1):107–127, 2002.

[167] SR Baber, WF Nash, and BC Rastin. The momentum spectrum of muons at sea-level in the range 3–1000 gev/c. *Nuclear Physics B*, 4(6):539–548, 1968.

[168] BC Rastin. An accurate measurement of the sea-level muon spectrum within the range 4 to 3000 gev/c. *Journal of Physics G: Nuclear Physics*, 10(11):1609, 1984.

[169] PJ Hayman and AW Wolfendale. The momentum spectrum of cosmic ray muons near sea level in the momentum range 5-1000 gev/c. *Proceedings of the Physical Society*, 80(3):710, 1962.

[170] BC Nandi and MS Sinha. The charge ratio of muons at sea level in the range 5–600 GeV/c. *Nuclear Physics B*, 40:289–297, 1972.

[171] B Adeva, M Aguilar-Benitez, H Akbari, J Alcaraz, A Aloisio, J Alvarez-Taviel, G Alverson, MG Alviggi, H Anderhub, AL Anderson, et al. The construction of the L3 experiment. *Nuclear Instruments and Methods in Physics Research Section A: Accelerators, Spectrometers, Detectors and Associated Equipment*, 289(1-2):35–102, 1990.

[172] Edgar V Bugaev, A Misaki, Vadim A Naumov, TS Sinegovskaya, SI Sinegovsky, and N Takahashi. Atmospheric muon flux at sea level, underground, and underwater. *Physical Review D*, 58(5):054001, 1998.

[173] N Lesparre, D Gibert, J Marteau, Y Déclais, D Carbone, and Emmanuelle Galichet. Geophysical muon imaging: feasibility and limits. *Geophysical Journal International*, 183(3):1348–1361, 2010.

[174] Stefano Cecchini and Maurizio Spurio. Atmospheric muons: experimental aspects. *Geoscientific Instrumentation, Methods and Data Systems*, 1(2):185–196, 2012.

[175] Anatoli Fedynitch, William Woodley, and M-C Piro. On the accuracy of underground muon intensity calculations. *The Astrophysical Journal*, 928(1):27, 2022.

[176] Sadakazu Haino, T Sanuki, K Abe, K Anraku, Y Asaoka, H Fuke, M Imori, A Itasaki, T Maeno, Y Makida, et al. Measurements of primary and atmospheric cosmic-ray spectra with the bess-tev spectrometer. *Physics Letters B*, 594(1-2):35–46, 2004.

[177] Anatoli Fedynitch and Matthias Huber. Hadronic uncertainties of inclusive atmospheric lepton fluxes from fixed-target experiments. 2021.

[178] VI Zatsepin and Natalia V Sokolskaya. Three component model of cosmic ray spectra from 10 gev to 100 pev. *Astronomy & Astrophysics*, 458(1):1–5, 2006.

[179] Felix Riehn, Hans P Dembinski, Ralph Engel, Anatoli Fedynitch, Thomas K Gaisser, and Todor Stanev. The hadronic interaction model SIBYLL 2.3 c and feynman scaling. *arXiv preprint arXiv:1709.07227*, 2017.

[180] Alexander Aab, Pedro Abreu, Marco Aglietta, Justin M Albury, Ingomar Allekotte, Alejandro Almela, Jaime Alvarez-Muñiz, R Alves Batista, Gioacchino Alex Anastasi, Luis Anchordoqui, et al. Measurement of the fluctuations in the number of muons in extensive air showers with the Pierre Auger Observatory. *Physical review letters*, 126(15):152002, 2021.

[181] Lorenzo Cazon, Ruben Conceição, and Felix Riehn. Probing the energy spectrum of hadrons in proton air interactions at ultrahigh energies through the fluctuations of the muon content of extensive air showers. *Physics Letters B*, 784:68–76, 2018.